UNIVERSITY OF CALIFORNIA

Santa Barbara

1.55 µm InGaAs THz Synchronized Photoconductive Switch Array

A Dissertation submitted in partial satisfaction of the

requirements for the degree Doctor of Philosophy

in Electrical and Computer Engineering

by

Kimani K. Williams

Committee in charge:

Professor Daniel Blumenthal, Chair

Professor Arthur C. Gossard

Professor Mark Sherwin

Professor David Auston

June 2012

ProQuest LLC.
789 East Eisenhower Parkway
P.O. Box 1346
Ann Arbor, MI 48106 - 1346

The dissertation of Kimani K. Williams is approved.

_____

Arthur C. Gossard

_____

Mark Sherwin

_____

David Auston

_____

Daniel Blumenthal, Committee Chair

April 2012

1.55 µm InGaAs THz Synchronized

Photoconductive Switch Array

by

Kimani K. Williams

ACKNOWLEDGEMENTS

I would first like to thank Dr. Elliot R. Brown for getting me interested in the field of THz, as well as device fabrication. There's nothing more gratifying than taking an idea to the cleanroom: then converting this idea into fabricated devices, then testing it in the lab, and from the lab to the realization of success. Dr. Elliot R. Brown was instrumental in teaching me the tools to navigate all the stages of my research. Dr. Rahul Singh, Dr. Zachary Taylor, Dr. Weidong Zhang, and Dr. Adam Young also contributed significantly to this process, and for that I am truly grateful.

Colossal thanks to the members of my committee: Dr. Daniel Blumenthal, Dr. Arthur Gossard, Dr. Mark Sherwin and Dr. David Auston. The completion of this Ph.D. would not have been possible without the vast knowledge and insight that my committee has bestowed upon me. Special thanks to Dr. Arthur Gossard for his unwavering support and guidance when things seemed daunting.

I would like to thank NSF MRSEC for providing the opportunity for me to take on my project via the IRG4 program. One of the advantages of this program is that I got to collaborate with members of other fields and disciplines, including the University of California, Santa Barbara

Materials Department. Thanks to the UCSB Materials Department for making strides in the growth of semiconductors. More specifically, thanks to Dr. Hong Lu and Dr. Jeramy Zimmerman for providing materials essential to the success of my project. Special thanks to Dr. Sascha Preu for the wealth of knowledge he imparted to me, and his tireless efforts in assisting me in this project.

Thanks to the UCSB nanofabrication / cleanroom team for showing me the ins and outs of functioning in the cleanroom, and to Andy Weinberg in the machine shop for intricately and meticulously making my designs. It would be remiss of me not to acknowledge my group members who all played critical roles in the completion of my research: Wenzao Li, Mingzhi Lu, Jon Suen, Peter Krogen, Demis John, Geza Kurczveil, John Garcia, Renan Moreira and Kim Nguyen. Thank you all.

Lastly, I want to thank my family and loved ones for all the support and unconditional love they have shown me. No matter the circumstances, they were my rock. They never waned. I am truly blessed. Thank you.

VITA OF KIMANI K. WILLIAMS
April 2012

EDUCATION

May 2002	Bachelor of Arts Degree, Macalester College (Magna Cum Laude)
April 2012	Ph.D., Electrical Engineering University of California, Santa Barbara

PROFESSIONAL EMPLOYMENT

2006 – 2012	Graduate Research Assistant, University of California, Santa Barbara
2005 – 2006	Teaching Assistant, University of California, Santa Barbara

PUBLICATIONS AND CONFERENCE PROCEEDINGS

[1] "Towards a 1550 nm InGaAs Photoconductive Switch," Kimani K. Williams, Z.D. Taylor, J.Y. Suen, Hong Lu, R.S. Singh, A.C. Gossard, and E.R. Brown, Optics Letters, Vol. 34, No. 20, 2009.

[2] "High-Spectral-Resolution THz Reflective Imaging Based on a Tandem-Bandpass Filter", K. K. Williams and E. R. Brown, 2009 Nanoelectronic Devices for Defense and Security Conference, 29 Sept. 2009.

[3] "A conformal ultrasound transducer array featuring microfabricated polyimide joints," D. B. Bennett, M. O. Culjat, B. P. Cox, A. E. Dann, K. K. Williams, Hua Lee, E. R. Brown, W. S. Grundfest, and R. S. Singh, Proc. SPIE 7295, 72951W (2009).

[4] "Electrical Transport in an Insulating Semimetal-Semiconductor Nanocomposite," E.R. Brown,. W-D. Zhang, K. Williams, H. Lu, and A.C. Gossard, IEEE Trans. Nanotechology, Vol. 8, Issue 3, pp. 402-407 May 2009.

[5] "Simulation, fabrication, and characterization of a novel flexible, conformable ultrasound transducer array," R.S. Singh, M.O. Culjat, S.P. Vampola, K. Williams, W.S. Grundfest, H. Lee, and E.R. Brown, Proc.

2007 IEEE Ultrasonics Symposium, New York, NY, pp. 28-31 October 2007.

AWARDS

Best Student Presentation in Sensor and System Applications – Nanoelectronic Devices for Defense and Security Conference, September 2009.

ABSTRACT

1.55 μm InGaAs THz Synchronized

Photoconductive Switch Array

by

Kimani K. Williams

Metal-particle-in-semiconductor nanocomposites are of continuing interest in materials science to produce electronic, photonic, and thermoelectric devices, as well as chemical and biological nanosensors. These materials have successfully been employed for THz photoconductive devices operating at 800 nm. To date, producing devices operating at the desirable pump wavelength of 1.55 μm at which both mode-locked and single-frequency lasers needed for THz generation are readily available, remains challenging. Excessive dark current and prohibitively low breakdown voltage have been the primary impediments. Recent research has shown that ErAs:$In_{0.53}Ga_{0.47}As$ designed for subpicosecond photoconductivity exhibits an exponential increase in resistivity when cooled to temperatures below 250 K. This increased

resistivity gives promise to producing THz sources since higher bias voltages can be used, thus increasing the optical to THz conversion efficiency.

One of the major limitations of THz photoconductive sources is that it is challenging to harness sizeable power. Typical power levels generated by THz sources at 1.55 μm are generally in the low microwatts region. This dissertation demonstrates a 1.55 μm THz synchronized linear array that maximizes power and has attained an impressive maximum peak power of 123 μW. In addition, THz beam steering at 1.55 μm by phase control in the time domain is a young field. Beam steering is demonstrated with this phased array up to 14.6^0 using optical delay line units. The possibility of beam steering will prove beneficial in various applications, particularly in standoff imaging.

Table of Contents

LIST OF FIGURES

1. Terahertz Introduction

The electromagnetic spectrum is a range of all possible frequencies of electromagnetic radiation. Terahertz (THz) radiation is generally considered the region of the spectrum that can be found between the high frequency edge of the microwave band (100×10^9 Hz or 0.1 THz) and the long wavelength edge of the far-infrared light (10×10^{12} Hz or 10 THz). This corresponds with a range of wavelengths from 0.03 mm to 3 mm. Before the 1990's, THz radiation was both hard to detect and produce. Detectors did not have the required sensitivity and generally required cryogenic temperatures for operation. THz sources were bulky and cumbersome, and therefore not ideal for portable and compact applications. However, in recent decades, there have been steady improvements in both generating and detecting broadband THz pulses. In particular, the improvements in solid-state semiconductor technology have led to more compact and portable THz sources. This complemented with the fact that a lot of common materials are transparent, and also many chemical materials have distinct absorption signatures in this region of the spectrum, makes THz radiation a promising field to explore. The development of both detectors and sources has resulted in the evolution of various applications including THz spectroscopy for sensing

and imaging. In order to take full advantage of THz region of the spectrum, there has been ongoing research to improve both THz detectors and sources.

The current telecommunications platform commonly uses systems operating at a wavelength of 1.55 μm. Therefore, operating at this wavelength is very appealing for THz devices, and will also reduce cost. One of the major limitations of THz photoconductive sources is that it is challenging to harness sizeable power. Typical power levels generated by THz sources at 1.55 μm are generally in the low microwatts region. However, this power level is enough to perform THz time domain spectroscopy (TDS) [1]. Therefore, constructing a synchronized linear array to maximize power would provide substantially more power, which would increase the signal to noise ratio and the dynamic range of the source. This dissertation discusses the performance of a 1.55 μm synchronized linear array of photoconductive switches. In addition, THz beam steering at 1.55 μm is demonstrated y phase control of the individual elements in the time domain utilizing fiber delay stages. Such a phased array will prove beneficial in applications of spectroscopy and security imaging since it allows scanning for a narrow THz spot in a target plane.

Metal-particle-in-semiconductor nanocomposites are of continuing interest in materials science to produce electronic, photonic, and thermoelectric devices, as well as chemical and biological nanosensors. Progress has been made in using these materials to develop high-repetition-rate picoseconds sources of THz radiation using GaAs as the host material [2], which has to be optically excited by a pump wavelength of 800 nm. However, using these materials for such THz photoconductive devices optically excited by 1.55 μm has been investigated, but to date has not produced a suitable device operating at this desirable pump wavelength, where both mode-locked and single-frequency lasers needed for THz generation are readily available. Excessive dark current and prohibitively low breakdown voltage have been the primary impediments. Recent research has shown that ErAs:$In_{0.53}Ga_{0.47}As$ designed for subpicosecond photoconductors exhibits an exponential increase in resistivity when cooled to temperatures below 250 K [3]. This increased resistivity gives promise to producing THz sources for operation at 1.55 μm because of the higher bias voltage and efficiency now possible.

1.1. Terahertz Detectors

Thermal detectors are accurate for detecting THz radiation. A common thermal detector used to detect THz radiation is the bolometer. The bolometer measures the power of incident radiation using an absorptive material with a temperature dependent electrical resistance. This material may be a superconductor operated close to the transition edge to normal conduction, resulting in huge responsivities. Typically, bolometers are operated at cryogenic levels at 4.2 K, which is the temperature of liquid helium. For superconducting bolometers, the cryogenic operation is a prerequisite to reach the superconducting state. For other bolometer types, like the high temperature electron bolometer, the low temperatures strongly increase sensitivity and minimize thermal noise, which scales with the square root of temperature. At 1 THz, the 4.2 K bolometer can provide an optical noise equivalent power (NEP) of approximately $1x10^{-12}$ W-Hz $^{-1/2}$. This translates to a minimum detectable power of approximately 10 pW for a bandwidth of 10 Hz [4]. For operation at room temperature, a Golay cell can be used. It is an opto-acoustic detector. It consists of a gas filled chamber also containing an absorptive element that is connected to a flexible membrane. The absorption of THz radiation expands the gas and causes a deformation of the membrane, which is detected with a photodiode. The Golay cell has a

nominal optical responsivity of 10 mV/μW and a NEP of approximately $2x10^{-10}$ W-Hz $^{-1/2}$ [5]. Its responsivity is very uniform over a broad range of frequency, spanning the whole THz region. Another option for a room temperature detector is the pyroelectric detector. The pyroelectric detector converts THz radiation to electrical signals by spontaneous electric polarization of a pyroelectric material: incident THz radiation generates heat which alters the polarization of the pyroelectric material. This change is read out capacitively, resulting in an electrical signal. It typically has a NEP of $2x10^{-8}$ W-Hz $^{-1/2}$ [4]

1.2. Terahertz Applications

Important features of THz radiation are that it is non-ionizing and has the capacity to penetrate through a variety of materials: clothing, luggage, plastic, cardboard, etc. [6]. There are also many biological signatures that are in the THz band [7]. This lends itself to a variety of useful applications. This includes molecular spectroscopy [8], chemical sensing [9], detection of dangerous materials, including drugs and explosives [6], and characterization of biological materials [10]. In many cases, a THz time domain setup is used. A THz-TDS is generally based on photoconductive antennas for detection and generation of far-infrared

light. The photoconductive antenna under bias is excited by a mode-locked laser, which leads to excitation of carriers. An applied bias separates electrons from holes, generating a current transient, which is fed into an antenna, emitting a THz pulse. Free space optics are then used to focus the THz radiation on the target material under test (DUT). The transmitted THz light focused onto a coherent photomixer detector that is driven with the same laser as used for THz generation. By using a variable delay line, the detection laser pulse can be continuously delayed compared to that of the incident THz pulse, which results in sampling of the profile of the electric field of each pulse. The pulses are measured with and without the target material. The two pulses are then Fourier-transformed to the frequency domain to determine their spectra. The comparison reveals the absorption spectrum of the DUT. Chemical materials have distinctive spectra and therefore can be identified in analyzing their spectra. For example, Figure 1.1, sucrose exhibits specific absorption bands at specific frequencies and therefore allows the capability to distinguish it from other sugars.

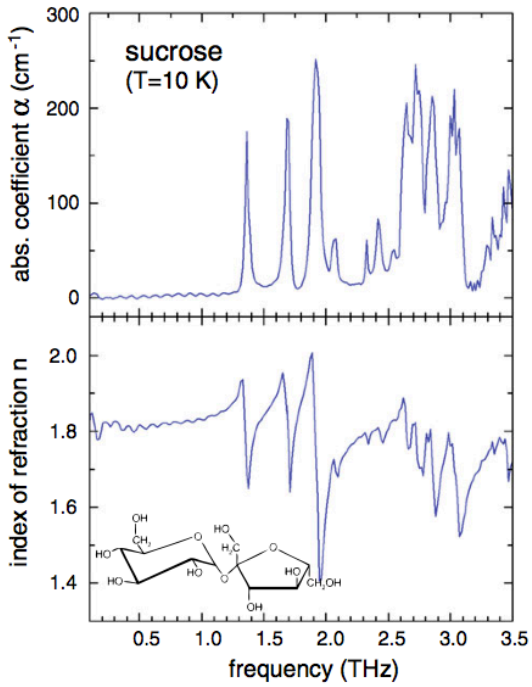

Figure 1.1: Spectrum of polycrystalline sucrose [11]

In the case of molecular spectroscopy, THz-TDS has been used to not only differentiate between glucose and fructose but also determine their molecular structure. Both have the same molecular formula but different molecular structures. Vibrational modes in the THz region result from interactions between chemical bonds and dispersive forces. Given that the two have different molecular structures, they will have two distinct spectra. The spectra of glucose and fructose were measured and studied in the frequency region of 0.5 to 4 THz using THz-TDS at room

temperature. The data was also used to determine the molecular arrangement of each compound.

In the case of detection of dangerous materials, it is either the transmitted or reflected THz pulses that are detected. If the target is transparent to THz radiation (plastic, clothing, many liquids, etc.), typically the transmitted THz pulses are detected. If the material strongly absorbs the THz radiation, then the reflected THz pulses are used to determine its dielectric properties [10]. At 94 GHz, many dielectric materials (clothing and paper) are transparent. Figure 1.2 shows an individual holding a knife concealed in a newspaper. The newspaper is transparent but the knife is reflective at 94 GHz. Therefore, harmful substances concealed by clothing, luggage, envelopes, etc. can be detected.

Figure 1.2: An individual holding a concealed weapon in a newspaper obtained at 94 GHz [6].

1.3. Thesis Overview

This thesis explores a special form of metal nanoparticle made from binary compound semimetals embedded in a semiconductor matrix: ErAs nanoparticles embedded in $In_{0.53}Ga_{0.47}As$. An array of photoconductive antennas is developed for operation at 1.55 μm. This was achieved by material engineering to produce a material that has subpicosecond lifetime that can sustain high bias voltage, and has low dark current (high resistivity). This material displayed all the criteria needed to develop a 1.55 μm array of photoconductive antennas when the temperature was lowered below 250 K. However, experiments were done at 77 K, since the resistivity and breakdown voltage was higher at this temperature and the temperature of 77 K is easy to maintain in a liquid nitrogen cryostat. The photoconductive switch was comprised of a self-complementary square spiral antenna fabricated on the InGaAs material on a InP substrate. When the semiconductor material is optically pumped by a 1.55 μm mode-locked laser, electron-hole pairs in the material are excited by the laser's ultra fast pulse, 80 fs. These carriers are separated by an applied electric field, which results in the generation of photocurrent. The photocurrent is then coupled by the square spiral antenna and generates THz power. The THz emission can be increased by increasing the electric field in the semiconductor, which can be done

by either increasing the applied bias voltage or by decreasing the gap distance between electrodes of the antenna at a constant applied bias voltage. The designed square spiral antenna was broadband. It produced THz power at frequencies from 13 GHz to 1.35 THz.

The fabrication of the array of photoconductive antennas is discussed in detail and its DC characteristics studied extensively. The lifetime of the material was also measured using the pump-probe technique. The array of photoconductive antennas had to be mounted in a 77 K cryostat, which required packaging the material. The methods of packaging the array and the experimental design are also discussed in detail. Measurements of THz power were taken for a single source, 2-source and 4 source linear arrays of photoconductive switches with and without a 600 GHz commercial filter. Experiments were done to test the dependency of THz power on the applied bias voltage and the dependency of number of sources. The ultimate goal was to achieve beam steering in the time domain at a wavelength of 1.55 μm. This was accomplished by the use of optical delay lines varying the arrival of laser pulses at the individual photoconductive antennas. A relationship between the phase of the THz pulses and the optical time delay was established in order to manipulate the phases of the THz radiation. In so doing, constructive and destructive interferences were controlled to get the beam steered in a

desired direction. Maximum peak power levels of10.38 µW, 38.12 µW, and 123.4 µW were obtained for a single source, 2-source and 4-source photoconductive linear arrays respectively at 77 K with no frequency filter present. However, the array of photoconductive antennas had reduced efficiency at higher frequencies and also THz signal was filtered using a frequency selective surface. This resulted in a reduction of THz power at higher frequencies. The maximum peak power levels of 4.75 µW, 16.15 µW, and 40.45 µW were obtained for a single source, 2-source and 4-source photoconductive linear arrays respectively at 77 K with frequency selective filter of 600 GHz. These power levels can successfully be used for the aforementioned applications. In addition, the array of photoconductive antennas had a beam steering capability of 12.77^0 and 14.6^0 for 2 and 4-source linear array respectively.

1.4. References

1. E. R. Mueller, "Terahertz Radiation: Applications and Sources," American Institute of Physics, p. 27-29 (2003).

2. E.R. Brown, "A photoconductive model for superior GaAs THz photomixers," Appl. Phys. Lett., Vol. 75, p. 769 - 771 (1999).

3. E.R. Brown, K. K. Williams, W-D. Zhang, J. Suen, Hong Lu, J. Zide, and A.C. Gossard "Electrical Transport in an Insulating Semimetal-Semiconductor Nanocomposite," IEEE Nanotechnology, Vol. 8, p. 402–407 (2009).

4. E. R. Brown, "THz Generation by Photomixing in Ultrafast Photoconductors," International Journal of High Speed Electronics and Systems, Vol. 13, p. 147-195 (2003).

5. K. K. Williams, Z. D. Taylor, J. Y. Suen, Hong Lu, R. S. Singh, A. C. Gossard, and E. R. Brown "Toward a 1550 nm InGaAs Photoconductive Switch for Terahertz Generation,", Optics Letters, Vol. 34, p. 3068 – 3070 (2009).

6. A. G. Davies, A. D. Burnett, W. Fan, E. H. Linfield, and J. E. Cunningham, "Terahertz spectroscopy of explosive and drugs," Materials Today, Vol. 11, p. 18-26 (2008).

7. B. Fischer, M. Hoffman, H. Helm, G. Modjesch, and P. U. Jepsen, "Chemical recognition in terahertz time-domain spectroscopy and imaging," Semicond Sci Technol, Vol. 20, p. S246 – S253 (2005).

8. Zhuan-Ping Zheng, Wen Hui Fan, Yu-Qing Liang, and Hui Yan, "Application of terahertz spectroscopy and molecular modeling in isomers investigation: Glucose and fructose," Optics Communications, Vol. 285, p. 1868-1871 (2012).

9. M. Walther, B. M. Fischer, A. Ortner, A. Bitzer, A. Thoman, and H. Helm, "Chemical sensing and imaging with pulsed terahertz radiation," Anal. Bioanal Chem, Vol. 397, p. 1009 - 1017 (2010).

10. B.L. Yu, Y. Yang, F. Zeng, X. Xin, and R.R. Alfano, "Terahertz absorption spectrum of D_2O vapor," Optics Comm, Vol. 258, p. 256-263 (2006).

11. M. Walther, B. M. Fischer, and P. U. Jepsen, "Non covalent intermolecular forces in poly-crystalline and amorphous saccharides in the far infrared," Chem. Phys. Vol. 288, p. 261 – 268 (2003).

2. Photoconductive THz Source

2.1. THz Sources

Viable sources of THz radiation for spectroscopic and imaging applications include oscillators [1], lasers [2] and solid-state devices [3]. The Backward Wave Oscillator (BWO) utilizes an electron gun to generate an electric beam through a vacuum tube that contains a slow wave structure. Oscillations are perpetuated through the tube and the generated power is coupled out near the electron gun. The BWO can generate THz average power on the order of Watts at low frequencies and beams of 190 mW at ~ 1 THz have been reported [4]. However, the BWO is a cumbersome system and is not suitable for portable operations. The Free Electron Laser (FEL) also suffers from practical limitations. It uses an electron beam as its lasing medium. The stream of electrons moves freely through a sequence varying magnetic fields, the undulator. It causes oscillations of the electrons, which then results in radiated THz power that is stored in a cavity. FELs can be tuned over a very broad band by varying the energy of the electron beam or the strength of the magnetic field. FEL's can produce free space output powers in excess of hundreds of Watts [2]. The FELs at University of California, Santa

Barbara can obtain average THz power of 15 kW with the tunable wavelength range from 2.5 mm to 63 μm (0.12 - 4.76 THz) [2].

The Quantum Cascade Lasers (QCL), emerged on the scene in the mid 1990s at the Bell Laboratories. At that time people were using semiconductor lasers that utilized the recombination of electrons and holes to emit radiation. However, the QCL used a single type carrier and the quantum confinement in heterostructures to create electronic transitions between conduction band states [5]. Since the wavelength is determined by the quantum confinement then the heterostructure can be designed to attain a specified submillimeter wavelength. A threshold power density of ≈ 1 kW/cm^2 at a continuous wave temperature of 25°C for a wavelength range of λ = 4.7 - 5.6 μm have been achieved using cascade lasers [6]. However, the most promising THz sources for a portable system are solid-state semiconductor devices.

2.2. GaAs vs InGaAs

Due to advancements in semiconductor technology, photoconductive sources have become promising sources of broadband THz radiation. Breakthroughs in this technology include the growth of semiconductor material having subpicosecond lifetime, improvements in fabrication techniques that allow sub-micron electrode features to be patterned on

the semiconductor surface, and the design of planar antennas that can efficiently couple the THz radiation to free space. The most successful THz photoconductive antenna has been achieved by exciting low temperature grown (LTG) GaAs with a wavelength of 800 nm. LTG GaAs is grown by molecular-beam epitaxy (MBE) at temperatures less than 200^0 C. Arsenic clusters are formed that act as recombination sites for electrons. LTG GaAs can be engineered to reach lifetime of 400 fs [7], a high electrical breakdown electric field in the range of 500 – 1000 KV/cm [8], and high resistvity, which are crucial for THz generation. One of the disadvantages of generating high power, short pulsed THz radiation at 800 nm is the requirement of high power pulsed laser systems. Typically, Ti: sapphire systems are used, making the experimental setup bulky, fragile, and increasing the cost.

Exciting a semiconductor material with 1.55 μm circumvents this problem by giving the capability of using fiber optics instead of the bulky free space optics. 1.55 μm is the wavelength of optical telecommunications, which means access to ready available optical fiber technology, measurement capabilities, and a significant cost reduction. Furthermore, solid-state and semiconductor lasers are available at this wavelength range that are capable of providing high levels of tunable laser power with subpicosecond pulses. For THz radiation to efficiently

couple to free space at a wavelength of 1.55 μm, a narrower bandgap than that of GaAs is required complemented with maintaining the subpicosecond lifetime and high resistivity. The photon energy of 1.55 μm light ($h\upsilon$ = 0.80 eV) is above the absorption threshold of $In_{0.53}Ga_{0.47}As$, that has a bandgap of 0.75 eV; therefore $In_{0.53}Ga_{0.47}As$ lattice matched with InP is a suitable choice of material. Furthermore, $In_{0.53}Ga_{0.47}As$ has a quantum efficiency that is almost twice as good as that of GaAs due to the smaller photon energy; 1.55 μm pulsed laser generates twice the photocurrent compared to that of 800 nm with the same optical power.

Growing $In_{0.53}Ga_{0.47}As$ at low temperatures does not produce the same quality material as does LTG GaAs; with the decrease of growth temperature, the carrier concentration in $In_{0.53}Ga_{0.47}As$ increases by orders of magnitude. This results in high dark conductivity, which is not suitable for efficient THz generation. Therefore, in order to make $In_{0.53}Ga_{0.47}As$ suitable for THz radiation, creative growth methods have been developed to combat these negative effects. One such method is iron (Fe) implantation. This has been used to improve the performance of $In_{0.53}Ga_{0.47}As$ photoconductive sources [9]. In this work, experiments were performed using $In_{0.53}Ga_{0.47}As$ optically excited at 1.56 μm. The Fe implant sites act as recombination sites for electron and holes, which

resulted in a lower lifetime of the material. The Fe implanted $In_{0.53}Ga_{0.47}As$ also had an increase in resistivity compared to that of $In_{0.53}Ga_{0.47}As$ with no Fe implant. However, the disordered state of Fe defects placed a limitation on the lifetime of the material. An alternative method used heavy ion, Br^+, irradiated $In_{0.53}Ga_{0.47}As$ for THz source at 1.55 μm. This created a more ordered state of trap sites, and therefore, more flexibility in controlling the lifetime [10]. High energy irradiated Br^+ ions of the order of magnitude 10^{11} cm^{-2} were implanted in the InP. This resulted in a lower lifetime (0.2 ps), lower electron mobility (490 cm^{-2} V s), and hence an increase in dark resistivity (3 Ω cm).

This thesis deals with a special form of metal nanoparticle made from binary compound semimetals embedded in a semiconductor matrix: ErAs nanoparticles embedded in $In_{0.53}Ga_{0.47}As$ [11]. This is a nanocomposite that has been utilized in recent years for a number of interesting device applications, including ultrafast photoconductors [12,13], THz photomixers [14], near-infrared plasmon resonators [15], and thermoelectric thin films [16]. The nanocomposite samples were grown by molecular beam epitaxy at a temperature of 490°C. The first epitaxial layer was a 0.1-micron-thick $In_{0.52}Al_{0.48}As$ buffer layer grown on a semi-insulating InP substrate. This layer was lattice-matched to $In_{0.53}Ga_{0.47}As$. Erbium and beryllium were co-deposited along with the In and Ga, the

erbium tended to coalesce into nanocrystallites, and the Be tended to incorporate as a hydrogenic acceptor. The Er-fraction and the Be concentration in the sample were estimated to be 0.3% by composition and $5x10^{18}$ cm^{-3} respectively. Hall measurements were made on the film at room temperature yielding n-type behavior with a resistivity of 13.1 Ω-cm, a free electron concentration of $1.2x10^{15}$ cm^{-3} and a mobility of 384 $cm^{-2}V$-s. The Be-compensation and co-deposition techniques have been successful in the past; the primary benefit being a compensation of the normally n-type ErAs and thus a large enhancement of the room-temperature resistivity of the composite material compared to that of the uncompensated material [17].

The present structure and all similar nanocomposites studied to date have been grown by molecular beam epitaxy at relatively low Er mass fraction (typically < 2%). This has the advantage over chemical deposition and self-assembly methods of being cleaner and less susceptible to contamination after growth. Specifically, under the right growth conditions, the ErAs nanoparticles embed as single crystals with little impact (chemical or elastic) on the surrounding single-crystal semiconductor. ErAs is a semi-metallic material, which acts as efficient nonradiative trapping centers similar to the As precipitates in LTG GaAs. Therefore, the growth of the material with ErAs nanoparticles can

be controlled to achieve subpicosecond lifetime and also results in higher resistivity needed for THz generation and propagation. Figure 2.1 shows the structure of the material that was used to fabricate a photoconductive source.

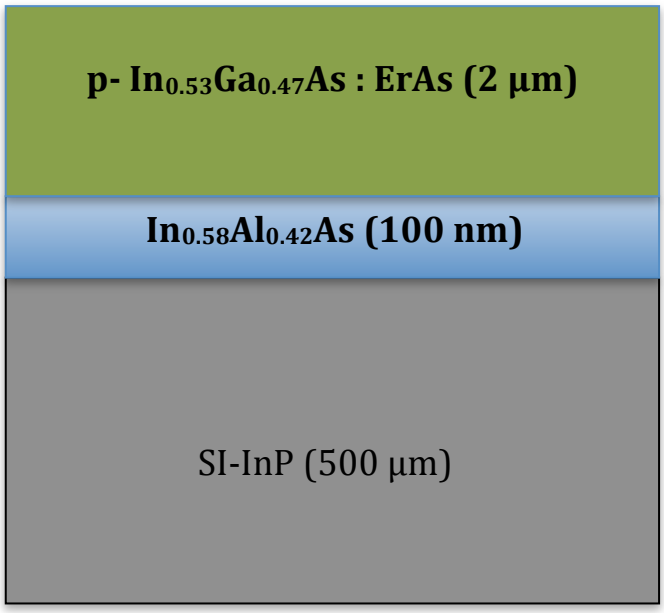

Figure 2.1: Structure of photoconductive material

2.3. Square Spiral Antenna

As previously discussed, this material is suitable for generating THz photons when excited by 1.55 µm mode-locked lasers. However, a square spiral antenna was used to couple out the THz radiation. The high dielectric constant, 13.94 [18], of InGaAs resulted in most of the THz radiation coupling into the substrate side of the spiral antenna instead of coupling into free space. Irrespective of antenna design, coupling the

generated THz power through the substrate side of the antenna and into free space poses a challenge. To overcome this obstacle, a hyperhemispherical lens made from a high refractive index, n, similar to that of the semiconductor and high resistivity material was placed on the backside of the photoconductive switch as shown in Figure 2.2. A silicon lens satisfied the aforementioned conditions and was used to couple the THz radiation to free space.

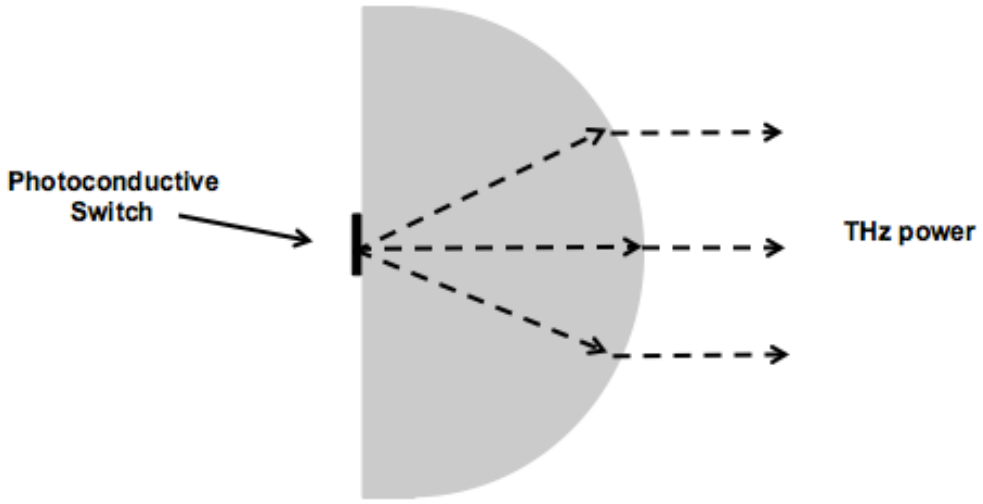

Figure 2.2: Cross sectional view of a hyperhemispherical silicon lens that was used to couple THz power from the backside of photoconductive switch into free space.

The substrate thickness was incorporated into the lens setback (0.76 mm), calculation and the antenna sits at the aplanatic point of the lens [8]. Thus most of the THz radiation from the antenna will pass into free space. Silicon dielectric constant (11.8) is closely matched to that of

InGaAs or GaAs, which results in effective transmission of the THz radiation into free space.

Ideally the antenna should be designed to radiate THz power over a wide range of frequencies. Antennas that were developed for THz power generation includes the tapered dipole [19], self-complementary log periodic [20] or log spiral designs [21]. However, a self-complementary square spiral antenna when designed properly will produce a frequency-independent beam pattern when coupled through a silicon hyperhemispherical lens. The symmetrical properties of the antenna results in the frequency independent radiation beam pattern, while the self-complementary design results in the antenna having high driving point impedance [22]. An image of the square spiral design is shown in Figure 2.3.

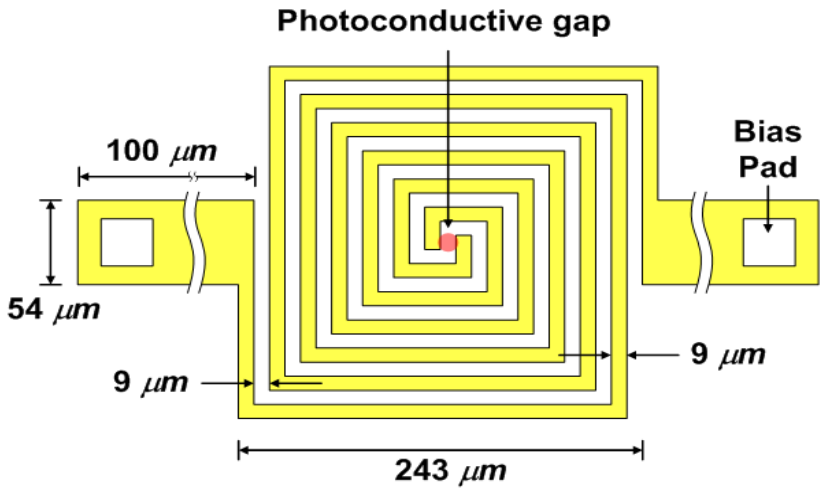

Figure 2.3: Self-complementary square spiral antenna with a photoconductive gap of 9 x 9 μm

The square spiral antenna is made up of 293 9 x 9 µm unit cells, in which each arm of the spiral is constituted of straight segments of an odd integer progression of 1, 3, 5….etc unit cells. The estimated frequency range can be determined by the following expression [21].

$$f_{\max,\min} = \frac{c}{L_{\min,\max}(\varepsilon_{eff})^{\frac{1}{2}}} \qquad 2.1$$

L_{min} and L_{max} are the minimum and maximum radiating perimeters of the square antenna spiral, and ε_{eff} is the effective dielectric constant for InGaAs. The effective dielectric constant on InGaAs-air interface is $\varepsilon_{eff} \approx (1 + \varepsilon_r)/2$, where ε_r is 13.94. L_{min} is the perimeter of the inner square, and L_{max} is the perimeter of the outer square shown in Figure 2.4. For this designed square spiral antenna, L_{min} and L_{max} were 81 µm (9 x (3 + 3 + 3 + 3)) and 8424 µm (9 x (243 +225 + 243 + 225)) respectively. This resulted in a f_{min} of 13 GHz and a f_{max} of 1.35 THz. The square spiral antenna will radiate at higher frequencies, but with reduced efficiency. Therefore, the broadband aspect of the antenna was dependent on the designed dimensions.

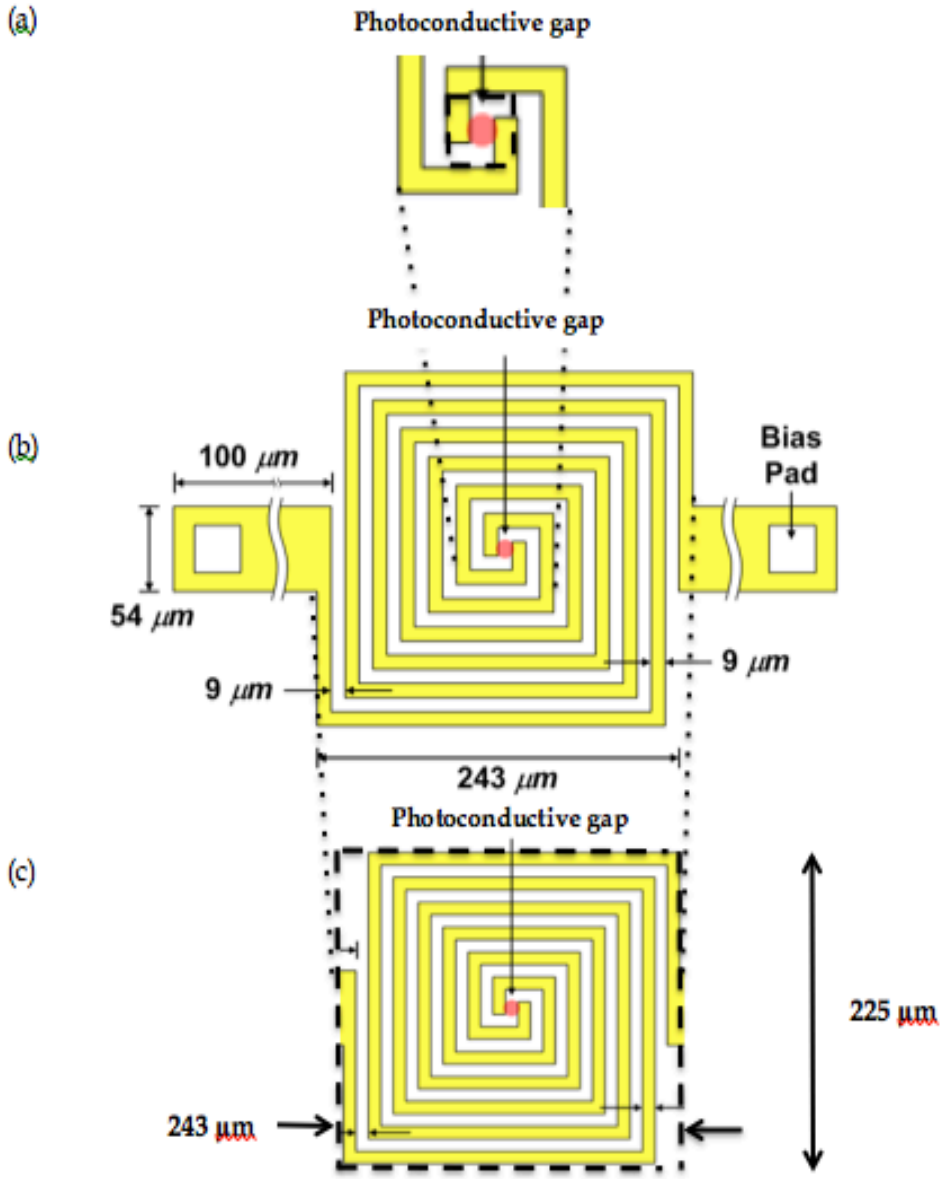

Figure 2.4: (a) Inner radiating perimeter that give rise to L_{min}. (b) Complete square spiral. (c) Outer radiating perimeter that give rise to L_{max}.

The performance of the square spiral antenna was simulated using the software High Frequency Structural Simulator (HFSS). HFSS was used to analyze the directivity of the antenna and the refractive effects of the silicon hyperhemispherical lens. The dimensions of the antenna were modeled as the same as the actual square spiral antenna. Same was also done for the thickness of titanium, platinum and gold (5000 Å) that were used for the metal deposition on the InGaAs material. The dielectric constant of the substrate was set the same as that of InGaAs, and no lumped components (such as capacitors) were used in the simulation. However, the actual size of the silicon lens (curvature of radius 5 mm) had to be reduced to one third of its size, to significantly decrease simulation time. This reduction in the size of the lens for simulation affected the directivity of the THz radiation. However, it gave insight to the behavior of the photoconductive switch. Since the actual lens is bigger than the simulated lens, better directivity was expected compared to that of the simulated directivity. Figure 2.5 shows the schematic of the simulation of the photoconductive switch in which the x and y axes are in the plane of the square spiral antenna, and the z-axis is in the direction of the emanating THz radiation.

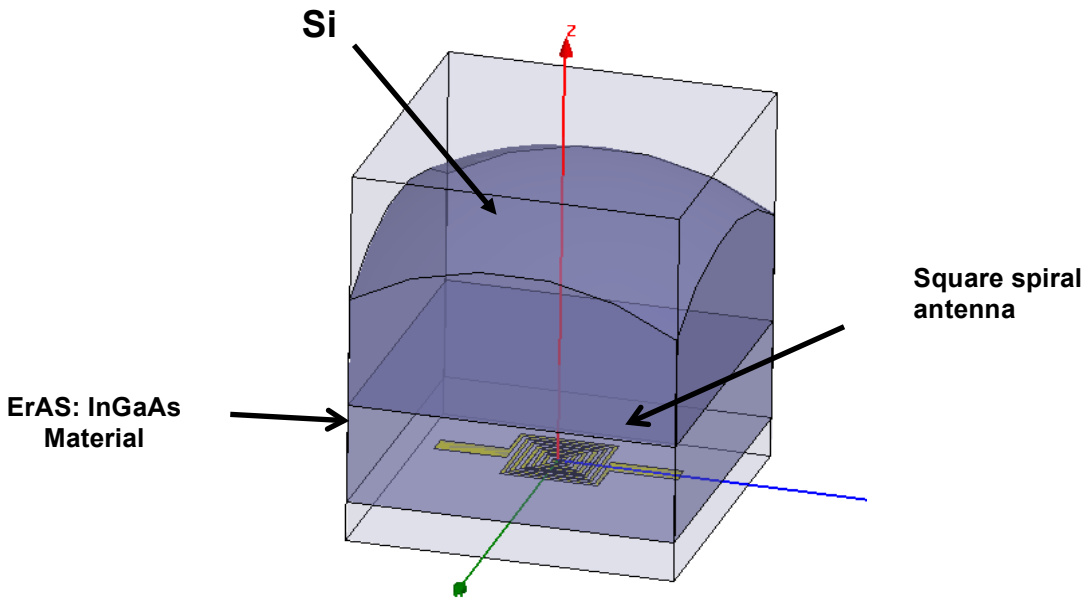

Figure 2.5: (a) Schematic for the simulated square spiral antenna.

Figure 2.6 shows the simulated directivity of the antenna, (a), and the angle dependency of the radiation pattern, (b), at 600 GHz. The beam pattern was aberrated because of the truncation of the simulated lens; however, a directivity of 12 dB was achieved with a full width half max (FWHM) of approximately 25 degrees. In addition, the directivity patterns at different □ angles were consistent, which showed that the antenna displayed isotropic behavior in □ directions at 600GHz.

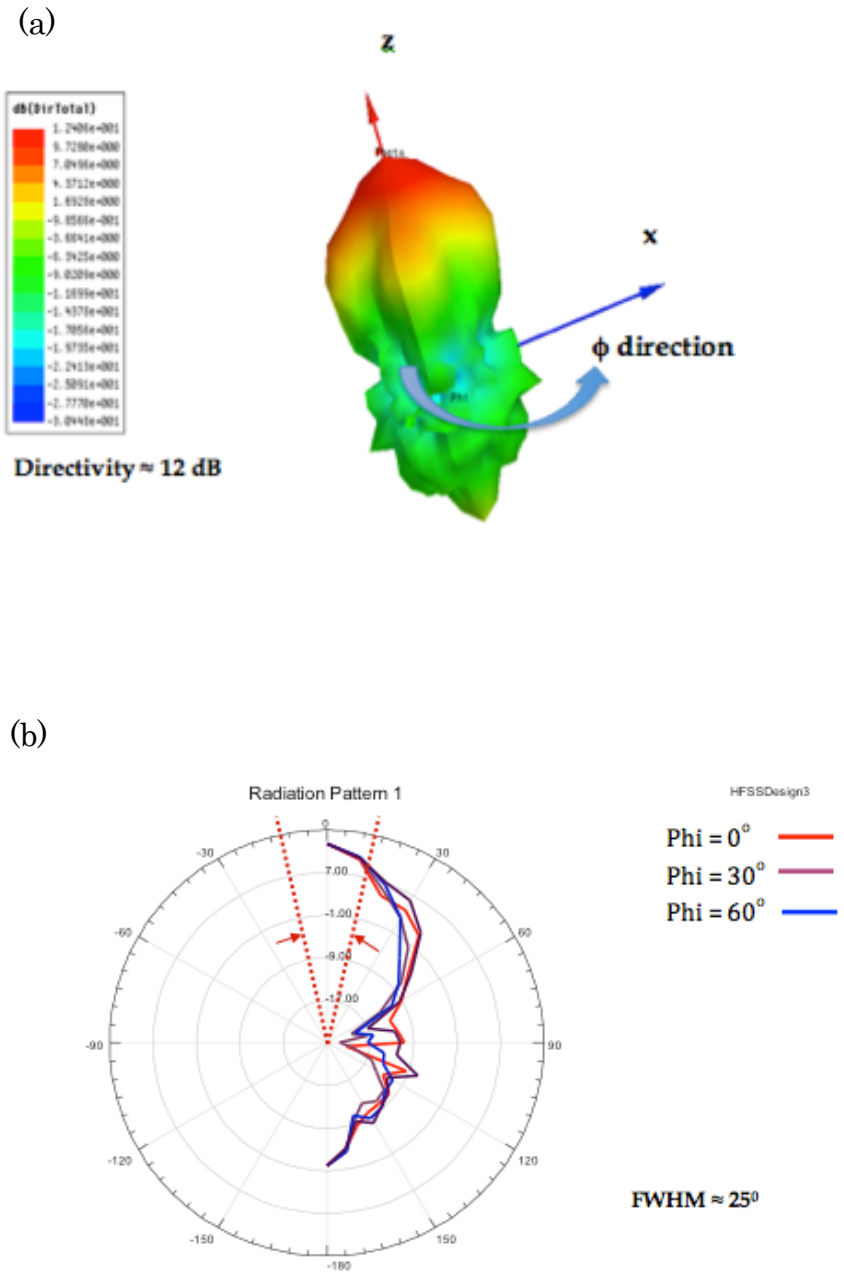

Figure 2.6: (a) Directivity of THz radiation beam pattern in the direction perpendicular to the plane of the antenna, z. (b) Cross section of beam pattern for different angles of □.

2.4. Summary

There are a variety of THz sources available, but most tend to be bulky and cumbersome. The most promising THz sources for a portable system are solid-state devices. For the lower end of the THz region (approximately 0.1 – 0.2 THz), monolithic microwave integrated circuits (MMIC) prove to be the most successful. For higher frequencies up to 0.3 THz, InP Gunn diodes and impact ionization avalanche transit time (IMPATT) diodes have generated CW power up to 10 mW [8]. Above 0.3 THz, GaAs photomixers have shown success as photoconductive sources but at an operational wavelength of 800 nm. In order for the photoconductive source to be compatible with 1.55 μm fiber technology, InGaAs on InP substrate was chosen as the material since the photon energy of 1.55 μm light ($h\upsilon$ = 0.80 eV) is above the absorption threshold of $In_{0.53}Ga_{0.47}As$, that has a bandgap of 0.75 eV. The antenna was designed to generate THz power up to 1.35 THz when optically excited by a 1.55 μm mode-locked laser. The dimensions of the antenna determined the range of frequency of the THz power generated by the photoconductive switch. However, the antenna design was limited by chip size. The performance of the photoconductive switch packaged on a hyperhemispherical Si lens was simulated using HFSS. This photoconductive switch showed promise to be a successful THz source.

2.5. References

1. N. Orihashi, S. Suzuki, and M. Asada, "One THz harmonic oscillation of resonant tunneling diodes," Appl. Phys. Lett., Vol. 87, p. 233501-1 - 233501-3 (2005).

2. G. Ramian, "New UCSB free-electron lasers," Nucl. Instrum Methods Phys. Res. Sect A, Vol. 318 p 225 -225 (1992).

3. N. Karpowicz, H. Zhong, C. Zhang, K.-I Lin, J-S Hwang, J. Xu, X.C. Zhang, "Compact continuous-wave subterahertz system for inspection applications," Appl. Phys. Lett., Vol. 86, p 1-3, (2005)

4. Paoloni, Claudio, Mineo, Mauro, Di Carlo, "Vacuum electron tubes for THz applications," 2011 30th URSI General Assembly and Scientific Symposium, URSIGASS; Article number: 6050398; Publisher: IEEE Computer Society.

5. J. Faist, F. Capasso, D. L. Sivco, C. Sirtori, A. L. Hutchinson and A. Y. Cho "Quantum Cascade Laser,", Science, Vol. 264 no. 5158 p. 553-556 (1994).

6. W. W. Bewley, C. L. Canedy, C. S. Kim, M. Kim, C. D. Merritt, J. Abell, I. Vurgaftman, and J. R. Meyer, "Continuous-wave interband cascade lasers operating above room temperature at λ = 4.7-5.6 µm," Optics Express, Vol. 20, p. 3235 -3240 (2012).

7. W. Walukiewicz, Z. Liliental-Weber, J. Jasinski, M. Almonte, A. Prasad, E. E. Haller, E. R. Weber, P. Grenier and J. F. Whitaker, "High resistivity and ultrafast carrier lifetime in argon implanted GaAs," Appl. Phys. Lett., Vol. 69,p. 2569 – 2571 (1996).

8. E. R. Brown, "THz generation by photomixing in ultrafast conductors,"Anal. Bioanal Chem, International Journal of High Speed Electronics and Systems, Vol. 13, p. 147 – 195 (2003).

9. M. Suzuki and M. Tonouchi, "Fe-implanted InGaAs terahertz emitters for 1.56 µm wavelength excitation," Appl. Phys. Lett., Vol. 86, p. 1104-1106 (2005).

10. N. Chimot, J. Mangeney,a L. Joulaud,P. Crozat, H. Bernas, K. Blary and J. F. Lampin, "Terahertz radiation from heavy-ion-irradiated $In_{0.53}Ga_{0.47}As$ photoconductive antenna excited at 1.55 μm," Appl. Phys. Lett., Vol. 87, p. 193510 (2005).

11. M. P. Hanson, S. R. Bank, J. M. O. Zide, J. D. Zimmerman, A. C. Gossard, "Controlling electronic properties of epitaxial nanocomposites of dissimilar materials, J Cryst. Growth, Vol 301-302, p. 4-9, (2007).

12. M. Sukhotin, E. R. Brown, D. Driscoll, M. Hanson, and A. C. Gossard, "Picosecond photocarrier-lifetime in ErAs:InGaAs at 1.55 μm," Appl. Phys. Lett., Vol. 83, p. 3921-3923 (2003).

13. D.C. Driscoll, M.P. Hanson, A.C. Gossard, and E.R. Brown, "Ultrafast photoresponse at 1.55 micron in InGaAs with embedded semimetallic ErAs nanoparticles," Appl. Phys. Lett. Vol. 86, No. 5, (2005).

14. M. Sukhotin, E. R. Brown, A. C. Gossard, D. Driscoll, M. Hanson, P. Maker, and R. Muller, "Photomixing and photoconductor measurements on ErAs/InGaAs at 1.55 μm" Appl. Phys. Lett., Vol. 82, p. 3116-3118 (2003).

15. M. Hanson, Ph.D. Dissertation, University of California, Santa Barbara (2007).

16. J. M. Zide, D. O. Klenov, S. Stemmer, A.C. Gossard, G. Zeng, J. E. Bowers, D. Vashaee, and A. Shakouri, "Thermoelectric power factor in semiconductors with buried epitaxial semimetallic nanoparticles," Appl. Phys. Lett., Vol. 87, p. 112102 (2005).

17. D.C. Driscoll, M.P. Hanson, E. Muller, and A.C. Gossard, "Carrier compensation in semiconductors with buried metallic nanoparticles," J Appl. Phys. Vol. 97 (2005).

18. S. Adachi, "Physical Properties of III-V Semiconductor Compounds," Wiley, New York, 1982.

19. V. Rumsey, "Frequency independent antenna," Academic Press, New York, 1966.

20. Wiley, “Helical and spiral antennas: A numerical approach,” New York, 1987.

21. J.E. Bjarnason, T.L.J. Chan, A.W.M. Lee, E.R. Brown, D.C. Driscoll, M.P. Hanson, A.C. Gossard, and R.E. Muller, “ErAs:GaAs photomixer with two-decade tenability and 12-microwatt peak output power,” Appl. Phys. Lett., Vol. 85 , p. 3983-3985 (2005).

22. E.R Brown, A.W.M. Lee, B.S. Navi, and J.E. Bjarnason, “Charaterization of a planar self-complementary square-spiral antenna in the THz region,” Microwave and Optical Technology Letters, Vol. 48, p. 524-529 (2006).

3. Fabrication and Performance

3.1. Fabrication of Photoconductive Source

As mentioned in the previous chapter, an antenna was used to couple the THz power from the InGaAs photoconductive gap into free space. The semiconductor industry has made progressive leaps and bounds in recent past, especially in the fields of material growth, design and fabrication. Therefore, the methods used for metal deposition have become more efficient, reproducible and reliable. Three important things are required for successful processing are (1) the accuracy of your mask design, (2) fast liftoff rates, and (3) a high yield of devices. A quarter of a clean 2 x 2 inch wafer of the InGaAs material was used to fabricate the photoconductive switches. Positive photoresist (AZ-4210) was spun on the material for 30 seconds at a speed of 3000 revolutions per minute (RPM). After spinning the photoresist, there would always be a build up of photoresist, an edge bead, at the wafer edge. The increased thickness of the edge bead has a negative effect on processing since it increases the distance between the mask and the sample. This leads to an imperfect projection of the mask with undefined edges. Therefore, the edge bead was removed delicately using a razor blade by scraping the edges of the wafer. After the removal of the edge bead, the wafer was placed on an

oven and soft-baked at 95 degrees Celsius for 60 seconds. Soft-baking was done to remove the solvent from the photoresist, which makes the photoresist photosensitive or imageable. After soft-baking, the square spiral antenna was patterned on the material with a photolithographic aligner model 3 Karl Suss MJB-3 using a chrome mask. The wafer was exposed for 15 seconds to UV light. For positive photoresist, the long-chained photoresist that is exposed to the UV light is optically reduced to shorter chains and gets removed when exposed to the developer. Therefore, the designed mask had the square spiral antenna transparent and the rest of the mask opaque in order to pattern the antenna on the material. The sample was then developed in AZ-400K diluted 1:4 for 50 to 60 seconds, followed by rinsing with deionizing (DI) water and blow-drying with nitrogen. The developer only dissolved the photoresist that was exposed to UV light, which resulted in the square spiral antenna pattern on the sample. Therefore, square spiral pattern was exposed InGaAs material, while the rest of the sample was covered in photoresist. The sample was then inspected under a microscope to verify that the pattern was successfully developed. If not, the sample was placed back in the developer until crisp clean patterns emerged.

After photolithography, the native oxide was removed in order to get high quality ohmic contacts. Therefore, before metal was deposited

on the sample, the sample was cleaned in a 1:10 hydrochloric acid (HCl) to DI water for 30 seconds then dried with a nitrogen gun. Electron beam metal deposition was used to deposit the metal contacts on the sample in a steady and controlled manner. The contact metals used were titanium (Ti), platinum (Pt) and gold (Au). The Ti and Pt were used for adhesion purposes, and the gold was used for conductive purposes. A thickness of 500 Å of Ti was deposited at a rate of 4 Å per minute. Followed by a thickness of 1500 Å of Pt at a rate of 5 Å per minute. Followed by 3000 Å of Au at a rate of 7 Å per minute for a total thickness of 5000 Å of metal deposition. This thickness had proved robust during wire bonding the photoconductive switch, which is necessary for packaging the device. After metal deposition, the unwanted metals (i.e metals on the photoresist layer) were removed from the sample by a lift-off process. The sample was first placed in acetone and then placed in an ultrasonic bath for 5 minutes. The sample was then removed from the acetone and placed in isopropanol, and also put in an ultrasonic bath. This was done until the unwanted metals were completely removed from the sample via the stripping (or liftoff) of the remaining photoresist. The device was then washed in DI water and dried with a nitrogen gun. The metals were successfully deposited on the InGaAs material; the photoconductive switch was fabricated. The fabricated wafer was then diced up using a

disco dicing saw to create 3.75 mm x 3.75 mm squares with individual photoconductive switches.

3.2. DC Characteristics

As discussed in the previous chapter, the square spiral antenna pattern has proven a very efficient as a planar antenna for THz photoconductive switches. However, it is also useful for dc characterization because it provides a well-defined geometrical method for calculating the electrical conductance. The conductance of the photoconductive switch is given below in equation 3.1.

$$G = \frac{1}{R} \approx \frac{N_s}{\rho_s} = \frac{N_s * t}{\rho} \qquad 3.1$$

R is the measured resistance, N_S is the number of squares (293), ρ_S is the sheet resistance (Ω/sq), and ρ is the corresponding bulk resistivity [Ω -m] [1]. The devices were electrically characterized over a wide range of temperatures in order to investigate the resistivity of the photoconductive switch. The sample was mounted on the copper cold finger of a Gifford-McMahon helium-4 refrigerator using thermal grease (Apiezon N) for good thermal conductance. The temperature was monitored with a silicon diode mounted in the same cold finger in close proximity to the sample under test. The zero-bias electric conductance was measured using a source meter in constant-voltage mode.

Measurements were then taken as the temperature of the cold finger dropped from room temperature. Experiments were performed to measure the resistance, R, versus temperature over the largest range possible.

Figure 3.1 shows the bulk resistivity derived with the formula $r = R * N_S * t$ (Eq. 3.1), with $N_S = 293$ and $t = 2$ micron versus temperature of the photoconductive switch. The room-temperature value of 13.3 Ω -cm agreed well with the separate Hall measurements value of 13.1 Ω -cm (see chapter 2).

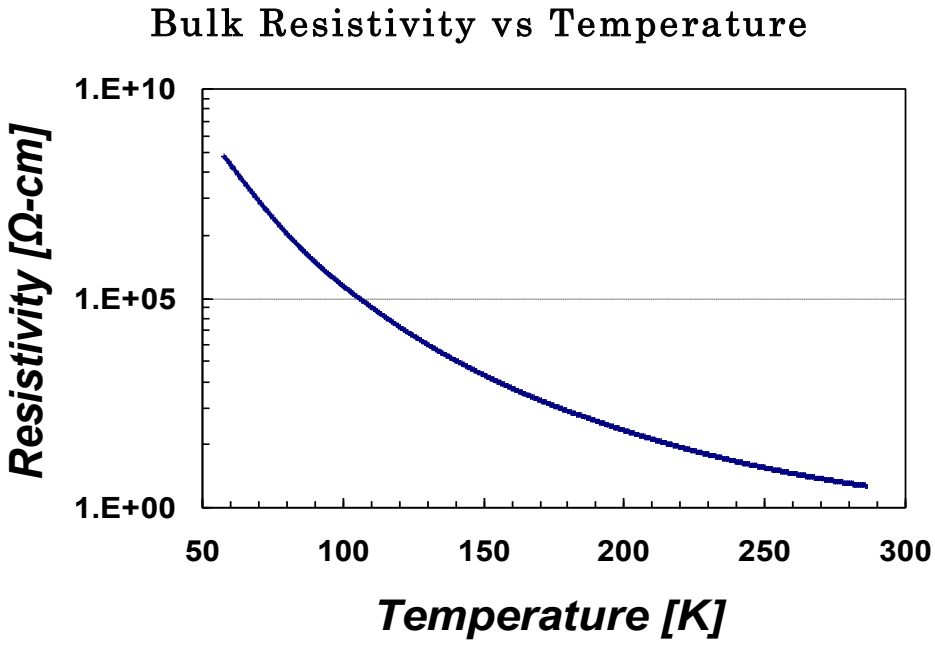

Figure 3.1: Bulk Resistivity vs Temperature of the photoconductive switch.

The resistivity of the InGaAs material increased exponentially as the temperature decreased; a decrease in 60 K resulted in an order of magnitude increase of the resistivity. The resistivities of this material at lower temperatures were now comparable, than the resistivity of ErAs:GaAs at room temperature. ErAs:GaAs materials having the same square spiral antenna design have been known to have a zero bias dark resistance of 90 MΩ [2]. The increased resistivity of the InGaAs material at low temperature minimizes the dark current, which is critical to prevent thermal failure of the device.

A longstanding problem of ErAs:$In_XGa_{1-X}As$ nanocomposites is electrical breakdown at relatively low fields [3], particularly at the high indium fraction ($X \geq 53\%$), which is required for strong photoconductors in the popular 1.55-micron telecommunications band. With the advent of low-temperature-grown GaAs, metal precipitates or nanoparticles have been an effective way of producing ultrafast photocarrier recombination even in the presence of high-bias fields around 800 nm [4]. Part of the reason for this is the "soft" nature of the impact ionization that takes place. Unfortunately, impact ionization occurs much more readily in $In_{0.53}Ga_{0.47}As$ because of its smaller bandgap. The used structure is advantageous for high-field studies since at any given bias voltage V_B it presents a well defined maximum electric field of $E_{max} = V_B/W_G$, where

W_G is the gap distance (9.0 micron) between the arms. This field occurs just below the nanocomposite-air interface and is shown in Figure 3.2. [1].

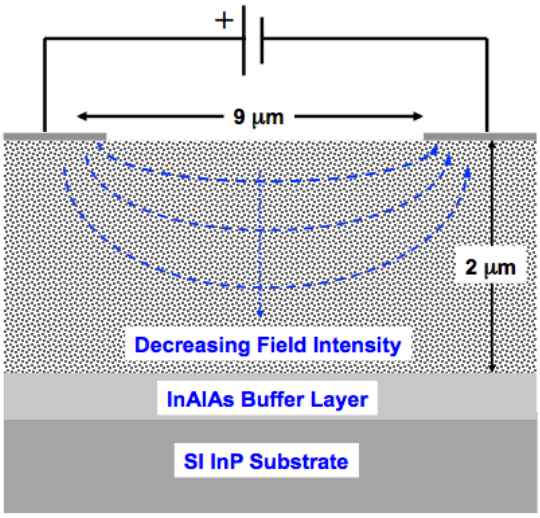

Figure 3.2: Cross-sectional view of electric lines of force in the gap region between adjacent arms of spiral.

As in most coplanar-electrode structures with equal and opposite electrostatic potential between them, the electric fields in the substrate follow ellipsoidal lines of force with the greatest field magnitudes at the surface, and progressively weaker magnitudes with depth in the material. This allows for determination of the threshold electric fields in critical transport effects, such as impact ionization. Therefore, since

device failure occurred at 23 V at 77 K, this would correspond to a breakdown E field of 2.6 x 10^4 V/cm.

An important aspect of any THz photoconductive device is its current-voltage characteristic at high bias. To further understand the dc characteristics of this material, experiments were done to obtain the dc current-voltage (I-V) behavior. The current-voltage curves of the test structure were obtained with the same source meter in constant current mode since this enabled stable measurement collection in the event of bias-voltage critical effects. Such effects were anticipated for the present sample based on experience with similar nanocomposite material in THz photomixer structures [5].

As in many metal-semiconductor interfaces, the I-V curve reveals information regarding the electrical contact behavior. Figure 3.3 shows the room temperature I-V curve and differential resistance versus bias voltage for a photoconductive switch. The linear I-V curve shows that the contact is Ohmic, and that the bulk material determines the measured resistance. However, as the voltage increases, there is a threshold where the current increases rapidly and the differential resistance falls to zero. This is the non-ohmic behavior regime and is what is referred to as a soft breakdown or device failure due to impact ionization. These devices displayed failure at approximately 8 V at room temperature, with a

corresponding dark current of ~ 100 mA. This high dark current was a serious impediment to device performance at room temperature, since THz power generation relies on reduced dark current; a dark current on the order of 10s of μA is low enough to generate THz power [6]. The square spiral antenna was designed to have high driving point resistance, ranging from 200 Ω to 350 Ω across a large bandwidth, and consequently can efficiently couple to high impedance sources like the photoconductive switch. The differential resistance measured at room temperature for the photoconductive switch was 322 Ω.

(a)

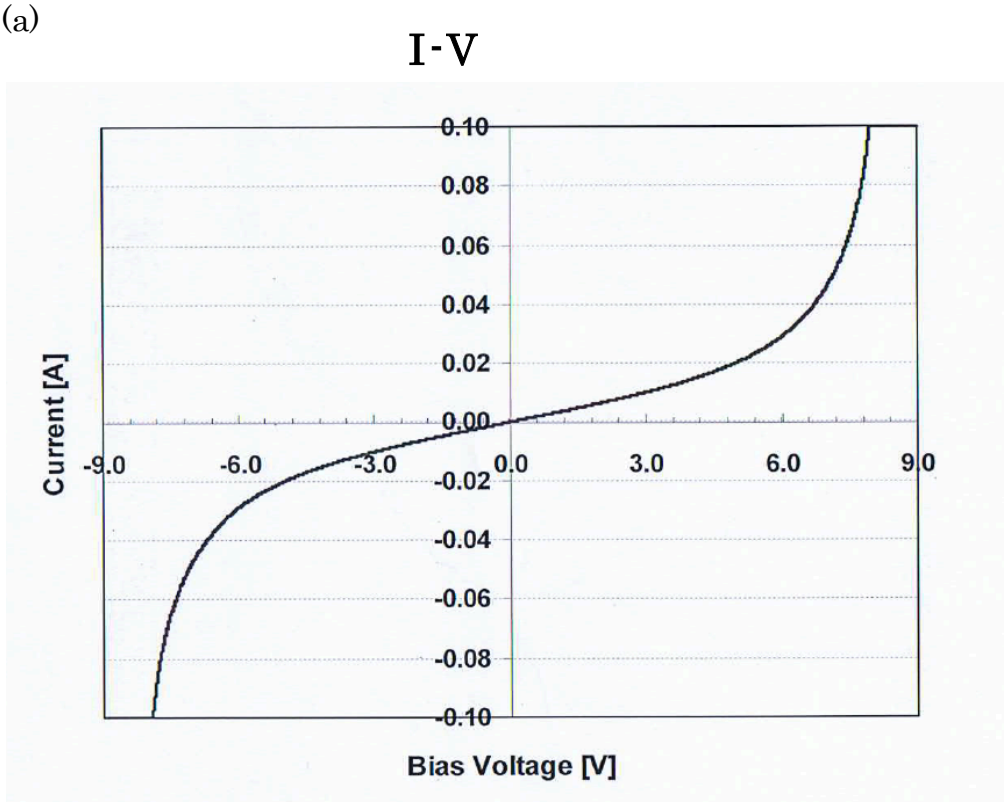

(b)

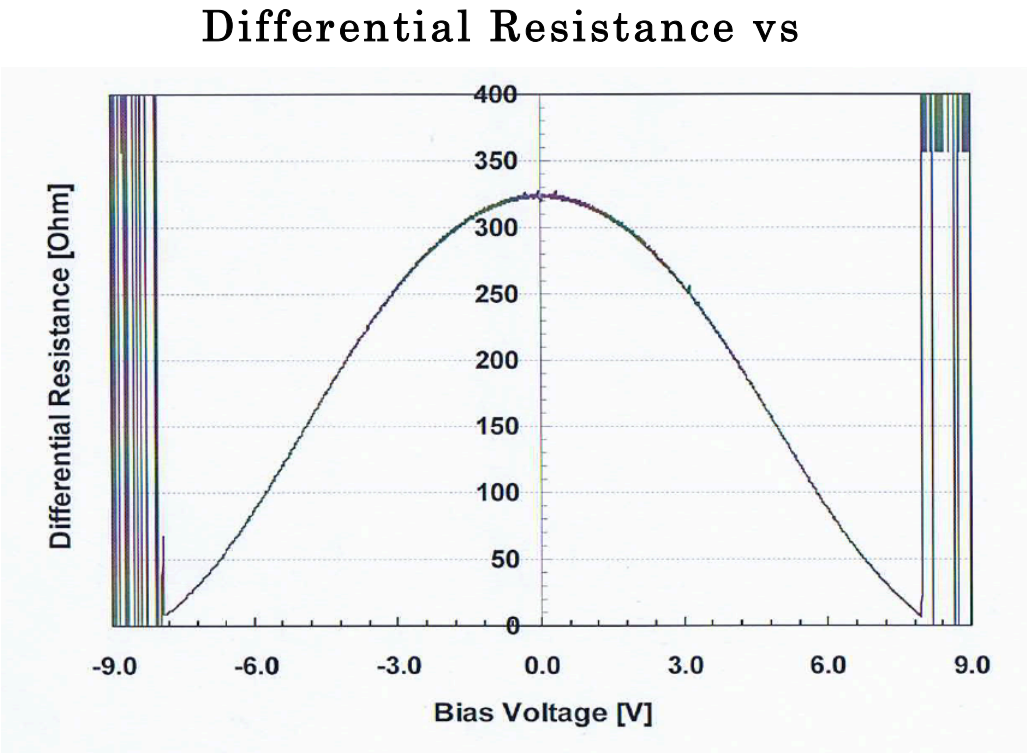

Figure 3.3: (a) I-V curve of a photoconductive switch at room temperature. (b) Differential resistance vs Voltage for a photoconductive switch at room temperature.

I-V characteristics were taken over a range of temperatures to analyze the performance of the photoconductive switch as the temperature was decreased. Figure 3.4 shows the I-V curve acquired at 200 K. Lowering the temperature to 200 K raised the maximum achievable DC bias to 13 V with an observed dark current of 7 mA. While much lower

than the room temperature operation, this dark current is still large enough to adversely effect THz generation.

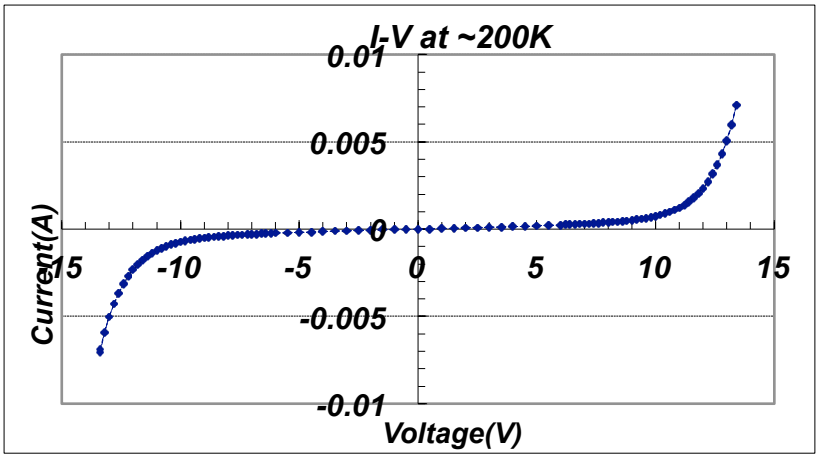

Figure 3.4: I-V curve of photoconductive switch at 200 K.

Figure 3.5 shows the I-V curve acquired at 150 K. A further decrease of the temperature to 150 K increased the maximum DC bias to 18 V. The dark current decreased to 0.003 mA at 13 V, which was significantly lower than the 7 mA that occurred at 200 K.

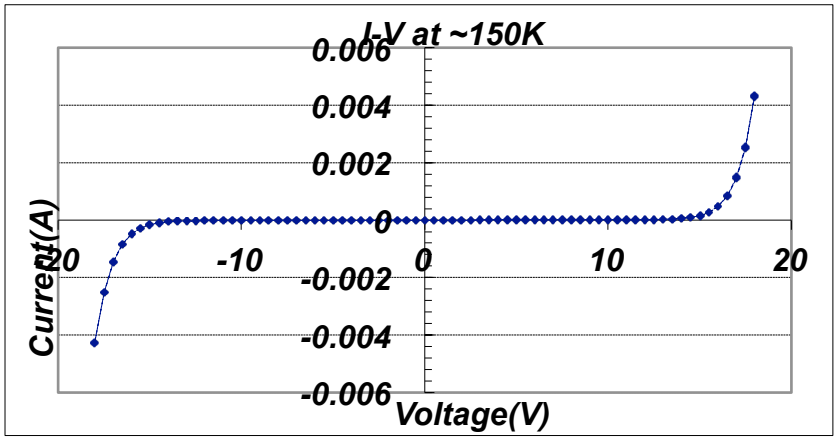

Figure 3.5: I-V curve of photoconductive switch at 150 K.

Figure 3.6 shows the I-V curve acquired at 80 K. At 80 K, the device could accept bias up to 23 V, which is roughly three times the bias of room temperature. The dark current was now reduced to microamps, which is a significant improvement from milliamps at room temperature. The photoconductive switch at a temperature of 80 K displayed high resistivity, hence, low dark current; it could withstand high bias voltage all while maintaining subpicosecond carrier lifetimes. It met the criteria to generate THz power.

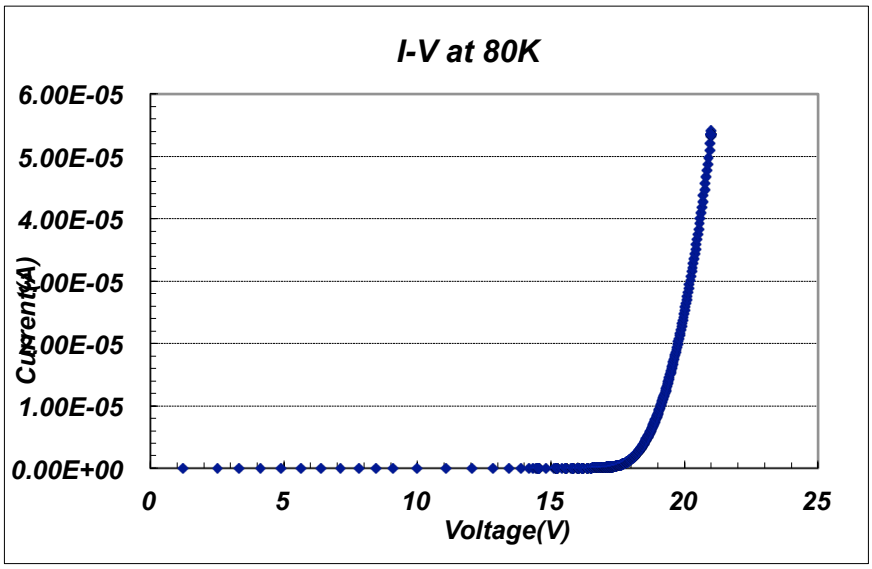

Figure 3.6: I-V curve of photoconductive switch at 150 K.

Figure 3.7 shows the I-V curves of a ErAs: $In_{0.53}Ga_{0.47}As$ photoconductive switch at 80 K, 150 K, 200 K, and 250 K without incident laser power. At a given bias voltage, the current increases with temperature. For

example, at 5 V, the dark current increases nearly six orders of magnitude between 80 K and 250 K. At 200 K, 150 K, and 80 K, the device entered break down at approximately 13 V, 18 V and 23 V respectively. Therefore, the device broke down at a critical electric field of approximately 1.4 x 10^4 V/cm, 2 x 10^4 V/cm, 2.6 x 10^4 V/cm.

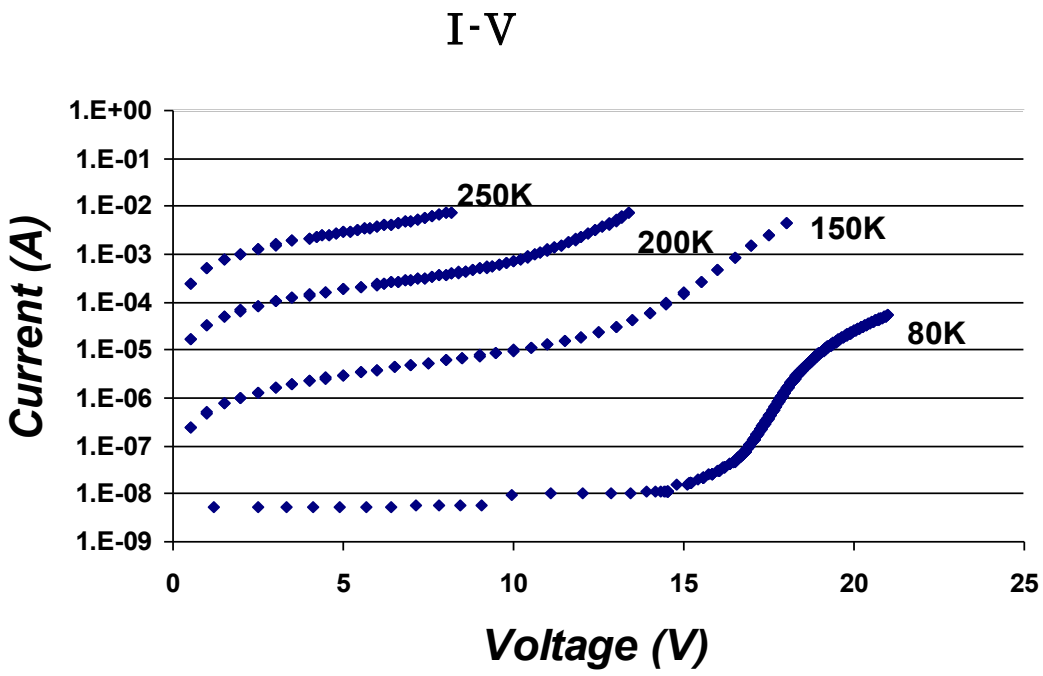

Figure 3.7: I-V curve of ErAs: $In_{0.53}Ga_{0.47}As$ device at 80K, 150K, 200K and 250K.

3.3. Lifetime Measurement

The superior performance of LTG-GaAs photoconductive sources is generally attributed to high dark resistivities and subpicosecond lifetimes [7]. ErAs has been used in both GaAs and InGaAs to act as

recombination sites in order to reduce the photocarrier lifetime [8]. Due to the high charge concentration in ErAs: InGaAs superlattices, the photocarrier lifetimes are longer compared to that of ErAs:GaAs. The ErAs:InGaAs was doped with p(Be) to compensate for the high n-doped background. In order to ensure that the material had subpicosend photocarrier lifetime, it was measured at 1.55 μm using a pump-probe phototransmission technique. The mode-locked laser pulses were sent through a 20 dB fiber splitter to create a pump and probe beam. The pump beam was focused on the InGaAs material after passing through an optical chopper, which was used as a reference signal for the lock-in amplifier. The probe beam was passed through a variable delay line and also focused on the sample. Both pump and probe beams were focused on the sample using fiber to free space couplers. The pump beam excites the photocarriers, which modulates the transmission of the probe beam. A photodiode along with a lock-in amplifier was used to detect the transmitted probe beam. The average probe-beam signal was measured as a function of the pump-probe time delay in order to obtain the differential transmission spectra. The delay signal was fit with the expression $I_0 \exp(-t/\tau)$, where τ is the lifetime. The experimental setup is shown in Figure 3.8.

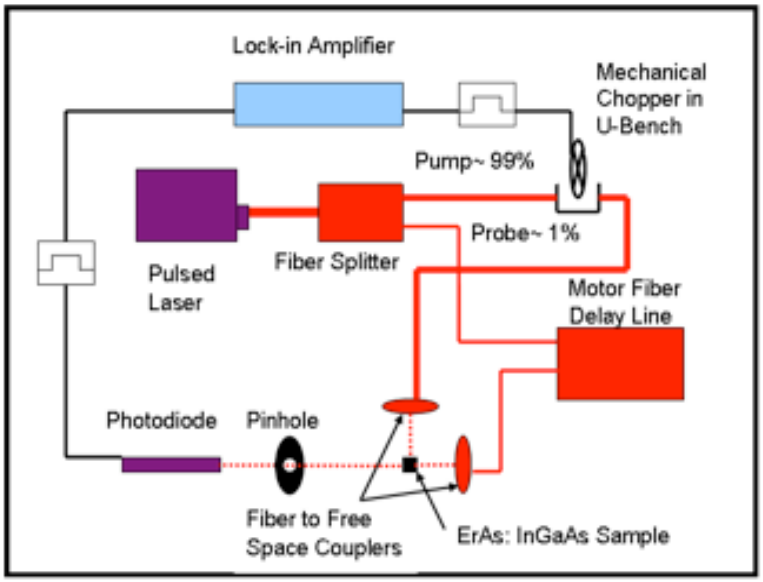

Figure 3.8: Lifetime measurement experimental setup.

Figure 3.9 shows the differential spectrum versus pump-probe time delay scan for the InGaAs material. The positive delay probe signal between 90% and 10% of the probe signal peak was fit to the exponential $I_0 \exp(-t/\tau)$, resulting in a fit value for the lifetime, $\tau = 0.73$ ps.

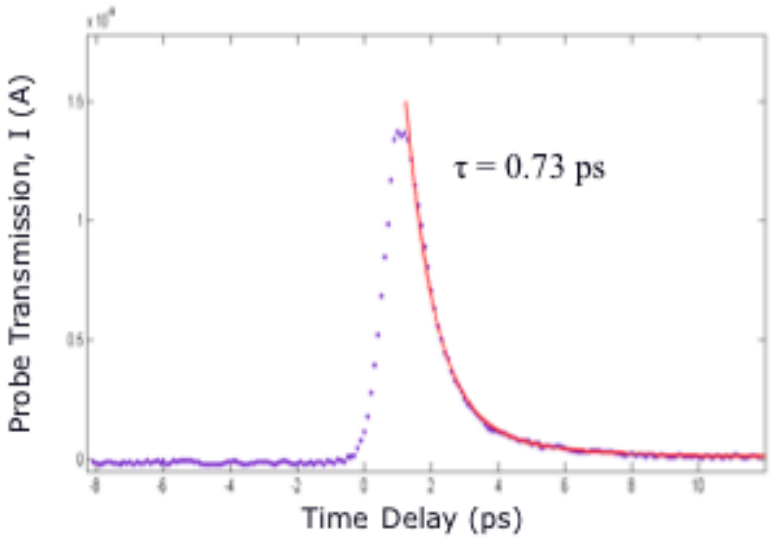

Figure 3.9: Differential transmission spectrum versus pump-probe time delay.

3.4. THz Power

The photoconductive switch was packaged with optics and bias lines prior to THz measurements. The device was mounted on the backside of a silicon hyperhemispherical lens in an aluminum mount. Experiments were performed at low temperatures, so aluminum was chosen because it is a good thermal conductor and compatible with the 77 K cryostat. Gold wires were then connected to the bias pads of the photoconductive switch and to bias terminals by use of conductive silver paint. Figure 3.10 shows photographs of both the front side and reverse side of a packaged photoconductive switch on Si hyperhemispherical lens.

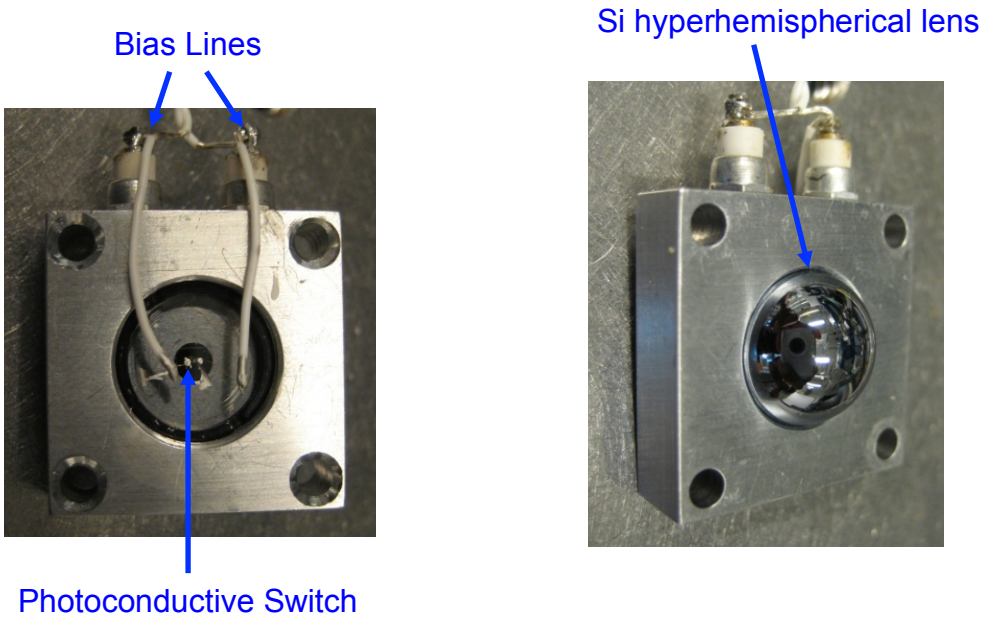

Figure 3.10: Photographs of the front and reverse side of a packaged photoconductive switch on Si hyperhemispherical lens.

The packaged device was then mounted on the copper cold finger in a liquid nitrogen 77 K Janis cryostat. In order to lower the temperature to 77 K, a vacuum pump was used to reduce the pressure inside the cryostat to 10^{-4} torr. This low pressure was needed in order to maximize the temperature drop and a liquid nitrogen hold time of 5 hours. The cryostat was connected to a temperature controller to monitor the temperature. One of the windows of the cryostat was designed as an electrical feedthrough to give the capability of biasing the device. Another window was a quarter inch thick Teflon, which is transparent to THz power, since the THz power needed to be detected outside of the cryostat. The final two windows were made of quartz and sapphire. The packaged device was then optically pumped with a PolarOnyx 1.55 μm fiber mode-locked laser. Experiments were done with an optical power of 140 mW. The mode-locked laser displayed a pulse width of 80 fs and a pulse repetition frequency of 46 MHz. Maximizing the photocurrent was needed to maximize the THz power. Maximum photocurrent was achieved by exciting the center (photoconductive gap) of the square spiral antenna. The laser was set up outside the cryostat and the beam was focused on the photoconductive gap of the device inside cryostat through a sapphire window using free-space optics. The photoconductive switch

was connected to an oscilloscope to monitor the photocurrent and locate the center of the antenna.

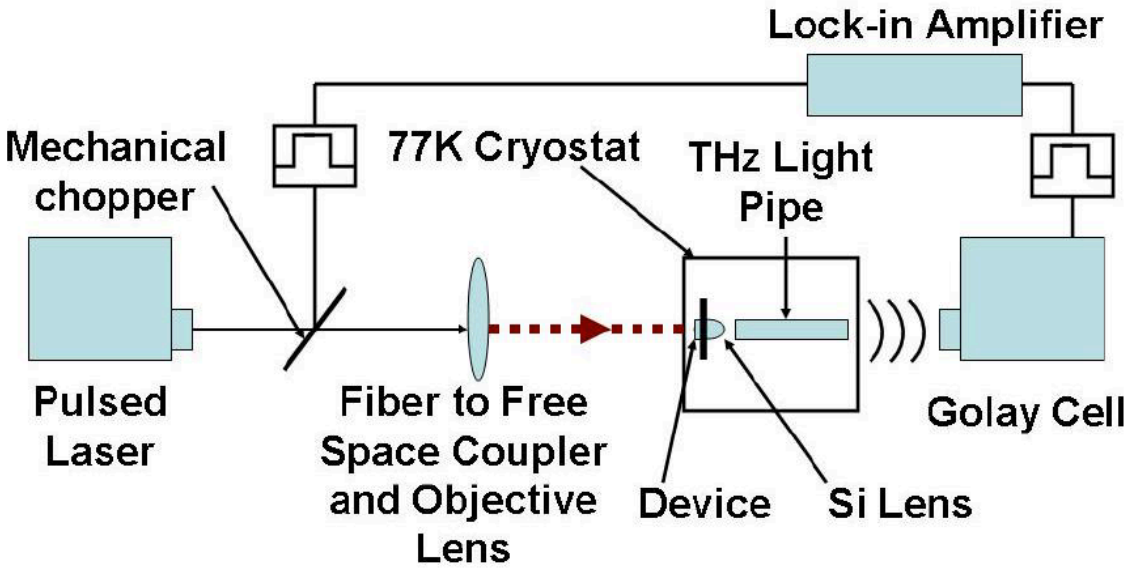

Figure 3.11: Experimental setup for InGaAs photoconductive switch generating THz power. The mechanical chopper provides a reference signal for the lock-in amplifier.

As shown in the block diagram of Figure 3.11, the THz radiation was coupled from the photoconductive switch through a polished brass tube (light pipe) and then a Teflon window (opposite the sapphire window) to a Golay cell in free space. The Golay cell had a 6 mm aperture and a nominal optical responsivity of ~ 10 mV/μW and a noise equivalent power of ~ 2 x 10^{-10} W Hz $^{-1/2}$ – both characterized at mid-IR wavelengths. It contained a thick black-polyethylene filter to block out the mid-IR radiation that can be generated by absorption of the 1.55 μm pump laser.

Previous calibration has shown that these performance values degrade about a factor of four between mid-IR and the portion of the THz region (λ = 0.5 to 3.0 mm) where the present experiments were conducted. The low AC modulation (<16 Hz) required by the Golay cell was provided by an optical chopper in a fiber-optic "U-bench" located outside the cryostat. The modulated THz radiation was measured with a lock-in amplifier and converted to absolute power using an overall responsivity of 10 mV/μW for the Golay cell. However, coupling the THz beam into the brass tube and through the Teflon window loses some THz power. The stated power measurements do not include this additional loss.

A broadband characterization with no spectral discrimination was performed first. The average output THz power of the device versus bias voltage at 77 K is plotted in Figure 3.12. The device was biased over a voltage range from 0 to 22 V. A maximum peak power of 11.38 μW was recorded at a bias of 22 V before the device failed at 23 V. This THz power was substantially higher than 0.8 μW reported by other InGaAs materials at 1.55 μm in recent times [9]. The failure mechanism is not yet understood but is certainly mediated by the optical pump power and associated photocurrent. The data was fitted with a quadratic polynomial, since the power should vary with the square of voltage. This is discussed in detailed in Chapter 5.

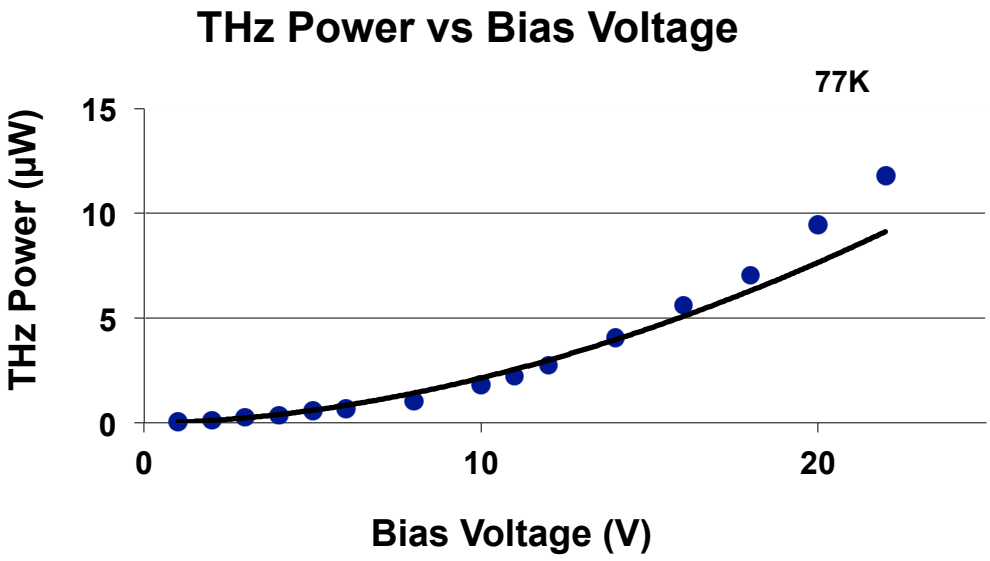

Figure 3.12: THz power versus bias voltage at 77 K biased up to 22 V pumped by a 1.55 μm fiber mode-locked with average power of 140 mW. The data is fitted with a quadratic polynomial.

Secondly, spectral discrimination of the THz power was achieved through the use of a custom designed quasi-optical bandpass-filter. The commercial filters (Virginia Diodes) are designed as frequency-selective surfaces in copper, and had center frequencies of 142, 193, 376, and 537 GHz. The transmission data of the filters are shown in Figure 3.13.

(a)

Filter #	1	2	3	4
Max Trans	0.63	0.53	0.74	0.99
Center Freq [GHz]	142	193	376	537
ENB [GHz]	60	139	165	128

(b)

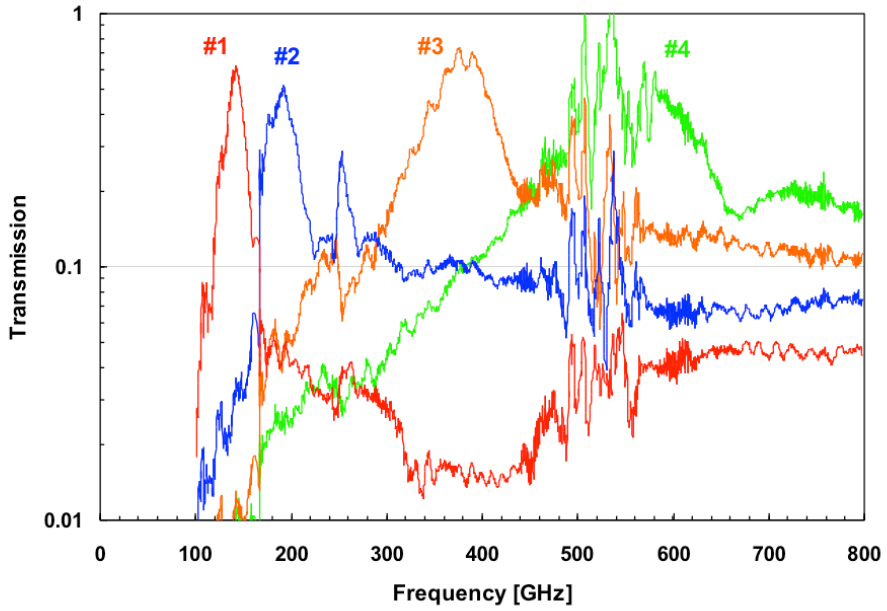

Figure 3.13: Data of the VDI commercial filters showing the center frequencies and bandwidths. (b). Transmission data of the VDI bandpass filters.

Each filter was placed sequentially between the cryostat and the Golay cell, and the power measurements were recorded for biases up to 22 V. The power for each measurement was normalized to the filter bandwidth and plotted versus frequency. Figure 3.14 shows the experimental setup of the free space optics focusing the 1.55 µm fiber mode-locked laser pulses on the photoconductive switch that is packaged on the copper cold finger in the 77 K Janis cryostat.

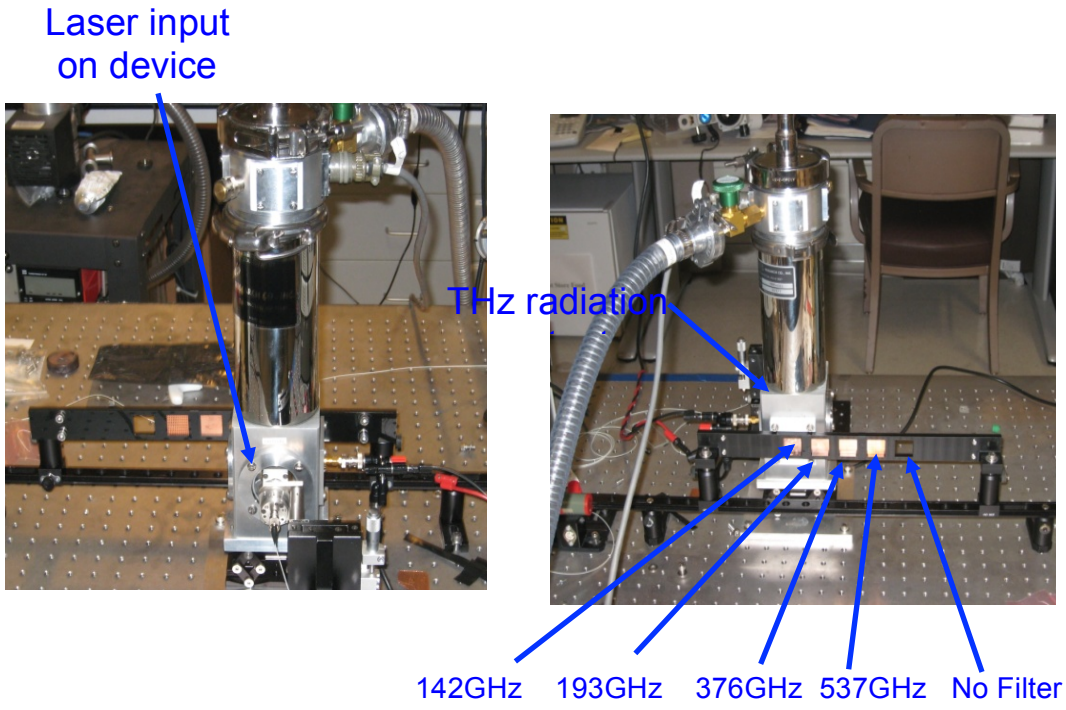

Figure 3.14: Laser input side of experimental setup. (b).THz output side showing the bandpass filters of the experimental setup.

The spectral power density plot for different bias voltages is shown in Figure 3.15. It shows a -3 dB bandwidth of approximately 350 GHz, and a consistent roll-off vs bias voltage. This suggests that the electron-hole lifetime in the ErAs: $In_{0.53}Ga_{0.47}As$ is independent of bias voltage. The photoconductive switch displayed reduced efficiency as the frequency was increased. However, the photoconductive switch performance is promising and a major step towards the application 1.55 µm fiber-laser and optical-component technology for THz generation.

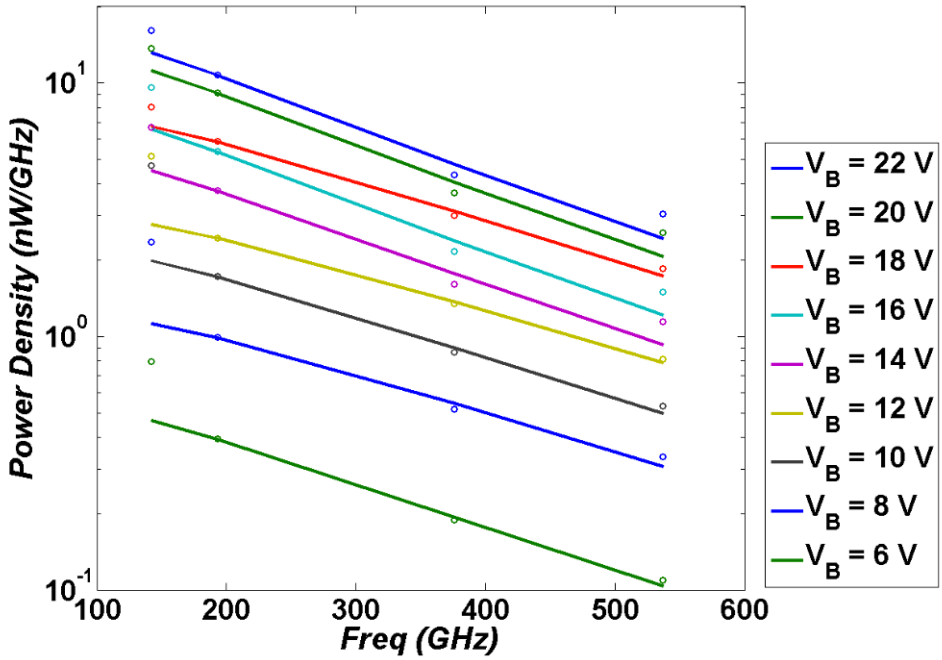

Figure 3.15: THz output power spectral density with fitted curves obtained from THz filter bank and normalized over the bandwidths.

3.5. Summary

The photoconductive switch was fabricated and the DC characteristics tested at room temperature down to 77 K. At lower temperatures, the material had high resistivity and an increase in breakdown voltage. The carrier lifetime of the material was measured using the pump-probe technique, which showed the InGaAs material had subpicosecond lifetime. The high resistivity, increase in breakdown voltage, and subpicosecond lifetime were essential in THz power generation. The THz power experimental setup was discussed in detail and a maximum peak power of 11.38 μW was achieved with no frequency selective filter. This power was markedly higher than other power levels reported with InGaAs at 1.55 μm [9]. However, at higher frequencies there was a slight roll off in THz power. Copper filters were used as frequency selective surfaces to obtain the power spectral density of the photoconductive switch. The photoconductive switch displayed a 3 dB bandwidth of 350 GHz. The power level of 11.38 μW was approximately 11 times bigger than the power needed for THz TDS.

3.6. References

1. E. R. Brown, K. K. Williams, W-D. Zhang, J. Suen, Hong Lu, J. Zide, and A.C. Gossard, "Electrical Transport in an Insulating Semimetal-Semiconductor Nanocomposite," IEEE Nanotechnology, Vol. 8, p. 402–407 (2009).

2. J. E. Bjarnason,a, T. L. J. Chan, A. W. M. Lee, E. R. Brown, D. C. Driscoll, M. Hanson, A. C. Gossard, and R. E. Muller, "ErAs:GaAs photomixer with two-decade tunability and 12 mW peak output power," Appl. Phys. Lett., Vol. 85, p. 3983 – 3985 (2004).

3. K-S.Hyun, C-Y. Park, "Breakdown characteristics in InP/InGaAs avalanche photodiode with p-i-n multiplication layer structure," Journal of Applied Physics, Vol. 81, p. 974 (1997).

4. K. A. McIntosh, K. B. Nichols, S. Verghese and E. R. Brown, "Investigation of ultrashort photocarrier relaxation times in low-temperature-grown GaAs." Appl. Phys. Lett. Vol. 70, p. 354 (1997).

5. S. P. Sundararajan, J.M. Steele, and N.J. Halas, "Propagation of surface plasmons on Ag and Cu extended one-dimensional arrays on silicon substrates," Appl. Phys. Lett., Vol. 88, p. 063115 (2006).

6. J.E. Bjarnason, T.L.J. Chan, A.W.M. Lee, E.R. Brown, D.C. Driscoll, M.P. Hanson, A.C. Gossard, and R.E. Muller, "ErAs:GaAs photomixer with two-decade tenability and 12-microwatt peak output power," Appl. Phys. Lett. Vol. 85 , pp 3983-3985 (2005).

7. M. Tani, K.-S. Lee, and X.-C. Zhang, "Detection of terahertz radiation with low-temperature-grown GaAs-based photoconductive antenna using 1.55 μm probe," Appl. Phys. Lett. Vol. 77, p. 1396 (2000).

8. D. C. Driscoll, Ph.D. Dissertation, University of California, Santa Barbara (2004).

9. J. Mangeney, P. Crozat, Ion-irradiated $In_{0.53}Ga_{0.47}As$ photoconductive antennas for THz generation and detection at 1.55 μm wavelength," C.R. Physique 9, pp 142-152 (2008).

4. Photoconductive Switch Array

4.1. Phased Array

The concept of a phased array of antennas goes as far back as early warning radar antennas used in World War II. Consider the British Chain Home early warning radar that could scan up to a range of 150 miles [1]. Back then engineers faced problems in steering the antenna beam, since this had to be done by physically moving the entire antenna. This means size was a serious limiting factor. A viable solution to this dilemma was to move away from a purely mechanical means of scanning the beam to an electronic way. The term phased array generally means an electronic or mechanical way of pointing a beam originating from an array in a desired direction. Phased arrays back then typically used a cumbersome setup of phase shifters in conductive-tube waveguides and centralized high power vacuum tubes. Then there was a shift towards using solid state technology to create phased arrays, which had the advantages of compact size, low cost, high reliability, and also introduced more applications.

In the search for obtaining a compact phased array for millimeter wave systems, designers came up with the idea of monolithic microwave integrated circuit (MMIC), which integrated the antennas, phase shifters,

and their circuitry on a single chip. Research has been done on microstrip patch antennas on a high dielectric constant substrate, such as GaAs. However, the thickness of GaAs required for the implementation of MMIC led to undesirable efficiencies and a narrow bandwidth; therefore, alternative methods were investigated [2]. One such of these methods was the active slot-line antenna integrated with high electron mobility transistor (HEMT) amplifiers on GaAs. This was not affected by substrate thickness [3]. By impedance matching of the drain-source port of the transistor to the input resistance of the radiator eliminated the matching circuitry resulting in smaller chip sizes. Using a pair of anti-resonant slot antennas (instead of resonant antennas) that also had matching impedance increased the bandwidth to allow operation up to 30 GHz. Another method was the integration of waveguide horn antennas consisting of a dipole suspended in a 1 μm etched pyramidal cavity in GaAs. This had an operational frequency up to 242 GHz [4]. Then there is the flip-chip back-face patches antenna that operates at 35 GHz [5]. This back-face patch antenna uses a thin film microstrip transmission line medium (TFMS) on a ground plane on the front of the chip with a thin dielectric deposited on top to form the substrate. The back face was metallized to create radiating elements, which are isolated from TFMS with ground planes. Connections between transmission lines

and radiating elements were achieved through GaAs via holes. This circumvented the substrate thickness issue and resulted in efficient radiation, improved bandwidth, and the capability to use a dielectric lens. Most MMIC research has been done with GaAs and has approached operational frequency up to 300 GHz. The problem with operating at higher frequencies is the availability of compatible planar detectors.

4.2. Array Packaging

The phased array in this thesis was fabricated on InGaAs on InP and was designed for frequencies up to 600 GHz. For testing individual devices, the pulses of the 1.55 μm mode-locked laser were focused on the photoconductive gap using free space optics outside the 77 K cryostat. However, for the photoconductive switch array, free space optics was substituted by a fiber array connected directly to the device. The fiber chosen for the experiment was a SMF-28 (single mode fiber) that supports 1.55 μm wavelength. The core of the fiber was 9 μm in diameter, so the antenna was redesigned using bigger square unit cells to better accommodate the pigtailing of the fiber to the center of the device. The new square spiral antenna was made up of 15 x 15 μm. An anvil was added to the photoconductive gap to aid in alignment of the fibers to the

photoconductive switch array. The anvil decreased the dimension in the photoconductive gap, which resulted in a spike in the photocurrent when excited by the mode-locked laser. Therefore, the spike in the photocurrent was an indication when the fiber was aligned with the photoconductive gap of each antenna of the photoconductive array. The new design is shown in Figure 4.1.

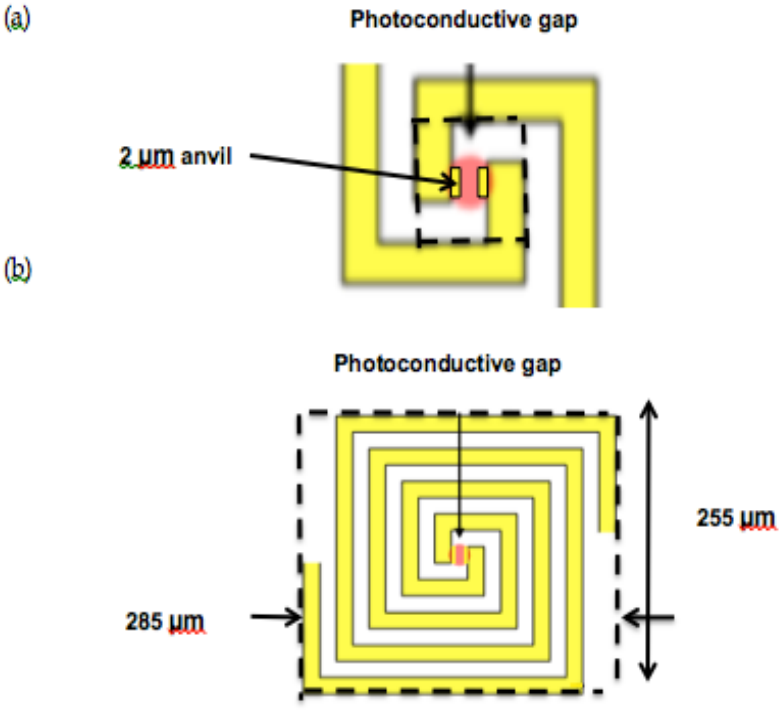

Figure 4.1: (a) Inner radiating dimensions that give rise to L_{min}. (b) Outer radiating dimensions that give rise to L_{max}..

For this designed square spiral antenna, L_{min} and L_{max} were 180 µm (15 x (3 + 3 + 3 + 3)) and 16200 µm (15 x (285 +255 + 285 + 255)) respectively [6]. This resulted in a f_{min} of approximately 7 GHz and a f_{max} of 609 GHz (see eq. 2.1 in chapter 2). A new mask was designed with the modified the square spiral antenna with the anvil being 2 µm wide and a gap of 11 x 15 µm. This mask contained patterns of a single square spiral antenna and photoconductive arrays of 2 and 4 square spiral antennas. The spacing between antennas was 500 µm. The photoconductive arrays were fabricated with the same process discussed in Chapter 3 and diced with a disco-dicing saw to separate each array. To ensure that fabrication was successful, I-V curves were taken of each antenna in the 4 source photoconductive array at room temperature. The results of the I-V curves are shown in Figure 4.2.

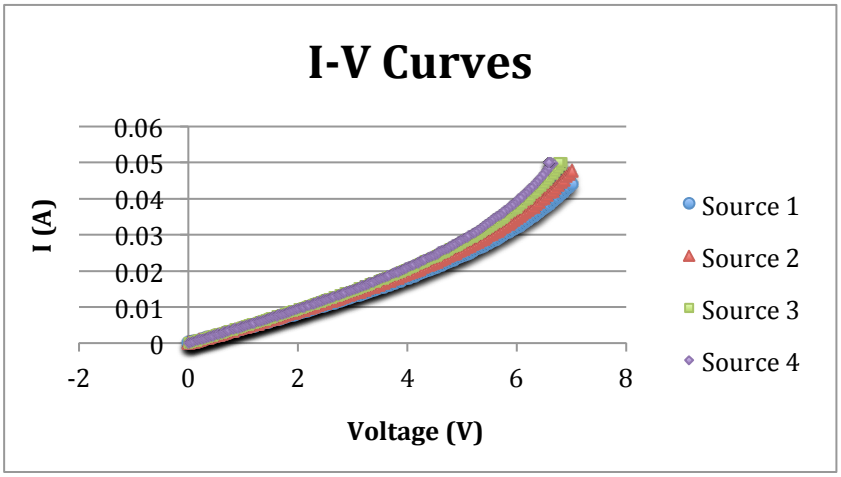

Figure 4.2: The I-V curves of each source of a 4 source photoconductive array measured at room temperature. Numbering of source goes from left to right.

Recall that I-V curves are expected to show a linear dependence (Ohmic contacts) and then a rapid increase in current as the device approaches breakdown. Based on previous experiments, device failure normally occurred at 8 V at room temperature, so care was taken to only bias the device up to 7 V. The I-V curves show that the sources were indeed approaching impact ionization at 7 V. The photoconductive switch array was then wire bonded with gold wires and conductive silver paint and packaged on the aluminum mount using the same methods discussed in Chapter 3.

One of the obstacles that needed to be addressed was how to attach a fiber array to ensure functionality under vacuum and at 77 K. Care needed to be taken to ensure that the setup was hermetically sealed to sustain the vacuum, which was required to achieve temperatures as low as 77 K with the cold finger. In addition, condensation would have occurred in the cryostat and affected the results of the experiment if cryostat was not hermetically sealed. The design included ASI9/125T fibers, which is a single mode fiber with a polymide buffer that supports 1.55 μm wavelength. There are two parts of the design: the ambient side, which is the part of the fiber setup that was outside the cryostat at room temperature, and the vacuum side, which is the part of the fiber setup that was inside the cryostat at 77 K. The vacuum portion of the fiber was

tested and designed to operate at the specified cold temperature of 77 K. It was also tested and made to withstand a vacuum pressure up to 10^{-6} torr, which is less than the pressure needed in the cryostat to attain a temperature of 77 K. In order to attain a hermetically sealed setup, the sapphire window was removed and replaced by an aluminum attachment that was fitted with an O-ring groove. The aluminum attachment was used to connect the cryostat to the designed fiber array with a rubber O-ring in place. The designed fiber array is shown in Figure 4.3 - Figure 4.5.

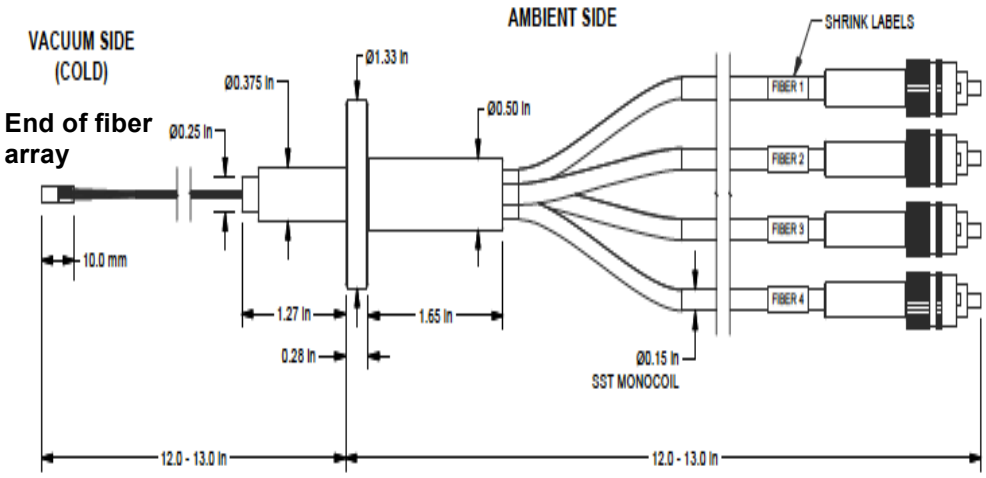

Figure 4.3: Designed fiber array to attach to cryostat and pigtail the photoconductive switch at a temperature of 77 K.

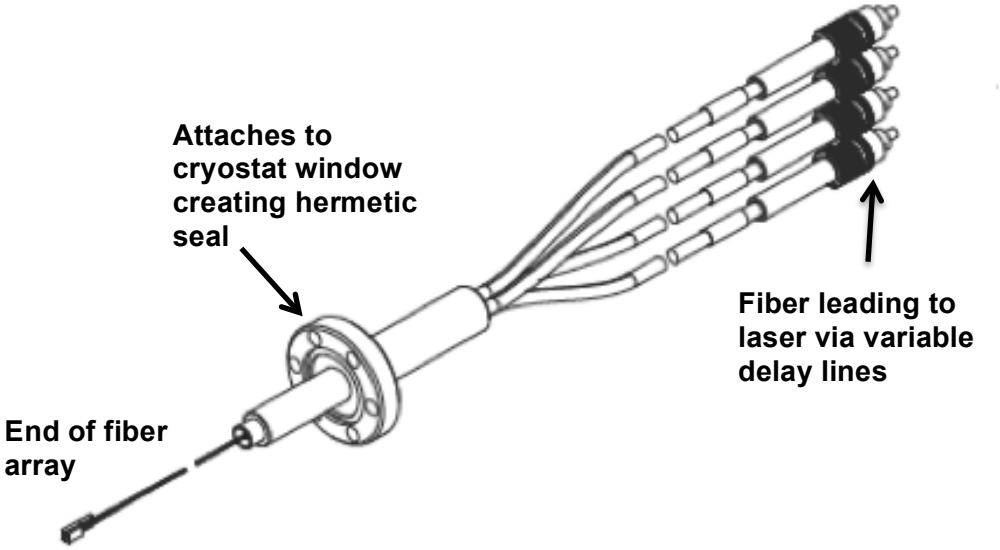

Figure 4.4: Alternate view of designed fiber array.

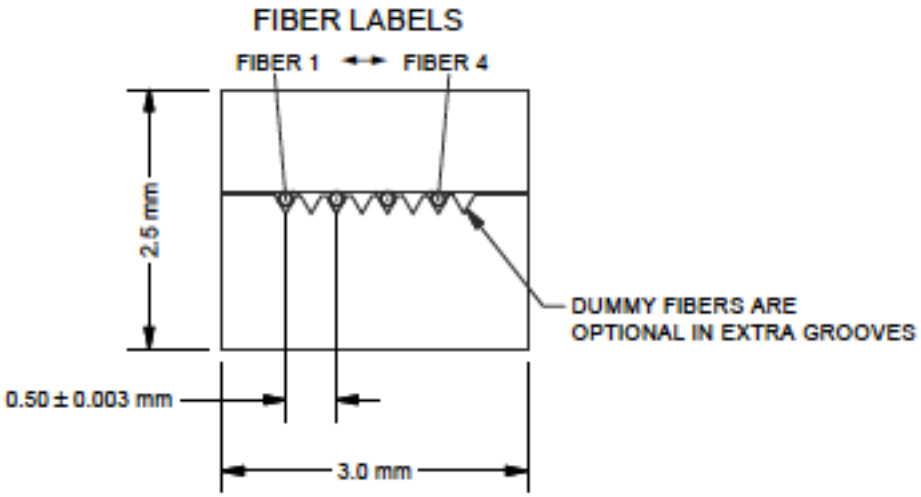

Figure 4.5: Blow up of the end of fiber array that are spaced at a designed distance 500 µm apart.

Figure 4.3 and Figure 4.4 show the designed fiber array showing the connection to the aluminum attachment creating a hermetic seal. The fibers were labeled 1 to 4 in order to keep track of which antenna was being excited by which fiber from the mode-locked laser. Figure 4.5 shows a zoomed in version of the actual fiber array. The fiber array has the same spacing as the antennas in photoconductive switch array in order to achieve proper alignment of the two. A test run was conducted with the designed fiber array connected to the cryostat in order to check if the vacuum pressure would hold and a temperature of 77 K obtained. It was successful on both counts. Figure 4.6 shows the actual designed fiber array attached to the cryostat.

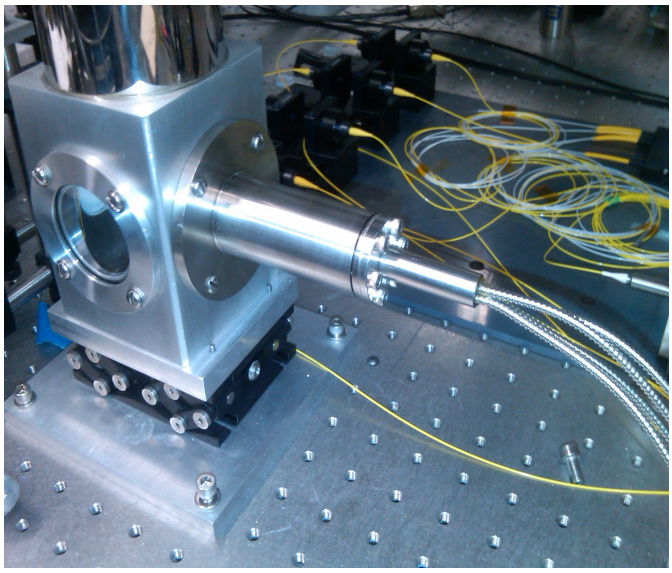

Figure 4.6: Actual fiber array design connected to the window of the cryostat via a designed aluminum window, which replaced the sapphire window.

Pigtailing the single mode fiber array to the photoconductive switch array had to be aligned with accuracy in the range of 3 µm. Improper alignment would result in coupling losses of the pulses to the photoconductive gap of each antenna in the photoconductive array. In order to maximize coupling of the two, the photoconductive switch array was connected to an oscilloscope to monitor the photocurrent, which was maximized for proper alignment. The photoconductive switch array and the fiber array were each mounted to translational stages in order to facilitate proper alignment. The fiber array was configured with a 1 x 4 V- groove FC connectors, in which the V-groove had a pitch of 500 µm ± 3 µm as shown in . A coarse alignment was first done using a fault locator. The 1.55 µm mode-locked laser was used to first illuminate only the leftmost antenna (Source 1). This induced a photocurrent in the antenna. The fiber array was controlled using the XYZ stage, which was used to translate the laser spot across the spiral antenna arms. THz power is maximized when the laser is incident on the driving point of the antenna (center gap), which was identified when there was a spike in the photocurrent due to the anvil. This process was done in iterative steps for all sources until all four sources were aligned. After alignment, a single component, low viscosity, UV curable adhesive was used to glue the fiber array to the photoconductive array. The UV curable adhesive

chosen also had a spectral transmission of over 98% between 420 nm and 1600 nm and was cured in 5 seconds with a 100 mW/cm^2 UV gun. Adhesive was added in increments until the two were fixed in a robust manner. The pigtailed fiber array to the photoconductive switch array was then mounted in the 77 K cryostat and was ready for experimental study.

4.3. Experimental Setup

This experiment was conducted in the time domain, which means the phase of THz radiation was controlled by delaying the arrival of the laser pulses to each antenna using optical delay lines. A series of 4 low loss, sub-picosecond OZ Optics ODL-200 fiber optic delay lines were used in this experiment. These delay lines consist of an input and an output fiber collimators to project the laser pulses into free space and then receive it again into the fiber. The separation between the input and output can be varied using a micrometer stage; thus controlling the distance the pulses travel in free space. The travel range was 25 mm, resulting in a delay of 83 ps with a resolution of 0.033 ps. The fiber from the laser was connected to a U-bench with a chopper, then to a 1 x 4 splitter, then to the optical delay lines, and terminated with the fiber

connectors connected to the photoconductive switch array. In order to match the optical path lengths, the fiber between the 1 x 4 splitter and the optical delay lines were physically measured and their lengths were spliced and kept as close as possible to each other. The optical path lengths for the optical delay lines were measured with an OZ Optics Optical Fiber Length Meter and were within 3 mm of each other, which is equivalent to the laser pulses being within 10 ps of each other. The experimental parts were mounted onto a 12" x 12" x 0.25" PVC sheet to maintain robustness and portability. This portion of the experimental setup is shown in Figure 4.7.

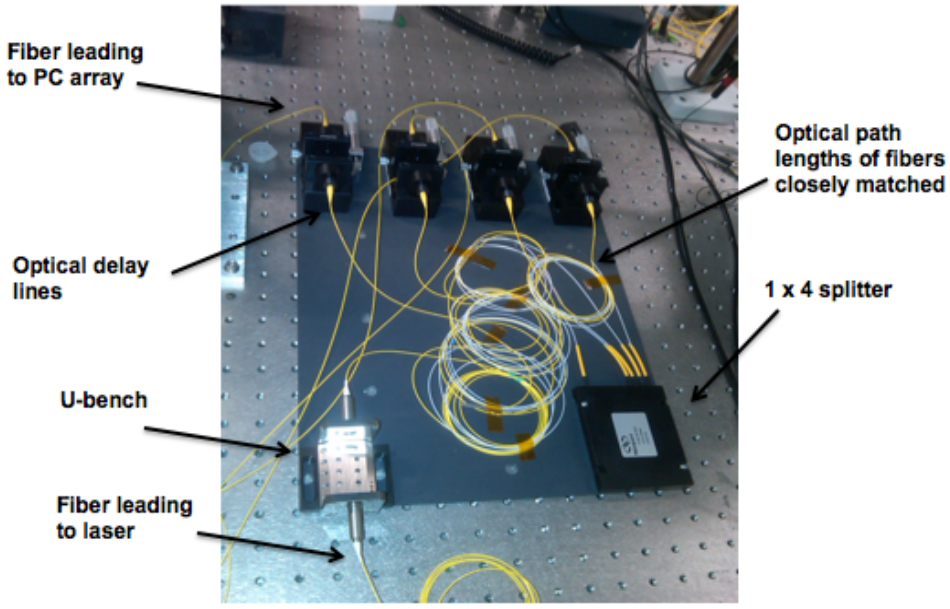

Figure 4.7: Optical delay line units, 1 x 4 splitter and U bench mounted on a PVC board before inserted in complete experimental setup.

In order to attain maximum THz power from the photoconductive array in the broadside direction, the laser pulses needed to arrive simultaneously at each source. The data sheet of the optical delay line stated that 1 mm of translation on the micrometer corresponds to 3.33 ps of time delay. Experiments were done using the Luna OBR 4400 (Optical Backscatter Reflectometer) to verify the consistency of the experimental setup. The OBR was used to tune out built in deviations in the fiber lengths to find the zero point of all the optical delay lines. This commercial tool scans reflected power and plots it versus time delay or optical path length. The OBR input was connected to one end of the optical delay line and a laser source swept through the experimental setup. Reflections will occur at surfaces encountered in the experimental setup such that a continuous detection of reflected power along the optical path is plotted versus time delay. Based on the knowledge of the physical setup, each reflection line that was detected was attributed to the respective surface in the experimental setup. The reflective surfaces that were used as references to calculate the time delay were the output end of the time delay and the initial reflective surface of the U-bench. Measurements were taken with the micrometer of the optical time delay set at the 20 mm mark. This micrometer position was taken as position 0 mm and used as a reference. Additional measurements were taken 5 mm

forward (positive) and backward (negative) from the reference point in increments of 1 mm. The data is shown below in Figure 4.8.

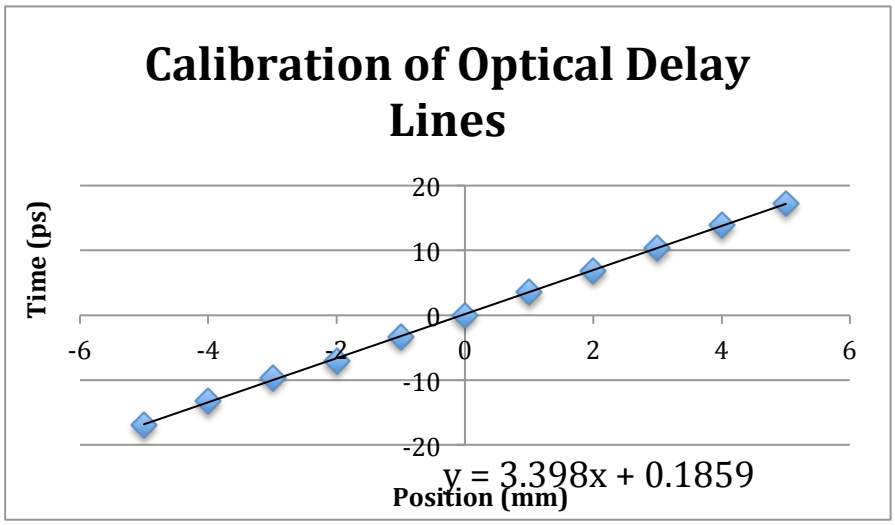

Figure 4.8: The calibration of the optical delay line using the Luna OBR 400.

The slope of the graph shows that 1mm of translation on the micrometer resulted in a time delay of approximately 3.4 ps, which is within 2% of the data sheet value of 3.33 ps. This value was consistent with experimental setup. However, for experimental purposes, the time delay for 1 mm was taken as 3.4 ps instead of the data sheet value of 3.33 ps. In addition, the OBR plots reflected power versus time delay or optical path length; therefore, this tool was also used to test the performance of the 1 x 4 splitter, which was made up of two 2 x 2 splitters spliced at 4 m in the setup, and each according to the data sheet

should have a 3 dB loss. Figure 4.9 shows a screenshot of the optical time delay setup and annotated with the physical surfaces encountered by each reflection spike. The group index, n_g, of the fiber was approximated to be 1.5 and has been converted from time-domain data into a optical path length axis in meters. With each reflection there was a loss of power. Each splitter showed a decrease in backscattered power levels in the fiber of 6 dB. However, this was increased by a factor of two because traveled twice through the splitter: transmission and reflection, so the loss was actually 3 dB. The experimental setup was working perfectly as designed and the optical delay lines were calibrated in order to achieve zero time delay for all four sources, hence maximum THz power along the optical axis.

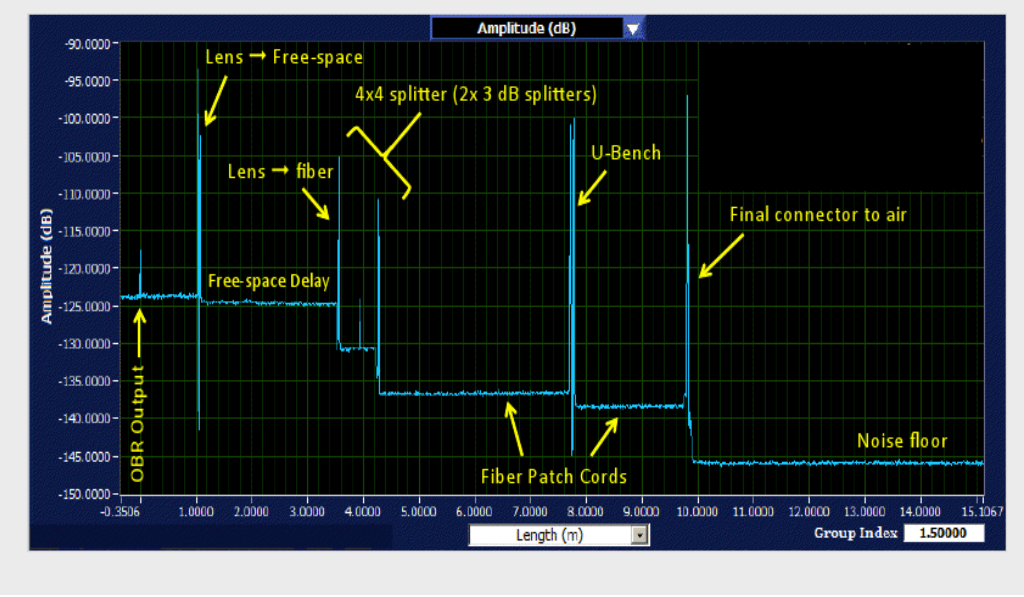

Figure 4.9: Screenshot of OBR showing reflection spikes: reflection power levels versus optical path length for experimental setup.

After the optical delay lines were calibrated, the packaged photoconductive switch linear array was packaged in the 77 K cryostat. The optical chopper in a U-bench provided a reference signal for the lock-in amplifier. A 1 x 4 splitter was used to split the laser power into the optical delays lines, which were connected to the photoconductive switch linear array through the fiber array. The array was mounted on the copper cold finger of the cryostat and the Golay cell, which was placed outside the cryostat, was used to measure the THz power. Figure 4.10 shows the experimental setup of the packaged photoconductive array.

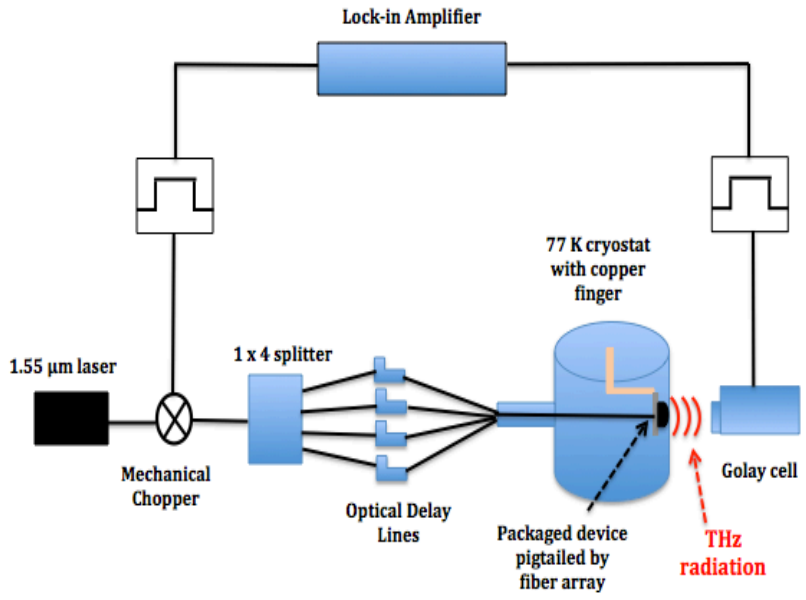

Figure 4.10: Experimental setup of packaged photoconductive switch linear array.

4.4. Summary

In order to make phased array technology more compact, researchers have implemented the use of MMIC, HEMT, and other alternative options. However, most of these options include work done with GaAs and an operational frequency up to 300 GHz (0.3 THz). This chapter addressed fabricating linear arrays of 2 and 4 photoconductive switches using InGaAs on InP substrate. The antenna was redesigned in order to accommodate pigtailing the fiber to the photoconductive gap of each antenna; an anvil was introduced in the gap for alignment purposes. The newly designed antenna had a frequency range from 7 GHz to 609 GHz. The linear array of photoconductive switches were packaged with the fiber array and mounted in a 77 K cryostat. The cryostat was hermetically sealed to ensure obtaining the desired temperature and pressure for experimental purposes. The ambient side of the experiment included the fiber array being connected to four optical delay lines to control the arrival of the 1.55 μm mode-locked laser pulses to each source. The optical delay lines were calibrated and the zero path length difference found using the Luna OBR 4400. The experimental setup was described in detail and experiments were done in order to test the performance of the linear array.

4.5. References

1. L. Brown, "Airborne radar: Its beginnings in World War II," IEEE Aerospace and Electronic Systems Magazine, Vol. 19, p. 3-8 (2004).

2. K. Takeuchi, "Fundamental Characteristics of a Slot-Coupled Microstrip Antenna using High Permittivity Feed Substrate," 22nd European Microwave Conference Digest p. 769-774 (1992).

3. L. Roy, "A 30 GHz, HEMT, Active Antenna Structure in MMIC Technology," 22nd European Microwave Conference Digest p. 236-241 (1992).

4. G. M. Rebeiz, P. D. Kasilingam, Y. Guo, P. A. Stimson, D. B. Rutledge, "Monolithic millimeter-wave two-dimensional horn imaging arrays," IEEE Transactions on Antennas and Propagation, v 38, n 9, p 1473-1482, (1990).

5. D. Sanchez-Hernandez, S. Lucyszyn, I. D. Robertson, "A Study of Integrated Antennas for THz Circuits," Center for Telecommunications Research, (1995).

6. E.R Brown, A.W.M. Lee, B.S. Navi, and J.E. Bjarnason, "Charaterization of a planar self-complementary square-spiral antenna in the THz region," Microwave and Optical Technology Letters, Vol. 48, p. 524-529 (2006).

5. THz Beam Steering

5.1. Beam Steering Theory

The radiation pattern of an antenna generally refers to the directional dependence of the strength of the electromagnetic waves emanating from the antenna. Typical radiation patterns contain what are called lobes that are local extemums in the angular dependence of the electric field. The main lobe of the antenna radiation pattern is the lobe that contains the maximum power while the adjacent lobes that have weaker power levels and are called side lobes. Beam steering is concerned primarily with changing the direction of the main lobe of the radiation pattern. This can be achieved by using a linear array of antennas. The concept of beam steering derives from the constructive and destructive interferences of electromagnetic radiation. When the electromagnetic energies of two or more closely spaced radiating sources (antennas) arrive at a point in space at the same time in a target plane, the radiation patterns overlap which results in and increase in the resulting electromagnetic energy. This is referred to as constructive interference. When each of the electromagnetic energies of the radiating sources arrives at a target plane at a specific change in time apart, (Δt), the electromagnetic energies may cancel each other (if the delay corresponds to the

appropriate phase) and results in what is known as a null point or zero energy. This is referred to as destructive interference. Manipulating the relative phases of the electromagnetic waves emitted by arrayed antennas gives the capability to achieve constructive interference in a desired direction. In essence, it gives us the ability to steer the radiated beam in a desired direction.

Consider a time harmonic signal, s(t), represented by the expression below:

$$s(t) = A\cos(\omega t) = A\Re\left\{e^{j\omega t}\right\} \tag{5.1}$$

The angular frequency, ω, is related to the frequency, f, through ω = 2πf, A is the amplitude of the signal s (t), and ℜ denotes the real part of the complex exponential. The signal, s(t) is periodic, which means the signal at a value t_0 will be repeated after a period at the time $t_0 + n(1/f)$, where n is an integer. We know that a plane wave is a disturbance in both space and time; therefore, a good representation for a plane wave is shown below:

$$s'(t) = A'\cos(\omega t \pm \frac{2\pi}{\lambda} l) = A'\Re * e^{j(\omega t \pm \frac{2\pi}{\lambda} l)} = A'\Re * e^{j(\omega t \pm kl)} \tag{5.2}$$

The distance along the propagation path is represented by *l* and k is known as the wave number (2π/λ). The phase of signal s' (t) is given by ϕ' = ωt ± k*l*. The direction of a THz beam can be controlled by changing

the phase over the elements of a linear array of antennas. Changing the phase gives the capability of changing how the waves interfere with each other. In 2008, Maki and Otani demonstrated THz beam steering by producing a phase relationship between the difference frequency generation of pump lasers and the THz radiation [1]. THz radiation was emanated from a strip-line photoconductive antenna excited by the difference frequencies of pump lasers. The phase shift was created by tilting one of the incident pump beams, which was then used to control the wavefront of the THz beam. This resulted in a steering range up to 29 degrees and tuning capability from 0.3 THz to 1.7 Thz. In 2010, Bauerschmidt and Preu demonstrated THz beam steering using n-i-p n-i-p superlattice photomixers. These photomixers produced a power of 1μW at 1 THz and was tunable over a frequency range of 0.1 - 2.5 THz [2].

For the purpose of this thesis, beam steering was performed in the time domain instead of the commonly practiced frequency (phase) domain. It was accomplished using fiber time delay lines, which controlled the THz radiation wavefront by changing the point of constructive interference at the target plane. Consider a linear array of antennas of N elements equally spaced a distance of *d*. The time delay of source *i* results in a phase delay of $\Delta\phi=\omega_{THz}\,\Delta t_i$. The wavefront of the

THz radiation makes an angle, θ, relative to the array normal as shown in Figure 5.1 [3].

In the time domain, a mode-locked laser has a waveform envelope of $\mathrm{csch}(t)^2$, which means it will constructively interfere with itself given synchronous alignment [4]. We also know that the THz pulses are coherent (time locked) with the laser pulse. Therefore, constructive interference will occur by synchronizing the THz pulses.

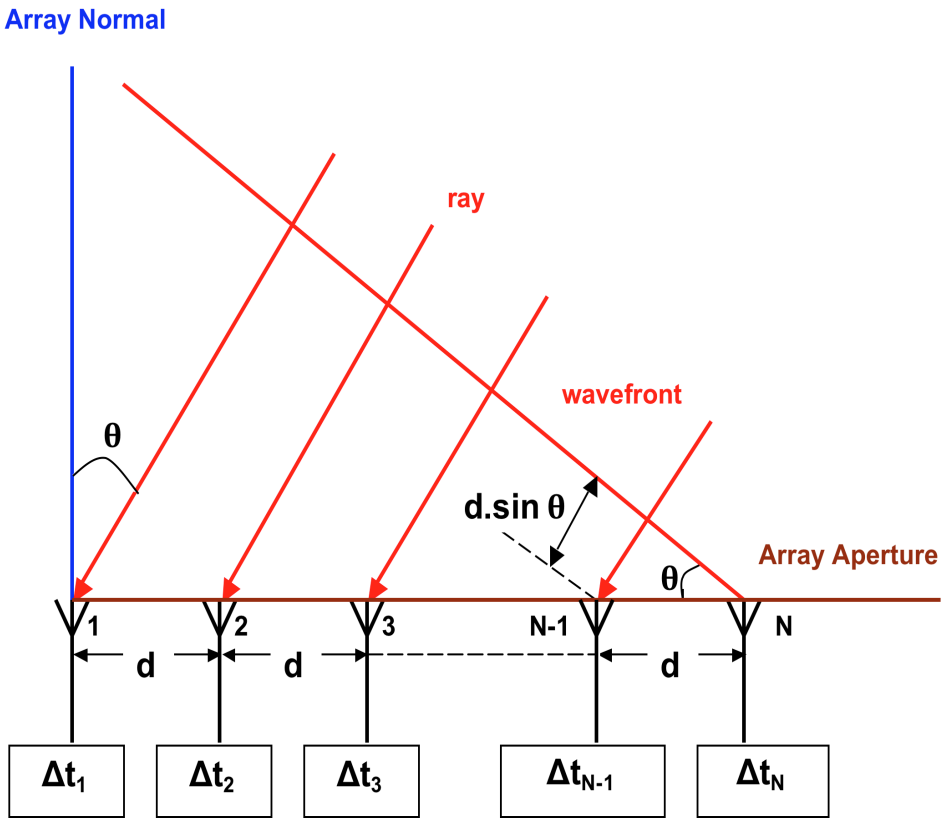

Figure 5.1: A linear array of N elements, equally spaced a distance d apart along a straight line, where a plane wave is incident under the angle θ with respect to the array normal. The delay times are adjusted with fiber delay stages.

Using goniometrics, the path length, $\Delta(\theta)$, of each device can be represented by the following

$$\Delta(\theta) = (N - i) * d \sin(\theta) \qquad \text{i = 0,1,2.....(N-1)} \tag{5.3}$$

Therefore, the time delay between devices is as follows

$$\Delta t_i = \frac{\Delta}{c} = \frac{(N - i) * d \sin(\theta)}{c} \qquad \text{i = 0,1,2....(N-1), c is speed of light} \tag{5.4}$$

In order to get a theoretical simulation of beam steering, the THz pulse was modeled using the following function [5].

$$f_i(t,\theta) = A_i * \sec h(a * t) \cos(b * t) * \sqrt{D(\theta)} \quad \text{for i = 1,2....N} \tag{5.5}$$

A_i is the field amplitude transmitted by the i^{th} antenna and is normalized to 1 for simplicity. *a* and *b* are the inverse duration of the pulse $(0.5 \text{ ps})^{-1}$ and the center of the power spectrum ($\omega = 2\pi * 300$ GHz) respectively. $D(\theta)$ is the directivity of the antenna, which was modeled as a Gaussian [6]. Figure 5.2 shows the modeled THz pulse.

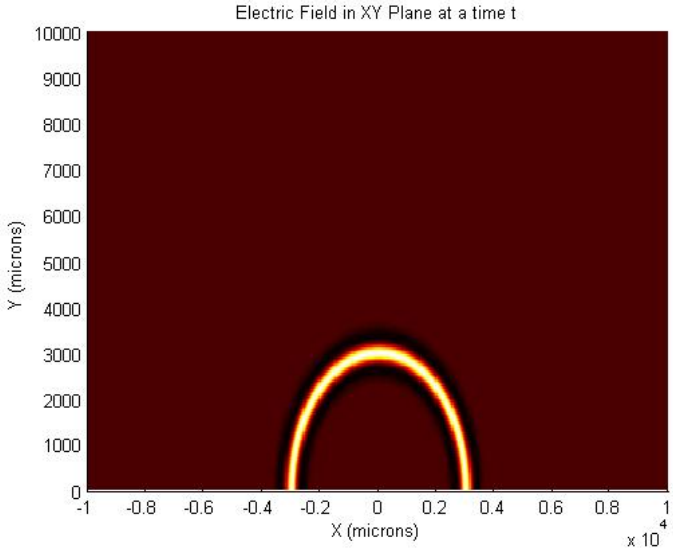

Figure 5.2 Modeled THz pulse.

Theoretical simulations of linear array systems of both 2 and 4 sources were performed for several time steps. Selected frames of the resulting movie of the beam propagation are shown in Figure 5.3 - Figure 5.5. The linear array was designed for a frequency of 600 GHz. The center-to-center spacing between sources was chosen to be 500 μm, which is the corresponding wavelength for 600 GHz. Simulations were performed in the far field region using the Fraunhofer diffraction approximation of $(2w^2/\lambda)$, where w is the width of the linear array. In the far field, the power of the radiation decreases as the square of the distance from the source, the absorption of the radiation by the detector has no effect on the source, and the shape of the radiation pattern is independent of distance.

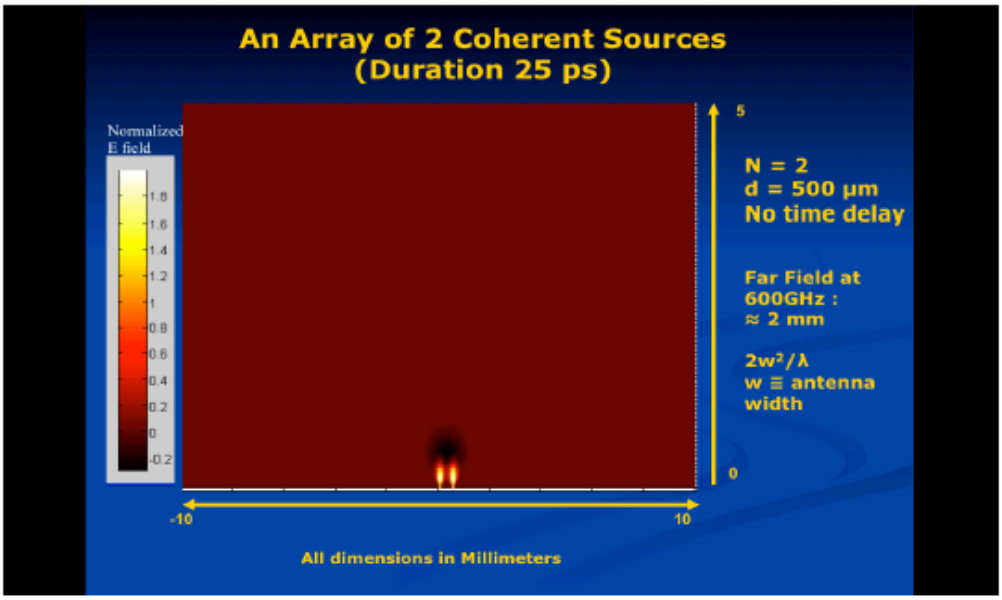

(a). Movie still frame of THz pulses from 2 coherent sources.

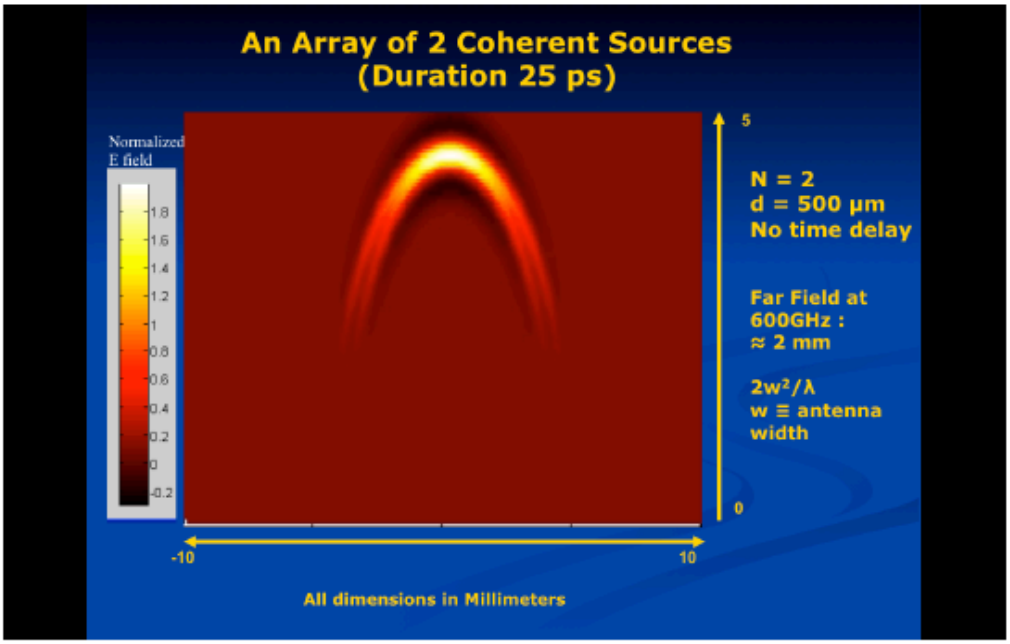

(b). Movie still frame of THz pulses from 2 coherent sources after 16 ps.

Figure 5.3 : Movie still frames of THz pulse from 2 sources. THz radiation is perpendicular to the axis of the linear array.

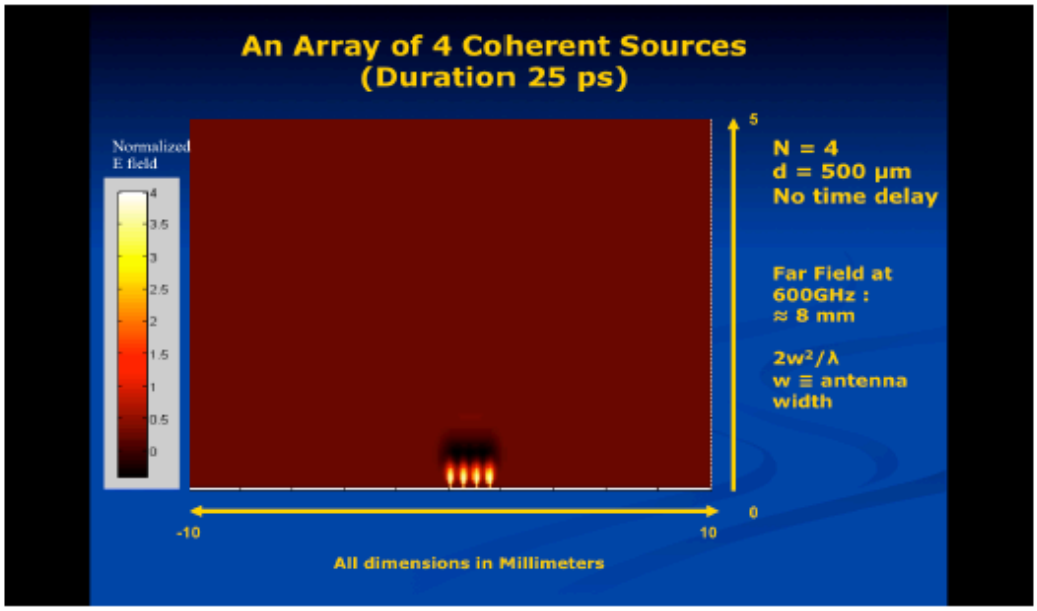

(a). Movie frame of THz pulses from 4 coherent sources.

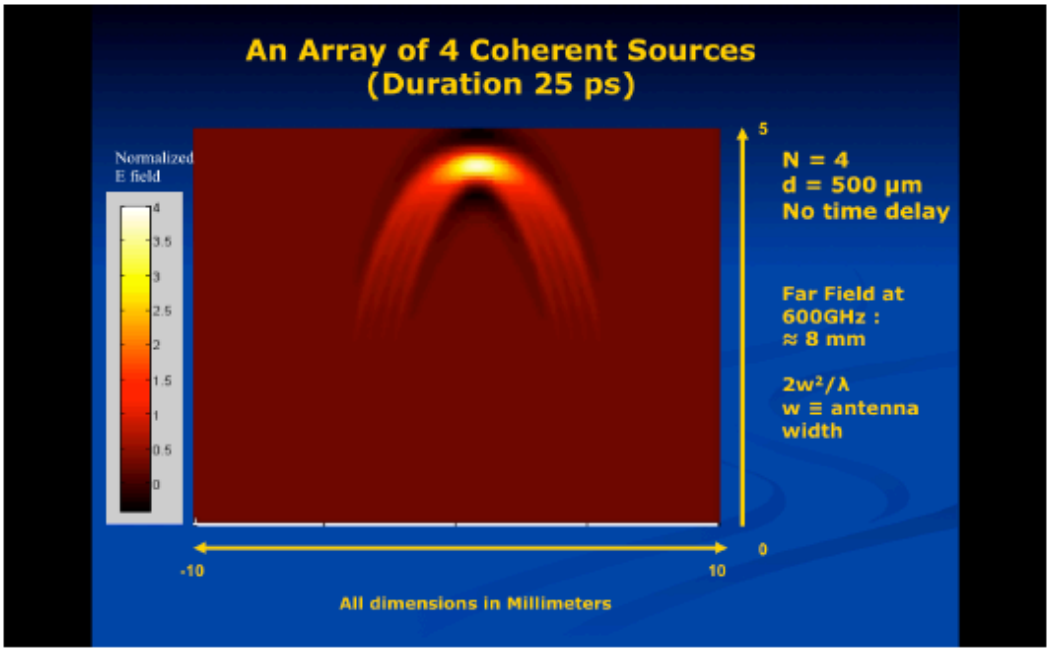

(b). Movie still frame of THz pulses from 4 coherent sources after 16 ps.

Figure 5.4 : Movie still frames of THz pulse from 2 sources. THz radiation is perpendicular to the axis of the linear array.

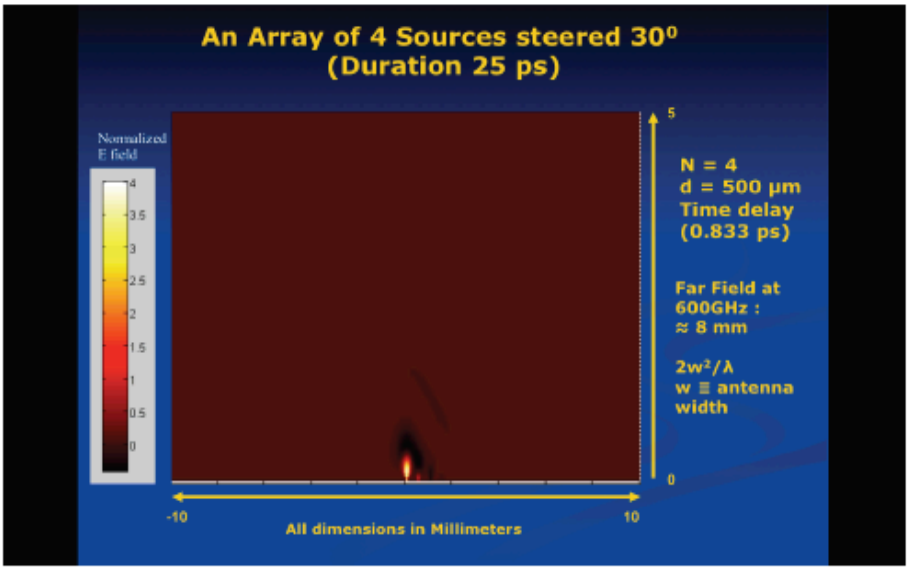

(a). Movie still frames of THz pulses from 4 sources with a time delay of 0.833 ps between sources. Beam steered 30 degrees to the normal.

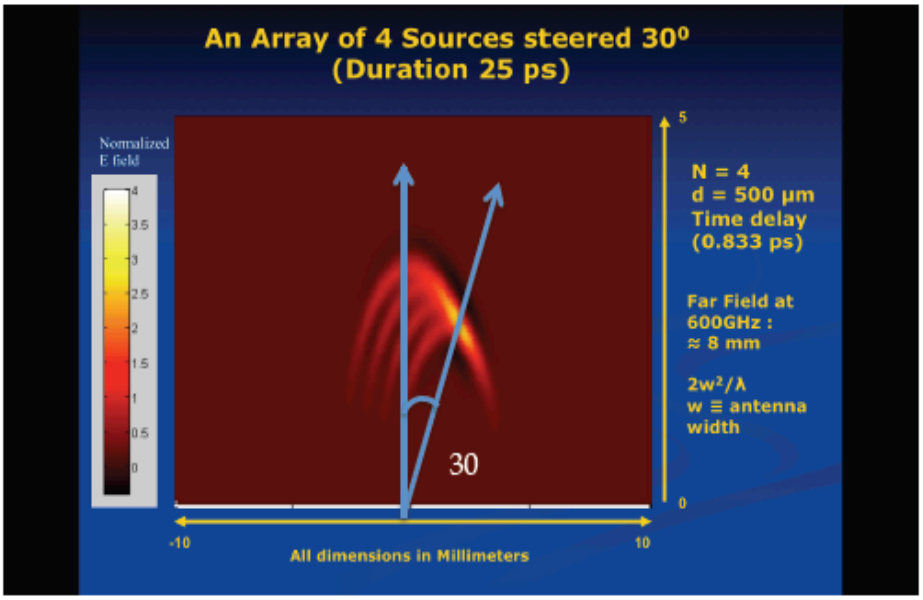

(b). Movie still frames of THz pulses from 4 sources with a time delay of 0.833 ps between sources after time 8 ps. Beam steered 30 degrees to the normal.

Figure 5.5 : Movie still frames of THz pulse from 4 sources steered at angle 30^0 to the normal. THz radiation is perpendicular to the axis of the linear array.

In Figure 5.3, the still frames show the propagation of THz pulses from 2 coherent sources. In Figure 5.4, the still frames show the propagation of THz pulses from 4 coherent sources. In Figure 5.5, the still frames show the propagation of THz pulses from 4 sources with a time delay of 0.833 ps of the pulses between each source that results in the steering of the beam to an angle of 30 degrees to the normal. The plane of the linear array is along the horizontal axis and the THz power propagates perpendicular to the array plane as expected.

One of the advantages of implementing a linear array system is that it combines the power from each source and thus increases the total transmitted power. To successfully design the architecture of a linear array system, the separation between sources was chosen to be λ, where λ is the wavelength of free space. This was done in order to minimize the effects of side lobes or only having one maximum within the scanning range [3]. Equation 5.6 below shows the constraint that applies to the distance between sources to minimize side lobes within scanning range – $\theta_{max} \leq \theta \leq \theta_{max}$.

$$\frac{d}{\lambda} \leq \frac{1}{\left|\sin(\theta_{max})\right|} \tag{5.6}$$

Therefore, for the scanning range between $-\pi/2 \leq \theta \leq \pi/2$, the above equation reduces to $d \leq \lambda$.

If the THz electric field arrives at a target plane equidistant from all the sources then constructive interference will occur. In the far field, the intensity of the main lobe increases as N^2 (N is the number of sources) compared to that of a single source. The total radiated power, however, which is integrated over all angles, will just increase by a factor of N. In addition, the beam width is inversely proportional to aperture size [3]. By increasing the distance between antenna elements of the linear array, the beam will get narrower and consequently steering of the beam gets more accurate at the cost of more intense side lobes. Knowing this fact and due to design performance for 600 GHz, the distance between antenna elements was chosen to be λ (500 μm) for 600 GHz. Figure 5.6 shows the simulated power comparison for the cases shown in Figure 5.3 - Figure 5.5 for a single source, 2 sources, 4 sources and 4 sources steered at 30 degrees respectively. Figure 5.6(a) shows the power of a single antenna element and was used as a reference for the simulated directivities of the 2 and 4 element array. Figure 5.6(b) shows the power of a 2-element array with a 6 dB gain, which is in accordance to a gain of N^2. Figure 5.6(c) shows the power of a 4-element array with a 12 dB gain, which is in accordance to a gain of N^2. Figure 5.6(d) shows the power of a 4-element array steered at 30 degrees with a 9.6 dB gain. This decrease in gain compared to that of the coherent 4-element array system

is discussed in the beam steering section of this thesis. The beam width does get narrower and more accurate with the increase in the number of elements and the increase in aperture size.

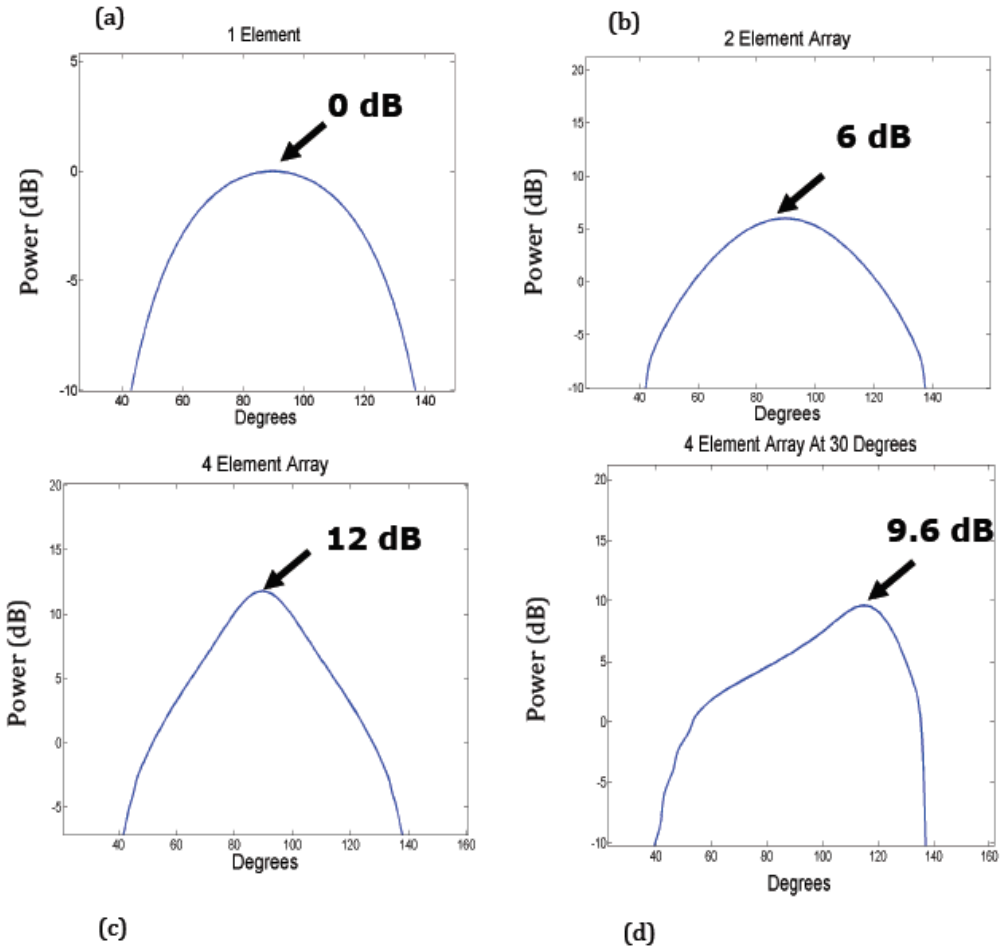

Figure 5.6: Power comparison of a single element, 2 and 4-element array, and a 4-element array steered at 30 degrees.

5.2. Experimental Results

The THz output power was experimentally characterized in two ways. In the first method measurements were taken without any bandpass

filter, while the second set of measurements was acquired using a VDI bandpass filter designed for 600 GHz transmission. The unfiltered output THz power of a single source, 2 and 4-source linear array versus the bias voltage are plotted in Figure 5.7 - Figure 5.9The device was biased over a voltage range from 0 to 24 V. Device breakdown occurred at 25 V. The output THz power obtained form the single source measurement was taken to predict the theoretical performance of the 2 and 4-source linear array, since the THz power has a quadratic dependence on bias voltage. See equation 5.7.

$$P_{THz} = \frac{1}{2} I_{AC}^2 * R_{AC} \rightarrow I_{AC} \propto V_{AC} \tag{5.7}$$

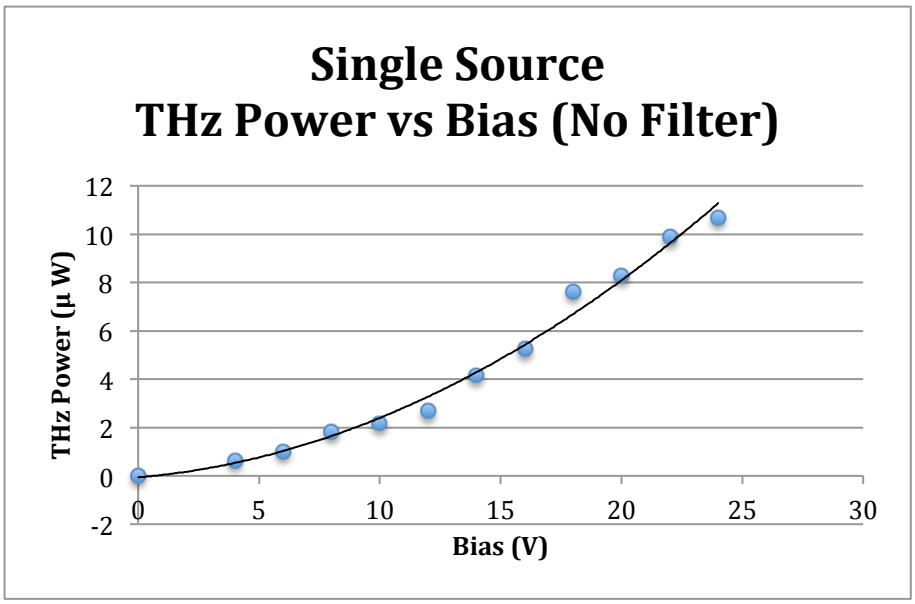

Figure 5.7: THz Power of a single source vs bias voltage with no filter, fitted with a quadratic polynomial.

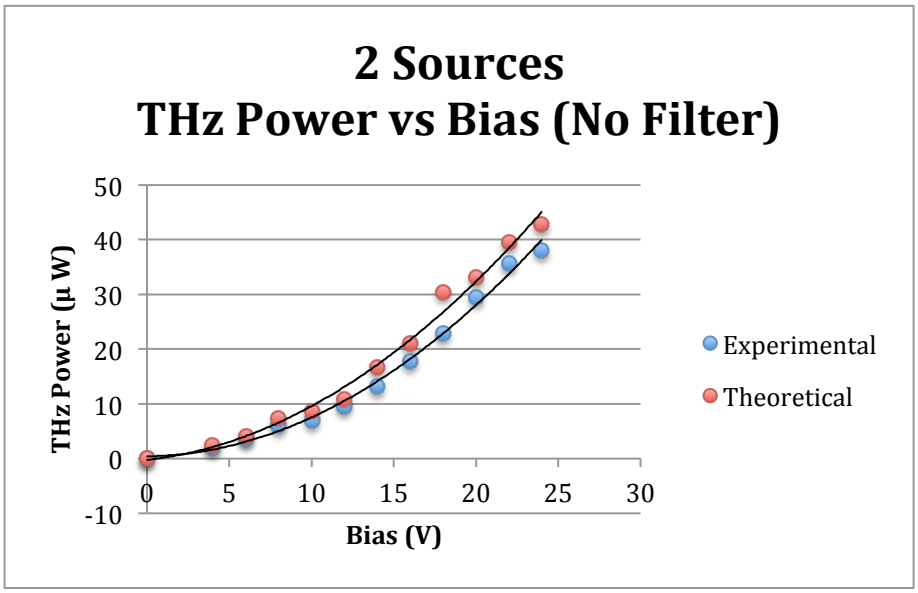

Figure 5.8: THz Power of a 2-source linear array vs bias voltage with no filter, fitted with a quadratic polynomial.

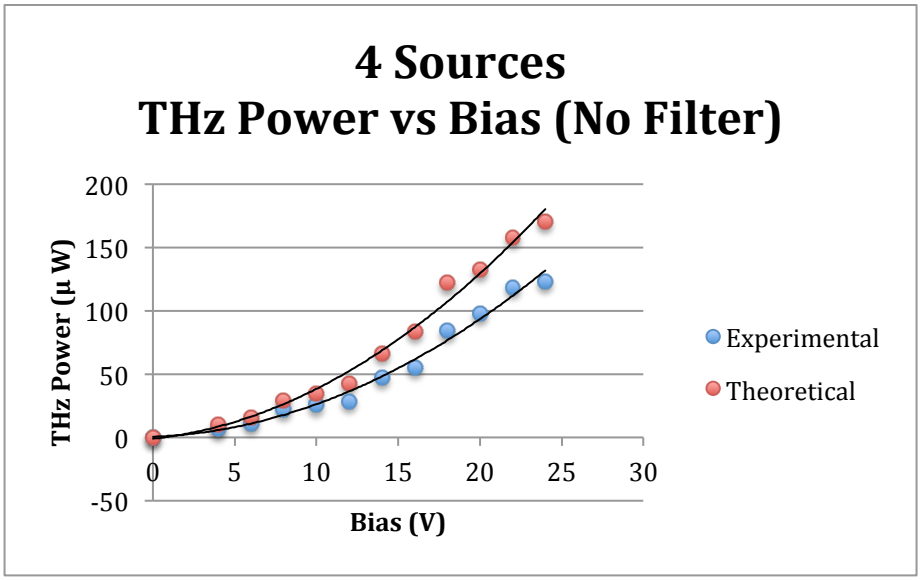

Figure 5.9: THz Power of a 4-source linear array vs bias voltage with no filter, fitted with a quadratic polynomial.

The highest powers recorded for a single source, 2 and 4-source linear array were obtained at a bias voltage of 24 V and the measurements with a maximum peak power of 10.38 μW, 38.12 μW and 123.4 μW respectively. The THz power measured by the Golay cell is actually the peak intensity of the radiation pattern, whereas, the total radiated power would be that of the intensity integrated over all angles. The peak intensity measured by the Golay cell will have a quadratic dependence on bias voltage as shown in Equation 5.7. The experimental THz power does show a near quadratic dependence as can be seen based on the quadratic polynomial fit.

Spectral discrimination of the THz power was achieved by placing a custom quasi-optical VDI bandpass mesh filter between the array and the Golay cell. The THz filter was designed as frequency-selective surfaces in copper, and had a center frequency of 600 GHz. Figure 5.10 shows the actual transmission of the VDI bandpass filters, in which filter number 4 was the 600 GHz filter. However, the transmission of the filter was measured and it had a center frequency of 537 GHz and a bandwidth of 128 GHz.

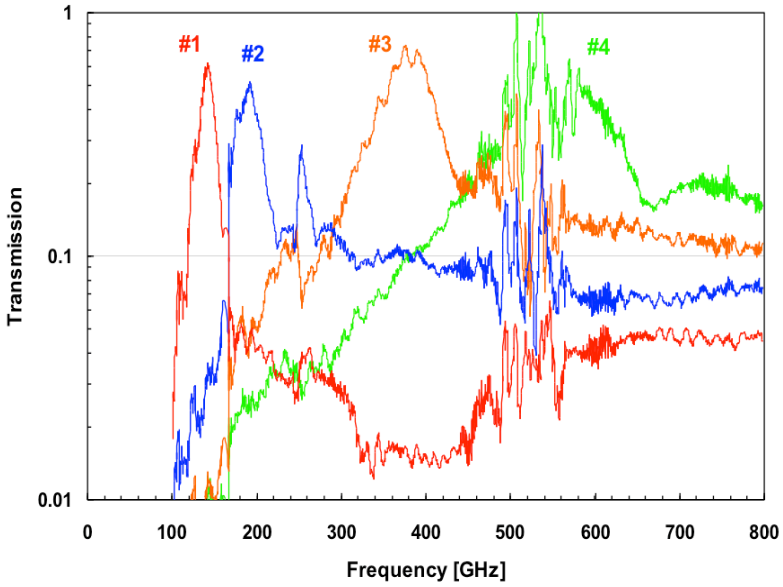

Figure 5.10: Transmission data of VDI bandpass filters. Recall Number 4 is the 600 GHz filter.

Figure 5.11- Figure 5.13 show the results of the THz power at 600 GHz versus bias voltage for a single source, 2 and 4-source linear array respectively. The highest powers recorded for a single source, 2 and 4-source linear array at 600 GHz were also obtained at a bias voltage of 24 V and the measurements were 4.75 μW, 16.15 μW and 40.45 μW respectively. As previously stated, device breakdown occurred at 25 V. The lower values at 600 GHz indicate pronounced emission at lower frequencies but the device is still efficient at 600 GHz to provide power

for THz applications. The experimental power at 600 GHz also shows a near quadratic dependency on bias voltage for the 2 and 4-source array.

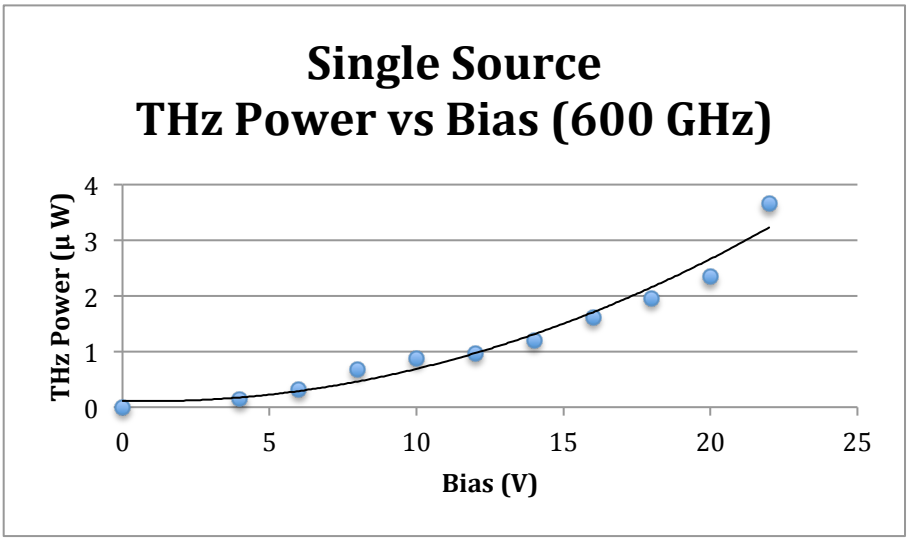

Figure 5.11: THz Power of a single source vs bias voltage with 600 GHz filter fitted with a quadratic polynomial.

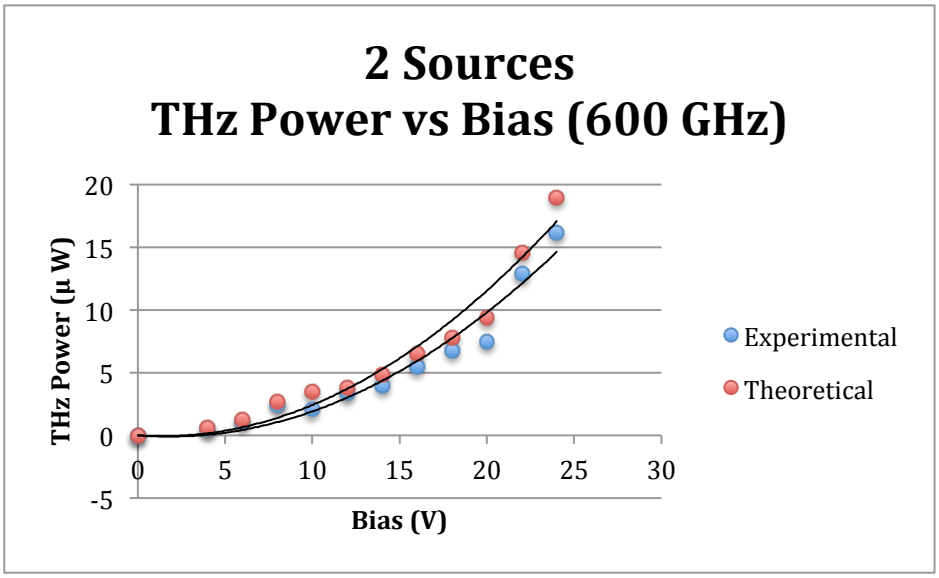

Figure 5.12: THz Power of a 2-source linear array vs bias voltage with 600 GHz filter fitted with a quadratic polynomial.

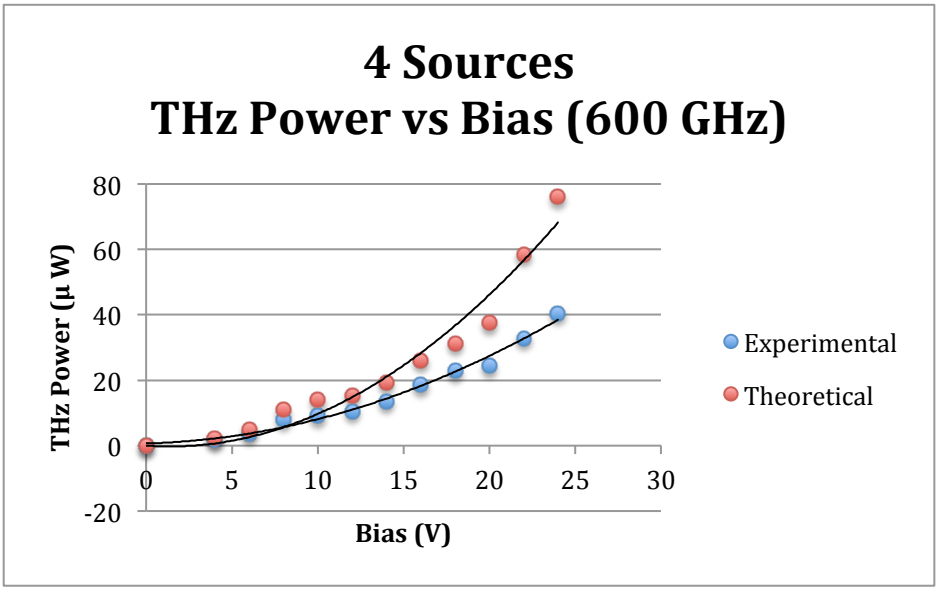

Figure 5.13: THz Power of a 4-source linear array vs bias voltage with 600 GHz filter fitted with a quadratic polynomial.

The THz power data was also plotted versus the number of sources, N, to show the N^2 dependency. Figure 5.14 shows the THz power versus number of sources for specific bias voltages with no filter present fitted with a quadratic polynomial. The THz power with no filter agrees well with theory [2] and does show a quadratic dependence on number of sources. Figure 5.15 shows the THz power versus number of sources for specific bias voltages at 600 GHz fitted with a quadratic polynomial. This data also corresponds well with the theoretical expectations as the THz power has a quadratic dependence on the number of sources.

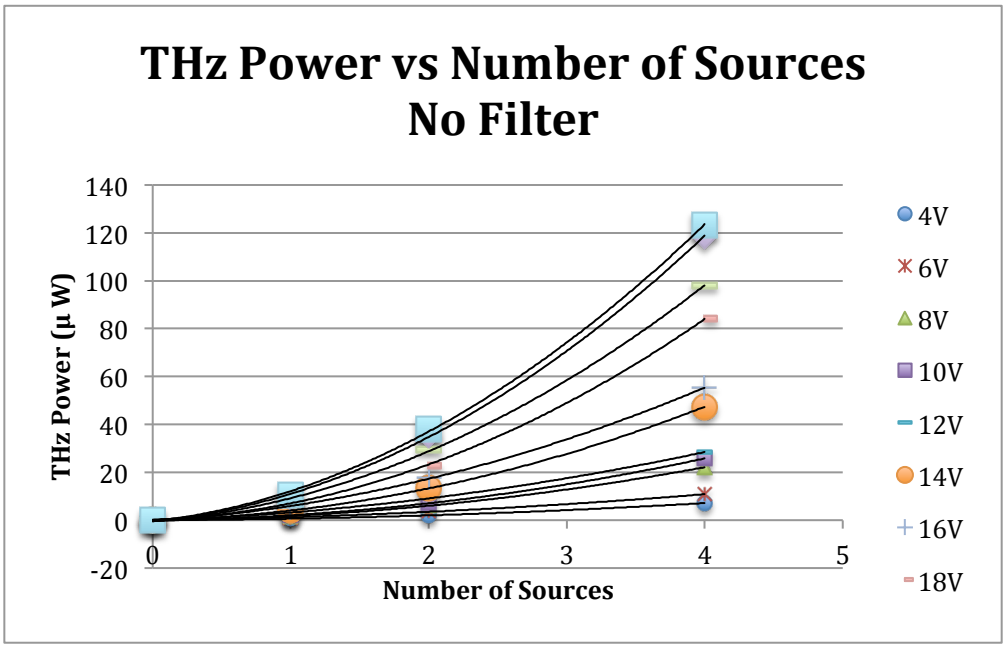

Figure 5.14: THz Power vs Number of Sources biased up to 24 V without any filter fitted with quadratic polynomial.

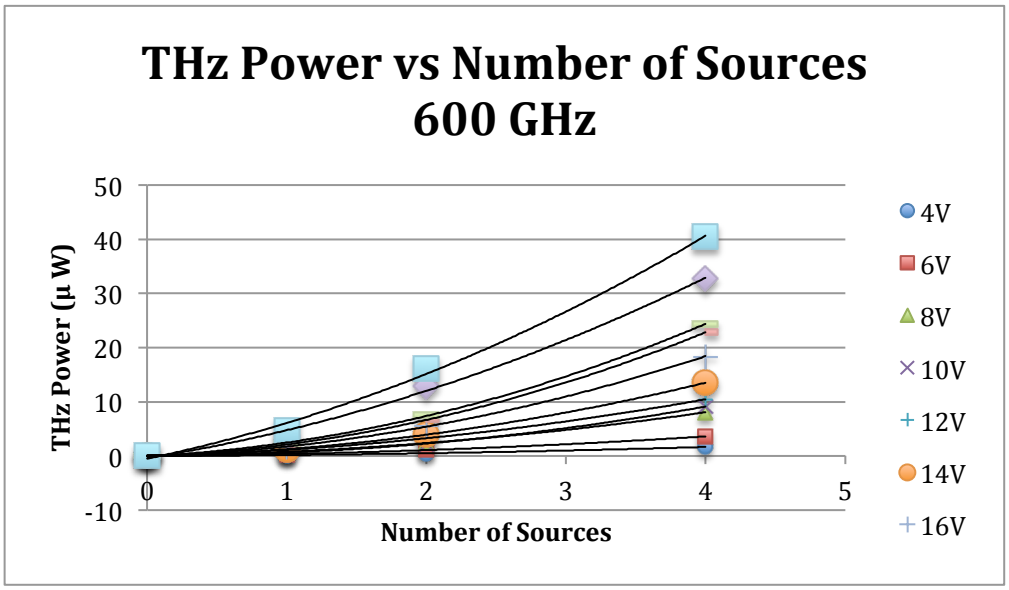

Figure 5.15: THz Power vs Number of Sources biased up to 24 V at 600 GHz fitted with quadratic polynomial.

An advantage of using interference of the array beam patterns is the reduction of the beam waist of the main lobe. This decrease in beam waist depends on the number of sources and the spacing between sources. An increase in the number of sources or spacing between sources will result in a narrower beam. This results in a tighter focus when steering the beam. The beam width of electromagnetic radiation can be determined by using the approximation of a Gaussian beam [6], whose transverse and electric field and intensity distributions are well approximated by the Gaussian function below.

$$f(x) = Ae^{\frac{-(x-x_o)^2}{2w^2}} \tag{5.8}$$

The Gaussian function is used to determine the full width half max (FWHM), which is a parameter commonly used to determine the beam waist, w, of electromagnetic radiation.

For the purpose of this thesis, the x direction was designated to be parallel to the linear array axis, the y direction was designated to be perpendicular to the linear array axis and z is the direction that goes away from the linear array. Figure 5.16 shows the beam profile in the x direction for a single source, 2 and 4-source linear array.

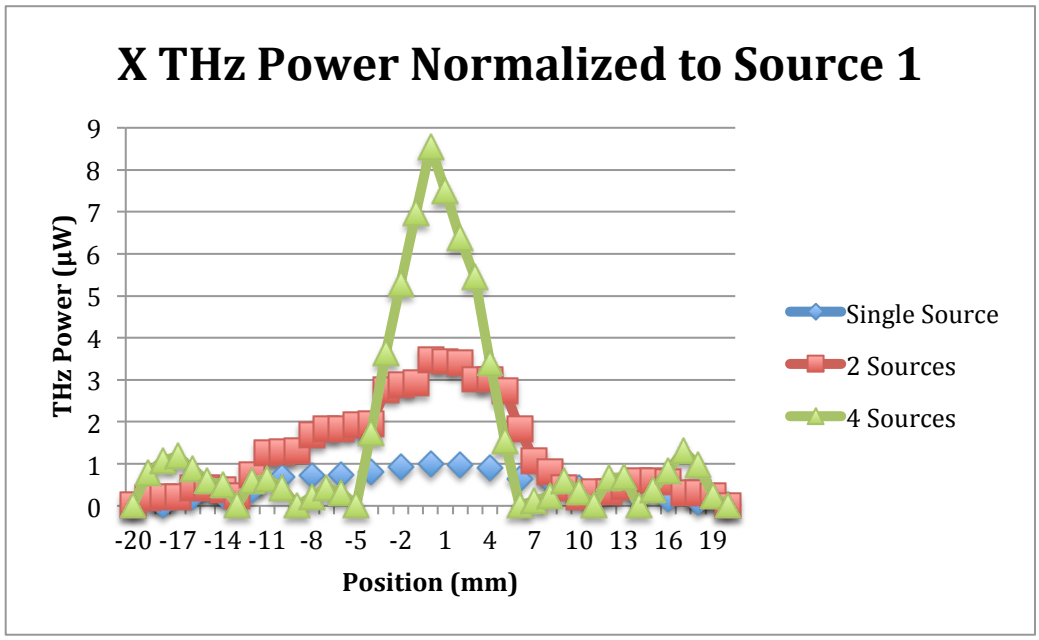

Figure 5.16: Beam profile in the x-direction of single source, 2 and 4-source linear array.

The Gaussian function was used to approximate the beam widths (FWHM) for the single source, 2 and 4-source linear array. For the single source, 2 and 4-source linear array, the beam widths were calculated to be 20.16 mm, 13.24 mm and 5.96 mm respectively. For the 2-source linear array, the beam width reduced to roughly half of that of the single source beam, and the 4-source linear array reduced to roughly a fourth of that of the single source, which is in accordance to theory. The Gaussian fits are shown in Figure 5.17.

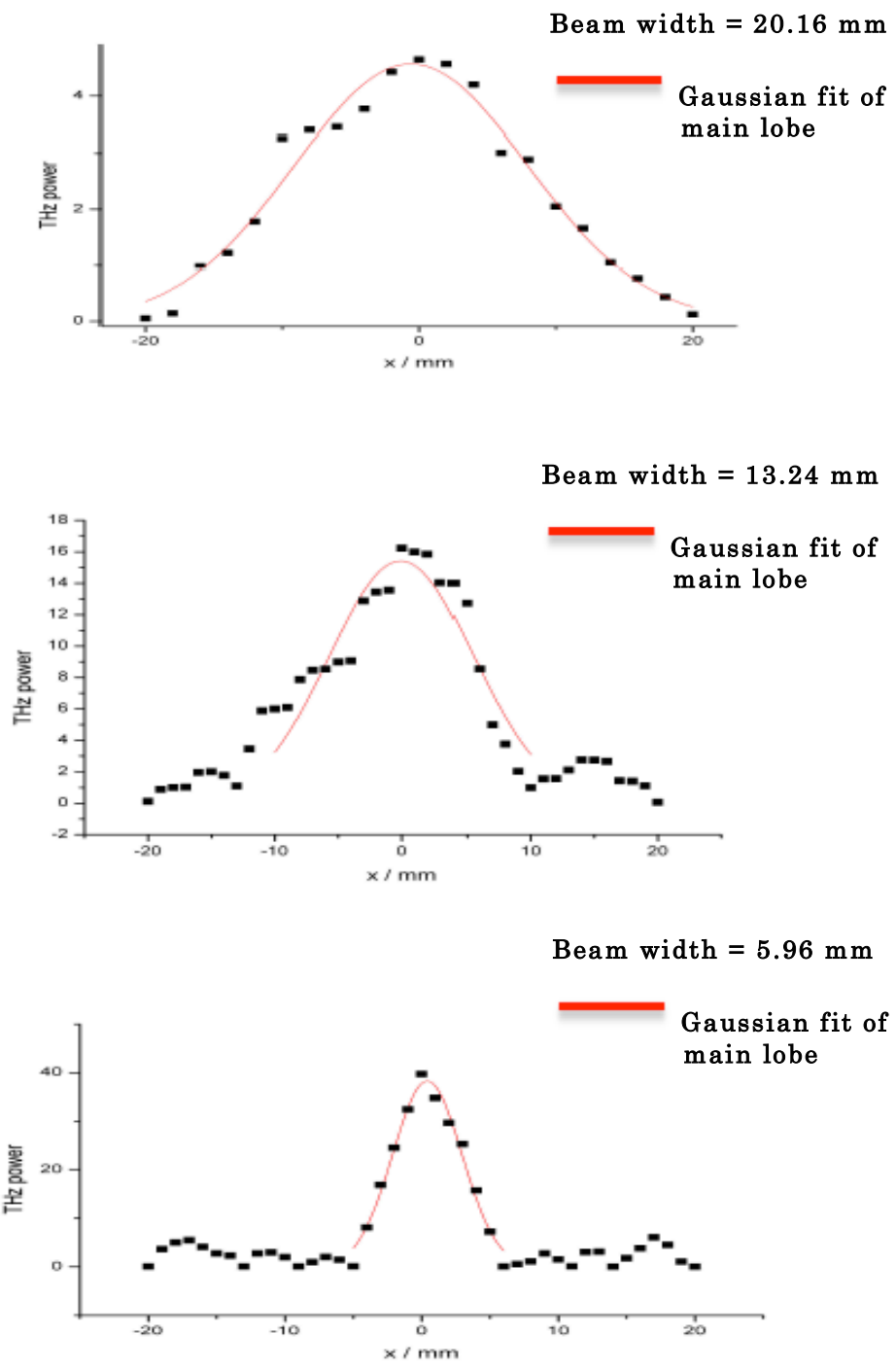

Figure 5.17: Gaussian fits of the main lobe for (a) single source, (b) 2-source, (c) and 4-source.

Beam profiles were also taken of each source of the linear array to see how they spatially relate to each other. This was to ensure that they were spatially able to constructively interfere and meet any requirements for beam steering. Figure 5.18 shows the spatial distribution of each source of the linear array. This spatial distribution is close enough to control the combined interference radiation pattern to steer the beam in a desired direction in a target plane.

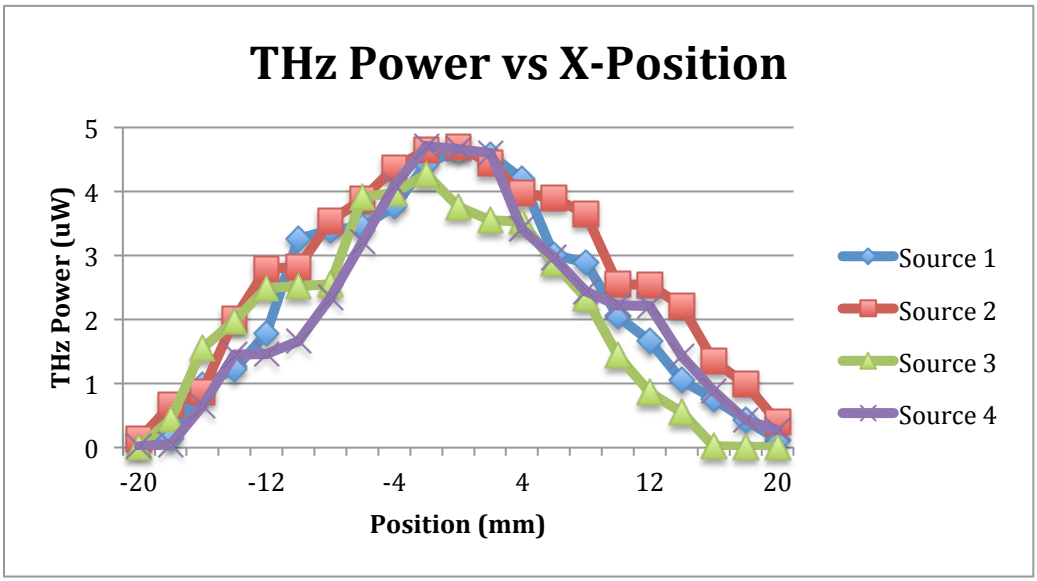

Figure 5.18: Beam profile showing spatial distribution in the x-direction of each source.

In order to get a 2D beam profile of the linear array, scans were done in both the x and y direction and then plotted. The pulses from the 1.55 μm mode-locked laser were controlled through a time delay system to make

them coherent on arrival to the linear array. This resulted in maximum constructive interference, hence maximum power. The beam profiles and contour plots of the single source, 2 and 4-source are shown in Figure 5.19 - Figure 5.21.

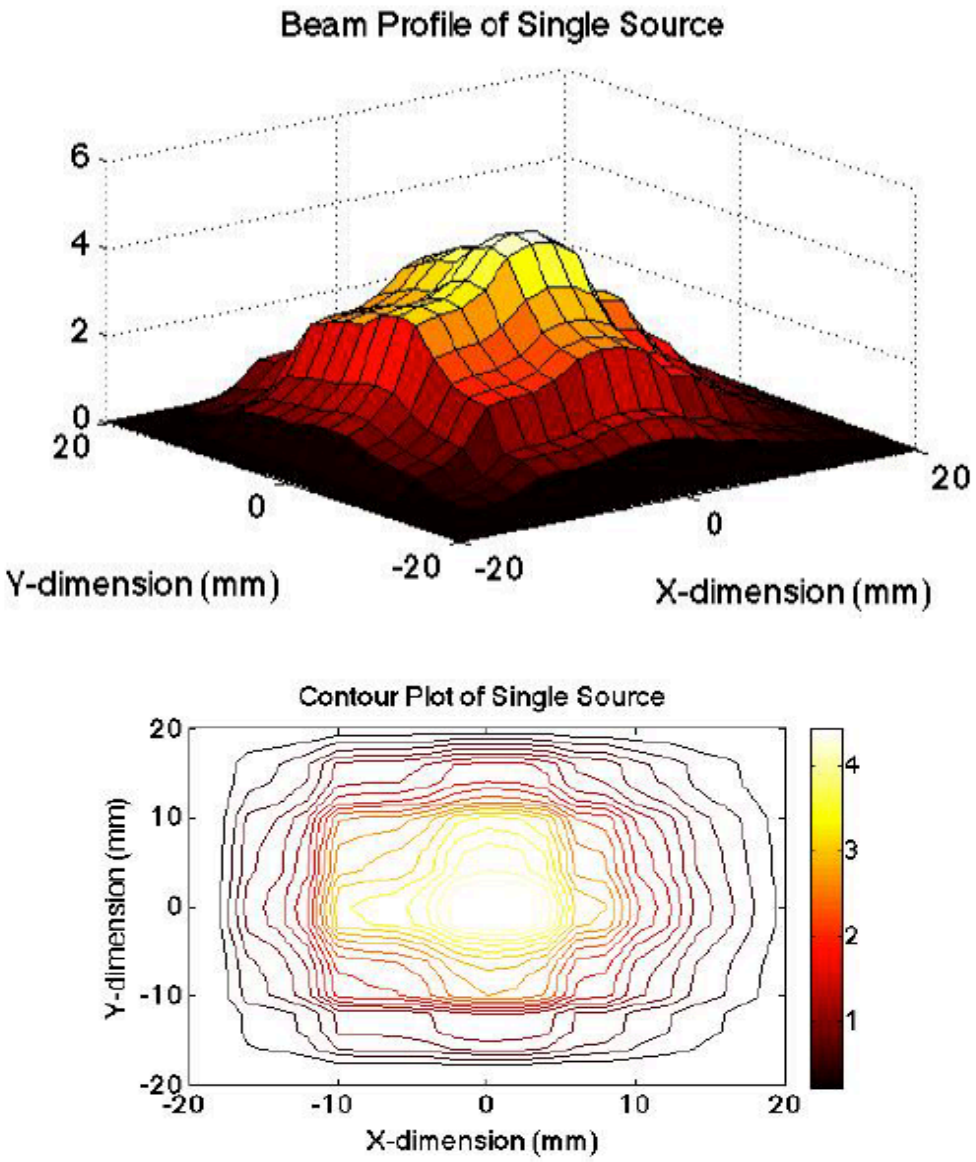

Figure 5.19: Beam profile and contour plot of a single source.

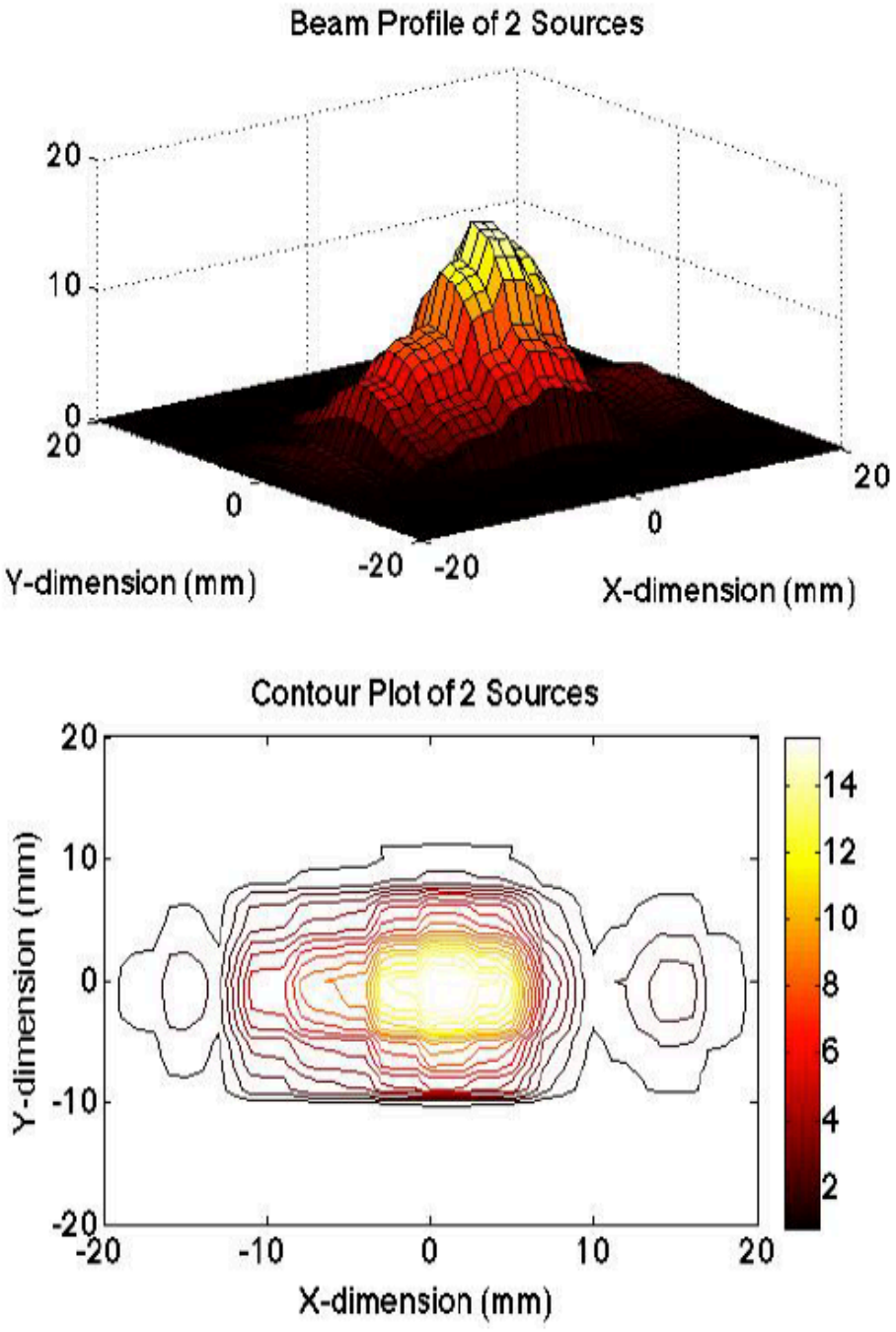

Figure 5.20: Beam profile and contour plot of a 2-source linear array.

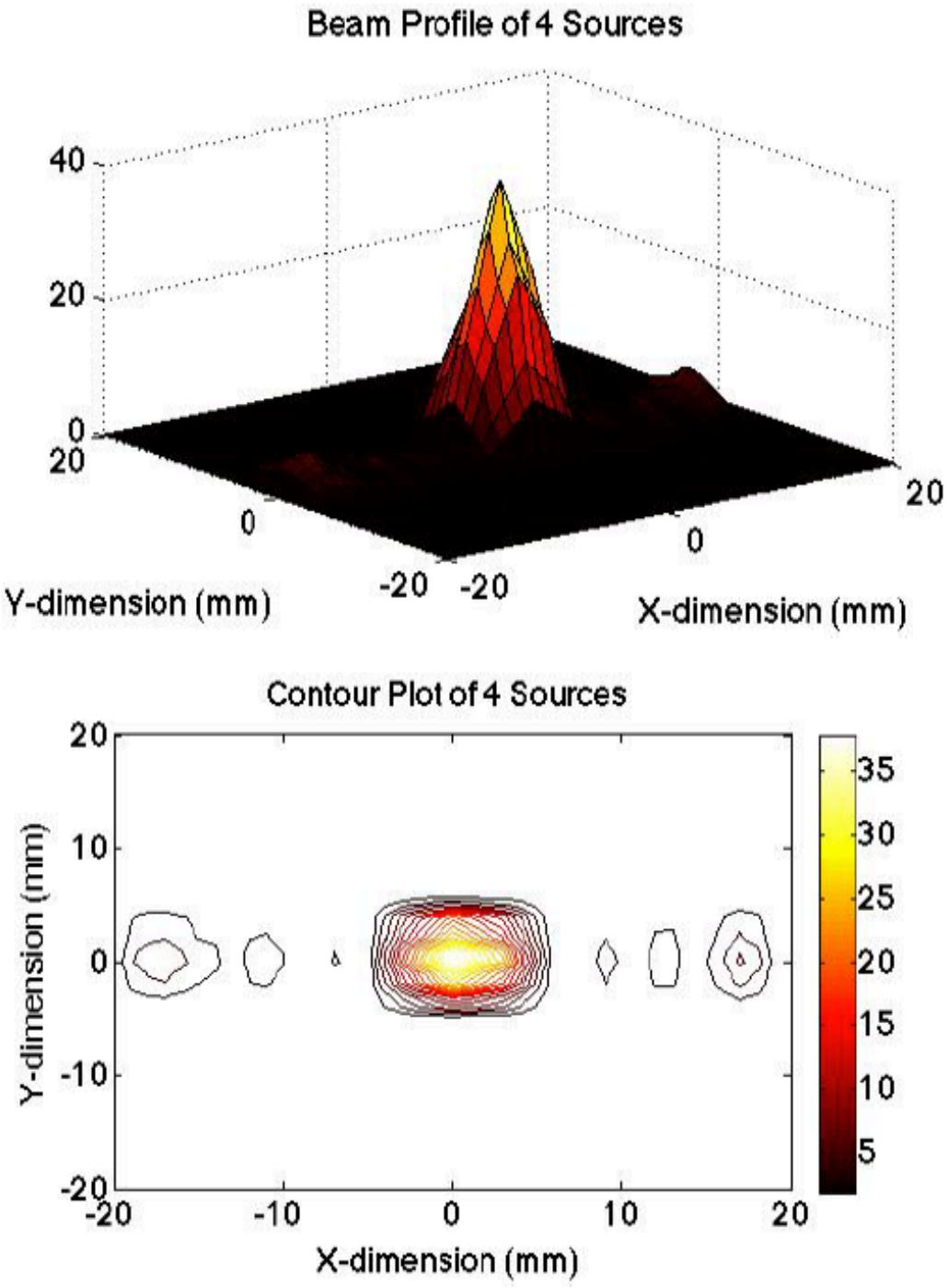

Figure 5.21: Beam profile and contour plot of a 4-source linear array.

The beam steering method used in this experiment was to establish a relationship between the phases of the THz radiation pulses and the optical delay lines. Hence, the phases of the THz radiation were controlled by the time of travel to each source by the laser pulses. The signal is increased by constructive interference in the main direction and the beam sharpness is improved by mainly destructive interference. A delay of 43.6 μm, 86.8 μm, and 129.41 μm were required in order to produce beam steering angles, θ, of 5^0, 10^0, and 15^0 respectively (see equation 5.3) at 600 GHz. This corresponds to a time delay between sources of 0.145 ps, 0.289 ps, and 0.431 ps respectively (see equation 5.4). Therefore, the optical delay line was adjusted with the required number of turns to achieve this time delay between sources. Figure 5.22 shows the beam profiles in the x-direction for a 2-source linear array being steered at 5^0, 10^0, and 15^0. ΔX represents the shift in the beam profile compared to that of 2 coherent sources. ΔX had values of 1 mm, 2 mm and 3.5 mm for beam steering of 5^0, 10^0, and 15^0 respectively. The experiment was repeated exciting 4 sources instead of 2 sources. Figure 5.23 shows the beam profiles in the x-direction for a 4-source linear array being steered at 5^0, 10^0, and 15^0. ΔX had values of 1.25 mm, 2.5 mm and 4 mm for beam steering of 5^0, 10^0, and 15^0 respectively.

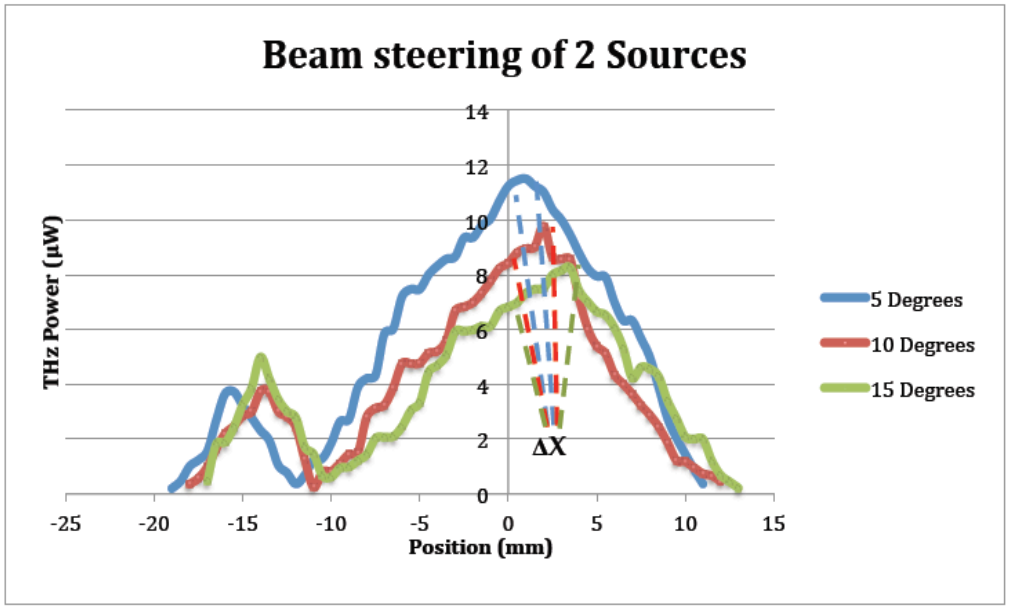

Figure 5.22: Beam profile of 2-sources in the x-direction (parallel to array plane) steered 5, 10, and 15 degrees to the normal.

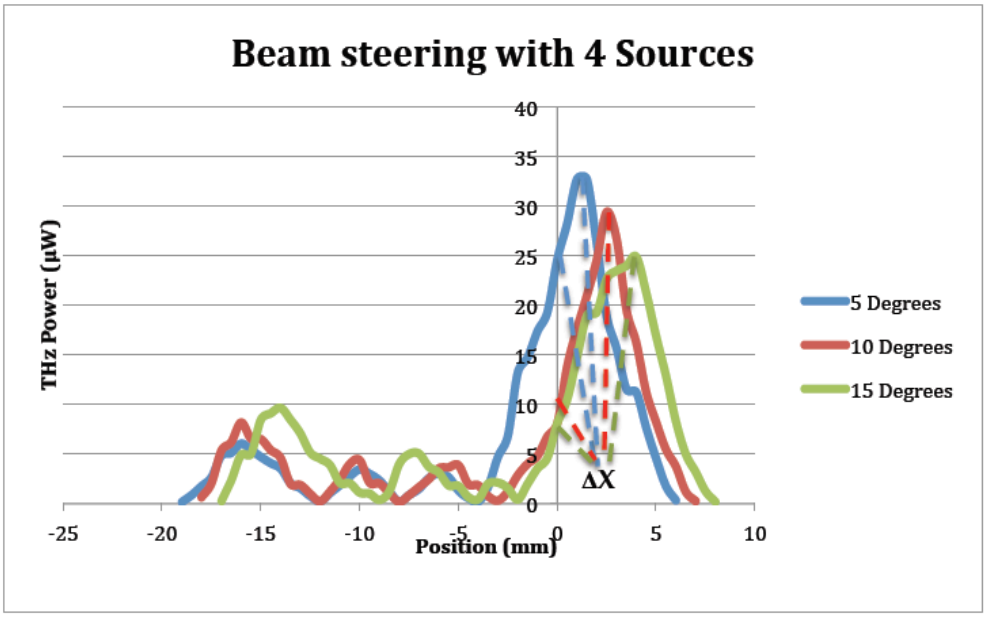

Figure 5.23: Beam profile of 4-sources in the x-direction (parallel to array plane) steered 5, 10, and 15 degrees to the normal.

Varying the time delay of the laser pulses resulted in the THz radiation being steered in a desired direction. Recall from Chapter 3 that the device is packaged on a silicon hyperhemispherical lens, which has a setback of a distance t = 0.76 mm, including the thickness of the device substrate. This setback of the lens resulted in the refraction of the THz rays at the Si/air interface. Therefore, the detector (Golay cell) detected the refracted THz rays. Figure 5.24 shows how the path of the steered THz ray traverses from generation from the device to the Golay cell. R is the radius of the silicon lens (5 mm), D is the distance from the device to the detector (25 mm), ΔX is the distance the Golay cell travels to detect the main lobe from the perpendicular (coherent sources) direction to the steered direction, ß is the refracted angle, and θ is the actual angle of beam steering. The refracted angle, ß, is given in equation 5.9 below.

$$\beta = \tan^{-1}\left(\frac{\Delta X}{D}\right) \tag{5.9}$$

Diffraction effects were ignored since R was much greater than the wavelength at 600 GHz (500 μm). In order to calculate the actual angle of beam steering, a relationship between ß and θ was determined.

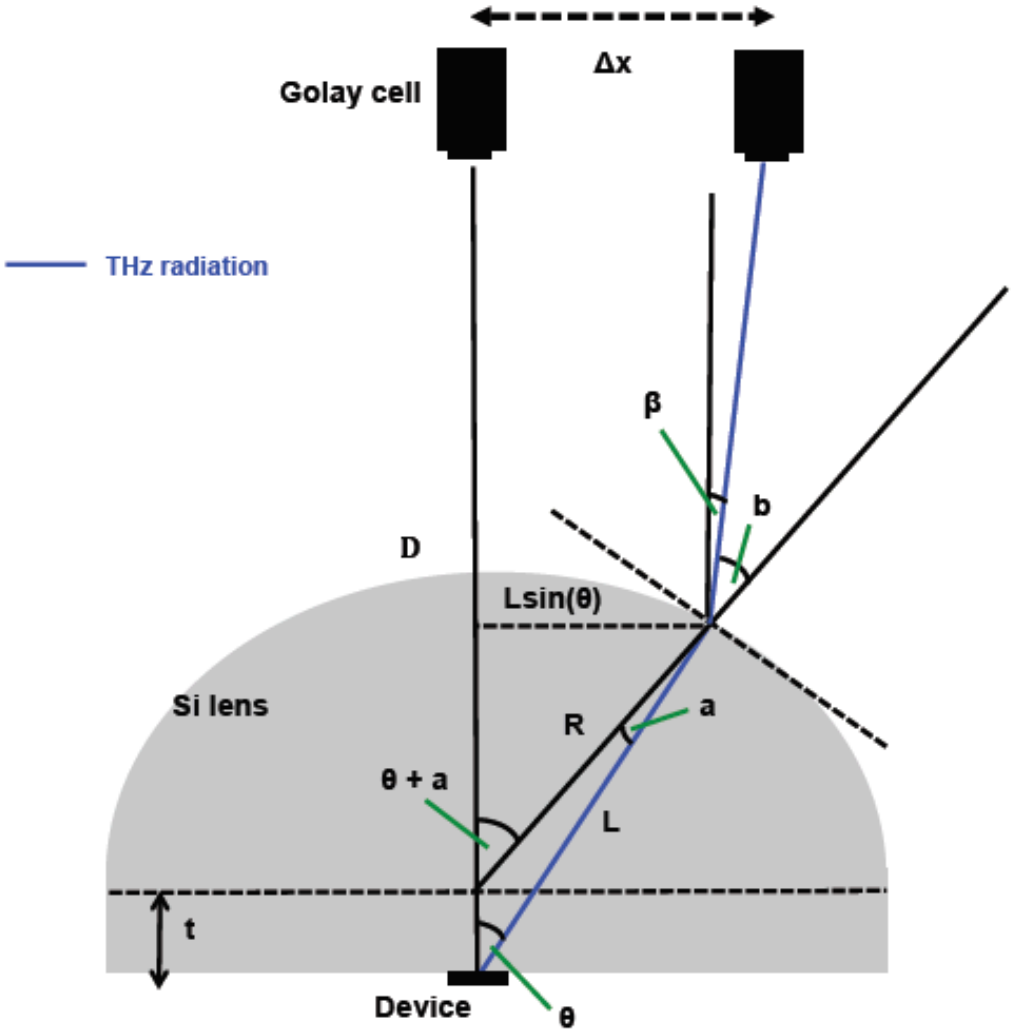

Figure 5.24: The path the steered THz ray traverses from generation from the device to the Golay cell.

The relationship between β (refracted angle) and θ (beam steering angle) is given in equation 5.10. The angle θ was calculated from the measured angles, β, for the beam steering of 5^0, 10^0, and 15^0, for both the

2-source and 4-source linear arrays. Figure 5.25 shows the graph of β versus θ up to 20^0.

$$\textit{From Figure 5.24; } \theta + a = \beta + b = \sin^{-1}\left(\frac{L\sin(\theta)}{R}\right)$$

$$a = \sin^{-1}\left(\frac{L\sin(\theta)}{R}\right) - \theta$$

$$\beta = \theta + a - b$$

$$n_{Si}\sin(a) = n_{air}\sin(b) \qquad \textit{Snell's Law}$$

$$b = \sin^{-1}(n_{Si}\sin(a))$$

$$t^2 + L^2 - 2tL\cos(\theta) = R^2$$

$$L = \frac{2t\cos(\theta) \pm \sqrt{(2t\cos(\theta))^2 - 4(t^2 - R^2)}}{2}$$
$$= t\cos(\theta) + \sqrt{(2t\cos(\theta))^2 - 4(t^2 - R^2)}$$

$$\textit{Recall } \beta = \theta + a - b = \theta + \sin^{-1}\left(\frac{L\sin(\theta)}{R}\right) - \theta - \sin^{-1}(n_{Si}\sin(a))$$

$$\beta(\theta) = \sin^{-1}\left(\frac{L\sin(\theta)}{R}\right) - \sin^{-1}\left(n_{Si}\sin\left(\sin^{-1}\left(\frac{L\sin(\theta)}{R}\right) - \theta\right)\right) \qquad (5.10)$$

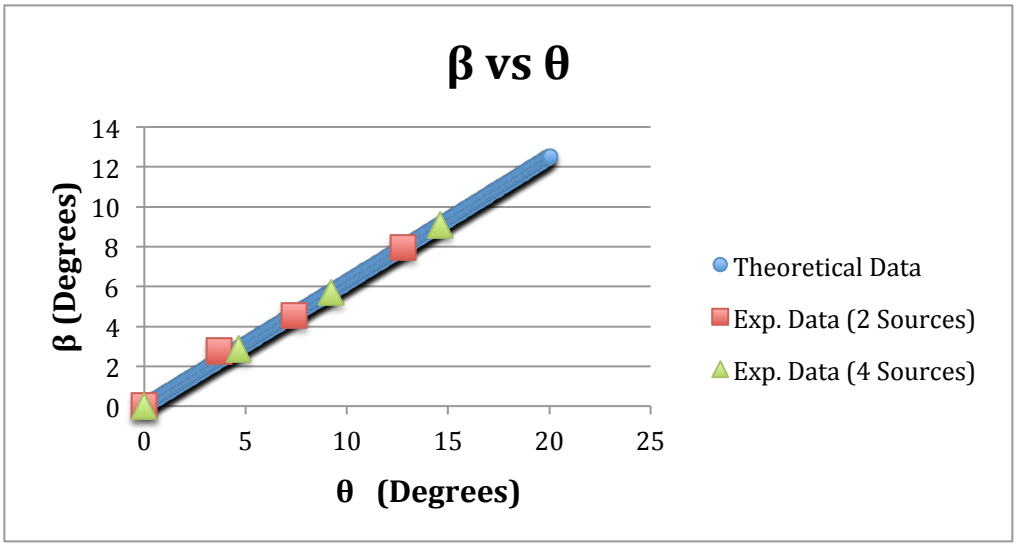

Figure 5.25: Comparing β versus θ for both theoretical and experimental data.

The experimental results of both β and θ for a 2-source linear array and how it compares to theory is shown in Figure 5.26. Figure 5.27 does the same for a 4-source linear array.

Δx (mm)	1	2	3.5
β (Degrees)	2.75	4.57	7.97
Calculated θ (Degrees)	3.72	7.39	12.77
Theoretical θ (Degrees)	5	10	15

Figure 5.26: Comparing the experimental results of both β and θ for a 2-source linear array.

Δx (mm)	1.25	2.5	4
ß (Degrees)	2.87	5.7	9.09
Calculated θ (Degrees)	4.64	9.22	14.6
Theoretical θ (Degrees)	5	10	15

Figure 5.27: Comparing the experimental results of both ß and θ for a 4-source linear array.

The experimental data for beam steering angle, θ, corresponded well with the values extrapolated from the refracted angle, β. For the 2-source linear array steered 5^0, 10^0, and 15^0, the experimental values were within 6% (3.72^0), 26% (7.39^0), and 15% (12.77^0) of the expected values. For the 4-source linear array steered 5^0, 10^0, and 15^0, the experimental values were within 4% (4.64^0), 8% (9.22^0), and 3% (14.6^0) of the expected values. There was a decrease in the power in the main lobe and an increase in the power in the side lobes as the beam was steered to greater angles. This was due to the fact that the source position remained fixed and steering occurs by defining the relative phases between the elements. The amplitudes of the orders of constructive interference follow that of the individual sources. For larger emission angles, the amplitude of the zeroth order reduces while the first order gains more power while it approaches the direction of maximum emission at 0^0.

5.3. Summary

THz pulse was modeled and simulated to investigate the effect of time delay on the constructive and destructive interference of the pulses. Experiments were done to measure how the THz power varied with bias voltage at 77 K with and without a 600 GHz filter. The power displayed a near quadratic dependence on voltage. Experiments were also done to measure how the THz power varied with the number of sources; this too also displayed a near quadratic dependence as expected from theory. The highest powers recorded for a single source, 2 and 4-source linear array were obtained at a bias voltage of 24 V and the measurements had an maximum peak power of 10.38 μW, 38.12 μW and 123.4 μW respectively. The corresponding values for THz power at 600 GHz were 4.75 μW, 16.15 μW and 40.45 μW respectively. The beam profiles showed that the beam width decreased with an increase in number of source, since it is inversely proportional to aperture size. Side lobes were detected and increased in power as the main lobe decreased in power when the THz beam was steered. This was due to the fact that during the beam steering of the 2 and 4-source linear array, the lobes follow that of a single source. In order to obtain the angle of beam steering, a relationship between the measured detected angle and the actual beam

steering angle was established. The beam steering angle had scanning capabilities of 12.77^0 and 14.6^0 for 2 and 4-source photoconductive switch array at 77 K.

5.4. References

1. K. Maki and C. Otani, "Terahertz beam steering and frequency tuning by using the spatial dispersion of ultrafast laser pulses," Optics Express, Vol. 16, No. 14, p. 10158-10169 (2008).

2. S. Bauerschmidt, S. Preu, S. Malzer, G.H. Dohler, L. J. Wang, H. Lu, and A.C. Gossard, "Continuous wave Terahertz emitter arrays for spectroscopy and imaging applications," Proc. of SPIE, Vol. 7671, p. 76710D-1-76710D11 (2010).

3. H. J. Visser, "Array and Phased Array Antenna Basics," Chapter 7, John Wiley and Sons, West Sussex, England (2005).

4. B. C. Barnett, L. Rahman, M. N. Islam, Y. C. Chen, P. Bhattacharya, W. Riha, K. V. Reddy, A. T. Howe, K. A. Stair, H. Iwamura, S. R. Friberg, and T. Mukai, "High-power erbium-doped fiber laser mode locked by a semiconductor saturable absorber," Optics Letters, Vol. 20, Issue 5, p. 471-473 (1995).

5. Z. Ma1, H. Ma1, C. Yang, and K. Feng, "Modeling of terahertz pulse generation from LT-GaAs ultrafast photoconductive switches," Journal of Systems Engineering and Electronics, Vol. 22, No.3, p. 373-380 (2011).

6. J. E. Bjarnason,a, T. L. J. Chan, A. W. M. Lee, E. R. Brown, D. C. Driscoll, M. Hanson, A. C. Gossard, and R. E. Muller, "ErAs:GaAs photomixer with two-decade tunability and 12 mW peak output power," Appl. Phys. Lett., Vol. 85, No. 18, p. 3983-3985 (2004).

7. R. J. Mailloux, "Phased Array Antenna Handbook," Chapter 1, Artech House, Norwood, MA. (1994).

8. M.Lax, W. H. Louisell, and W. B. Mcknight, "From Maxwell to paraxial wave optics," Physics Review A 11, 1365–1370 (1975).

6. Conclusion and Future Work

6.1. Summary

Epitaxial composite materials grown using MBE consisting of semimetallic ErAs nanoparticles embedded in an $In_{0.53}Ga_{0.47}As$ matrix lattice matched to InP substrate was used to fabricate a THz source. ErAs nanoparticles act as recombination sites, which resulted in subpicosecond lifetime. The electrical behavior of the material showed that the material had a high resistivity, 5.7×10^6 Ω-cm, and high breakdown voltage, 23 V, when the temperature was lowered to 77 K. This gave promise to create a linear array of photoconductive switches for an operational wavelength of 1.55 μm. A broadband self-complementary square spiral antenna was designed for frequencies up to 1.35 THz. Frequency selective filters were used to experimentally test the broadband nature of the THz source.

The motivation for this work was to engineer a device compatible with fiber technology (1.55 μm wavelength) that would generate THz power for applications including THz time-domain spectroscopy (TDS) and security imaging. Using fiber technology makes experimental setup more cost effective and more compact. The linear array of photoconductive switches fabricated on InGaAs material optically excited by 1.55 μm mode-locked

laser at a temperature of 77 K demonstrated a total THz power up to 123 μW without spectral discrimination and 40 μW with a 600 GHz frequency at a bandwidth of 128 GHz. Optical delay lines were used to control the arrival of the laser pulses to each source, which resulted in the capability to control constructive and destructive interference of the THz radiation from the linear array. The manipulation of interference pattern led to the beam being steered in a desired direction. For a 2-source linear array, a scan angle of 12.77 was demonstrated, and for a 4-source linear array, a scan angle of 14.6 was demonstrated.

6.2. Outlook

The photoconductive switch linear array in this dissertation was designed for frequencies up to 600 GHz. For future work, further improvements are possible for designing the antenna to be more broadband, which would improve the dynamic range of the device in applications of security imaging [1,2] and THz-TDS [3,4,5]. Recall from Chapter 2, equation 2.1, that the radiating dimensions of the antenna determine the bandwidth. Therefore, varying the size of the square unit cells can be used to obtain the desired frequency range but is limited by fabrication processes and chip size.

In addition, more than four sources can be used with different array configurations. Since the beam width is inversely proportional to aperture size, increasing the spacing between sources results in an improved beam focus, but at the expense of increasing the intensity of side lobes. An increase of the array elements will result in reduced lobe intensity.

Experiments in this dissertation were done with a 77 K cryostat, which was maintained using liquid nitrogen. Experiments were done at 77 K to prove the concept of having a THz source optically excited by a 1.55 μm mode-locked laser. However, experiments could have also successfully been done at 200 K, which is attainable by using a thermoelectric (TE) cooler. Recall from Figure 3.4 in chapter 3 that at 200 K, the breakdown voltage of the device was 13 V and the resistivity increased in order of magnitude. Also, in Figure 5.13 in chapter 5, the generated THz power at 13 V at 600 GHz was approximately 12 μW, sufficient for most applications. Therefore, performing a successful experiment at 200 K is quite feasible. For practical purposes, packaging and operation of the 1.55 μm THz photoconductive switch linear array should be less cumbersome and therefore more compact. The current setup is limited by the sizes of the cryostat, the optical delay lines and 1 x 4 splitter. In order to make this setup more compact, the cryostat can be

replaced with a TE cooler and the optical delay lines and splitter can be integrated on a single chip using optical waveguides. Implementing the optical delay line on a single chip has been made possible due to the groundbreaking work on integrated photonic delay (iPHoD) done by the Blumenthal's group at University of California, Santa Barbara. This research uses an optical component on a chip rather than fiber device. The research has shown the development and use of low loss waveguide, which have loss that is comparable to that of fiber 0.045 dB/m [6]. Each optical delay line has dimensions of 145 mm x 60 mm x 55 mm. There is an optical delay line for each source, which means the size of experimental setup scales with the number of sources. Each optical delay line can be replaced by a true time delay (TTD) chip [7] with dimensions of roughly 20 mm x 30 mm. The optical TTD is shown in Figure 6.1. The true time delay uses polymer waveguides and thermo-optic switches to achieve the desired time delay; the switches are used to determine the path of the pulse, which can be designed to obtain whatever the desired time delay. The waveguides were made of SiN core with SiO_2 cladding on Si substrate.

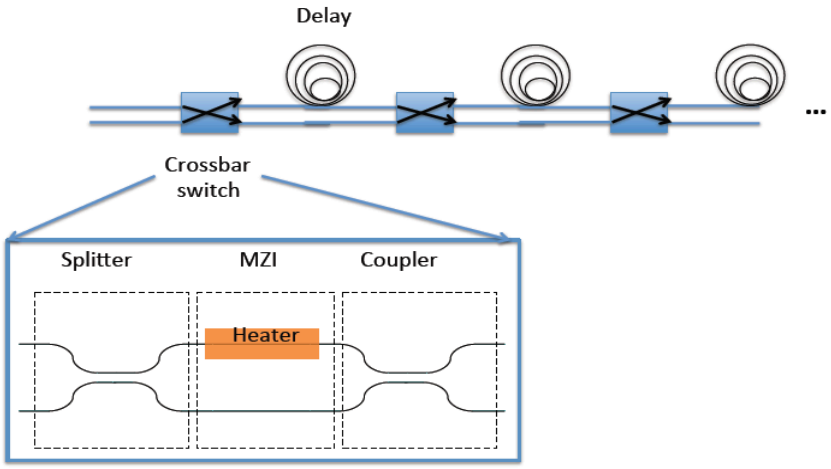

Figure 6.1: True time delay chip where the path of the pulse is determined by switches that are controlled by heat.

The 1 x 4 power splitter can also be replaced with multi-mode interference couplers (MMI) and packaged on the same chip as the TTD. Arrays of 1 x 2 MMIs that is 375.5 µm long and 15 µm wide with corner angled 67.7^0 [8] are capable of splitting the power from the 1.55 µm mode-locked laser. The cryostat can be replaced by a TE cooler with dimensions 18 mm x 18 mm with a delta max of 117 K. Therefore, the experimental setup will drastically decrease in size with these improvements. However, in packaging the device, the TE cooler has to be isolated from the thermo-optic switches to ensure experiment performs as

designed. The ultimate goal is to integrate most of the experimental setup on a single chip [9].

6.3. References

1. B. Ung, J. Balakrishman, B. Fischer, B.W.-H Ng, and D. Abbott, "Terahertz detection of substances for security related purposes," Proc. Of SPIE, Vol. 6414, p. 64141U-1 - 64141U-1 (2007).

2. A. G. Davies, A. D. Burnett, W. Fan, E. H. Linfield, and J. E. Cunningham, "Terahertz spectroscopy of explosive and drugs," Materials Today, Vol. 11, p. 18-26 (2008).

3. M. Walther, B. M. Fischer, and P. U. Jepsen, "Non covalent intermolecular forces in poly-crystalline and amorphous saccharides in the far infrared," Chem. Phys. Vol. 288, p. 261 – 268 (2003).

4. B. Fischer and D. Abbott, "T-ray spectroscopy of biomolecules," IRMMW-THz - Conf. Digest Jt. Int. Conf. Infrared Millimetre Waves, Int. Conf. Terahertz Electron," p. 398-399, (2007).

5. M. He, A. K. Azad, S. Ye, W. Zhang, "Far-infrared signature of animal tissues characterized by terahertz time-domain spectroscopy," Optics Commun. Vol. 259, p. 389-392 (2006).

6. J. Bauters, M. Heck, D. John, J. S. Barton, C. M. Bruinink, A. Leinse, R. Heideman, D. J. Blumenthal, and J. Bowers, "Planar waveguides with less than 0.1 dB/m propagation loss fabricated with wafer bonding," Optics Express, Vol. 19, p. 24090 - 24101 (2011).

7. Y. Chen, K. Wu, F. Zhao, G. Kim, R. T. Chen, "Reconfigurable True-Time Delay for Wideband Phased-Array Antennas," Proc. Of SPIE, Vol. 5363, p. 125-130 (2004).

8. J. Bauters, M. Heck, D. John, M.-C. Tien, A. Leinse, R. Heideman, D. J. Blumenthal, and J. Bowers, "Ultra-low Loss Silica-based Waveguides with Millimeter Bend Radius," Eur. Conf. Opt. Commun. ECOC, Vol. 1-2, (2010).

9. J. K. Doylend, M. J. R. Heck, J. T. Bovington, J. D. Peters, L. A. Coldren, and J. E. Bowers, "Two-dimensional free-space beam

steering with an optical phased array on silicon-on-insulator," Optics Express, Vol. 19, p. 21595 – 21604 (2011).